INAUGURAL - DISSERTATION

zur
Erlangung der Doktorwürde
der
Naturwissentschaftlich-Mathematischen
Gesamtfakultät
der

Ruprecht - Karls -Universität
Heidelberg

vorgelegt von
Dipl. - Ing. (Universität Bukarest) Oana Cristina Brinzanescu
aus Caransebes, Rumänien

Tag der mündlichen Prüfung: 14 Juli 2000

Röntgenstrahlung schwerer Projektile in Stößen mit Elektronen und Atomen

Gutachter: Prof.Dr.rer.nat. Heinz-Jürgen Kluge

Prof.Dr.rer.nat. Andreas Wolf

Dissertation
submitted to the
Combined Faculties for the Natural Sciences and for Mathematics
of the Rupertus Carola University of
Heidelberg, Germany
for the degree of
Doctor of Natural Sciences

X-Ray Emission of High-Z Projectiles in Collisions with Electrons and Atoms

presented by
Dipl. - Ing. Oana Cristina Brinzanescu
born in Caransebes, Romania

Heidelberg, July 2000

Referees: Prof.Dr.rer.nat. Heinz-Jürgen Kluge

Prof.Dr.rer.nat. Andreas Wolf

Röntgenstrahlung Schwerer Projektile in Stößen mit Elektronen und Atomen

Für meine Arbeit habe ich Berechnungen von totalen und zustandsselektiven Wirkungsquerschnitten im Rahmen einer nicht-relativistischen Theorie, ohne weitere Näherungen, für den atomaren Photoeffekt und seine zeitumgekehrte Reaktion, die Radiative Rekombination, durchgeführt. Die dabei gewonnenen Ergebnisse werden im Vergleich mit anderen nicht-relativistischen Theorien und einer vollständig relativistischen Rechnung dargestellt. Der radiative Elektroneneinfang wurde für hochenergetische Stöße von hochgeladenen, schweren Ionen mit leichten Targets untersucht. Hierbei wurden experimentell gemessene Winkelverteilungen und totale Wirkungsquerschnitte mit der exakten Theorie des REC verglichen. Eine genaue Messung der Spin-Flip Beiträge konnte im Rahmen der Experimente erstmals durchgeführt werden. Die atomare Struktur von helium- und lithiumähnlichem Uran in Stößen mit verschiedenen Targets wurde durch die theoretische Simulation der Röntgenspektren untersucht. Die Gültigkeit der von mir zur Beschreibung der beiden konkurrierenden Elektroneneinfangsprozesse, radiativer und nicht-strahlender Einfang, benutzten Theorien wird diskutiert, sowie ihre unterschiedlichen Beiträge zum totalen Elektroneneinfang dargestellt. Die Unterschalen sensitiven Ergebnisse (nlj), die zum ersten mal mit den experimentellen Daten verglichen werden, zeigen für die meisten Fälle eine gute Übereinstimmung mit diesen.

X-Ray Emission of High-Z Projectiles in Collisions with Electrons and Atoms

Calculations of total and state selective cross sections are done within the nonrelativistic dipole theory for the atomic photoelectric effect and its inverse reaction, radiative recombination without any further approximations. The results are contrasted with other nonrelativistic theories and the exact relativistic formulation. The radiative capture process is studied for high-energy collisions of heavy ions with light targets. Angular distributions and total cross sections experimental data are compared with exact theories for REC. A precise measurement of spin-flip contributions is accomplished for the first time. Atomic structure is investigated in the case of helium- and lithium-like uranium in collisions with different targets in the theoretical simulation of the x-ray spectra. The validity of the theories we used for the two competing capture processes - radiative and non-radiative - is discussed, as well as their different contributions to total electron capture. Subshell (*nlj*) sensitive results are compared for the first time with the experimental data, showing a reasonable agreement in most of the cases.

Contents

Introduction

In the evening of 8th November 1895, in the university of Würzburg Wilhelm Conrad Röntgen observed for the first time the x-ray emission and later named it like this due to its mysterious nature at that time. Now it is known since a long time as electromagnetic radiation of atomic origin, produced in collisions. The first studies date back to around 1930, with the calculations of Stobbe [1], Gordon [2], Sauter [3] and many others. Later on, the fast progress of nuclear physics shadowed the interest in atomic collision processes, subject that was classified as a basically well-known phenomena. A major reason for the present interest in x-rays from ion-atom collisions is the new insight introduced by the use of heavy ions as projectiles, which in the last decades gave rise to the discovery of several intriguing effects not predicted previously. The successful advent of high-energy accelerators, storage and cooler rings for brilliant beams of heavy ions, together with the application of well-accepted theories and new calculations have not only enabled such effects to be studied and understood, but also fundamental fields in heavy-ion physics have been opened widely for exciting explorations.

There are two general aspects to be considered in the field of atomic physics with highly charged ions: the collisional aspect and the atomic structure one. Both aspects have to be explored equally as they are strongly correlated. The interaction processes have to be investigated in order to know the population of excited states, that may clear up aspects of the atomic structure, and vice versa, one has to know the structure in order to understand the interaction.This is in particular true for the heavy-ion species with only a few - or even none - electrons left.

Recombination between electrons and ions plays an important role in different areas of modern physics and is subject to an increasing interest. The basic two- and three-body recombination processes are of very fundamental nature and relevant to accelerator-storage-ring based research, plasma and nuclear physics. The Radiative Electron Capture, one of the most important reaction channels in atomic collisions between highly charged heavy ions and low-Z target atoms can be viewed as Radiative Recombination, which is essentially the time reversed photoionization process. The capture cross sections are an important basis for estimates of beam losses, data which are urgently needed. In collisions, especially at high velocities, subtle effects of the relativity may be probed. Here, in particular also, magnetic and spin-flip effects may be studied; and the interaction processes at high central fields may deviate considerably from those involving low-Z ions (Stöhlker *et al.*, [4]). This is not only true for the typical excitation and ionization processes but as well for different capture and recombination processes. The capture of one electron by a heavy ion can be followed by cascade transition to the ground state; the analysis of the x-ray spectra can give precise information about details of the atomic structure.

All these interesting and fundamental aspects can be tested sensitively with the new tools, the heavy ion storage/cooler rings. Ions up to naked uranium can after acceleration and stripping be accumulated to high intensities in storage rings. By cooling - mainly by cold electrons - the phase space density can be increased, so that high luminosity beams of highly charged heavy ions can be provided for experiments. With these tools, the interaction of the heavy ions with photons, with electrons and with atoms can be studied selectively. Due to the long storage times for the heavy ions, also lifetime measurements for both, atomic as well as nuclear states get accessible (Kluge *et al.*, [5]; Andersen *et al.*, [6]; Irnich *et al.*, [7]). Last but not least, the storage rings can be tuned as high resolution mass spectrometers giving additional and important information on both atomic and nuclear structure of these heavy ions. The first steps had been tried on the long way towards extreme precision known from measurements in low-Z ion traps (Thompson, 1990, [8]).

This PhD work essentially reports about x-ray production processes: recombination processes between electrons and high-Z ions in slow and fast collisions, and investigation of x-ray spectra produced in collisions with light targets, as result of electron capture.

The **Chapter 1** of this thesis establishes in a brief way the theoretical frame of this work. Here, the main processes that lead to projectile x-ray production are discussed, as the free and bound electron capture processes in collisions of highly charged heavy ions with targets, the bremsstrahlung process and the decay dynamics within the excited shell of the atoms. The importance of understanding and using these theoretical tools is emphasized, in order to analyze and predict atomic physics related phenomena.

The experimental environment of GSI, in which the measurements have taken place is widely described in **Chapter 2**. The accelerator facilities, the storage ring and the technique of electron cooling are presented here. The current progress in the basic fields of atomic collisions and structure research involving high Z ions is closely related to the application of both advanced ion sources and advanced accelerator and storage techniques. The recent development of relativistic heavy-ion storage rings opened new challenging possibilities. The electron cooling guarantees ion beams of unprecedented quality, i.e. this technique provides cooled and intense beams with precisely known energies, charge state, momentum spread and beam diameters close to 1mm.

In **Chapter 3**, radiative recombination cross sections and rate coefficients calculations are presented. These calculations are performed numerically, for the first time without further approximations, for the nonrelativistic case. The comparison with experimental data, with other nonrelativistic theoretical results and with the complete relativistic calculations shows an overall good agreement. Since the latter approach involves significant contributions from higher multipoles and yields different angular distributions, the unexpected agreement with the nonrelativistic dipole approximation is very fortunate. Other test of validity of the dipole approximation has not been performed up to now.

Angle-differential cross section experiments and comparison with the nonrelativistic and the complete relativistic calculations are presented in **Chapter 4**, emphasizing the sensitivity of this kind of measurements to relativistic effects. The precision of this technique is illustrated by the experimental separation and identification of the spin-flip contributions.

Chapter 5 describes state selective investigation for electron capture in high energy collisions of H- and He-like uranium with target atoms. Up to now, rare final state selective information about electron capture in the domain of medium and high energy collisions was available. This study is concerned with population cross sections for (n,l,j) specific projectile states. In the case of helium-like uranium in collisions with several noble gas targets, it contains a full comparison between the experiment performed at ESR gas-jet target and computer simulations based on the existing theoretical predictions for the main capture processes involved. The domain of applicability of these theories is discussed as a function of the atomic number of the target and the energy of the collision, as it results from this study, and also in comparison with other theoretical approaches for REC and NRC.

For collisions of hydrogen-like uranium, a theoretical analysis of the x-ray production and the decay dynamics of the excited states in the helium-like uranium, after electron capture, is presented. Emphasize is being paid particularly to the formation of $^3P_0$ level and $^3P_2$ levels, states that are of interest for precise life-time measurements in future experiments, already foreseen at the ESR storage ring.

In summary, the present work relates about experimental and theoretical investigation of highly charged heavy projectile x-ray production in different types of collisions. Problems of capture and atomic structure calculations are addressed from the theoretical point of view and performed numerically. Issues connected to recent measurements and with other theories are widely discussed. Further investigations are required in the mentioned cases, where discrepancies from the actual experimental data are observed. The novelties brought by this PhD work with respect to all experiments and calculations done on the same subject, have been:

- The Radiative Recombination cross sections calculations based on the nonrelativistic theory of Stobbe, were performed without any further approximations;
- In the Radiative Electron Capture angular distribution study, the observation of photon emission close to 0° allowed a precise measurement of spin-flip contributions to the differential K-REC cross sections for the first time;
- The study of differential data for photoionization of a high-Z element in the low-energy regime, i.e. the separation of the radiative capture into the ground state from the capture into excited states and furthermore, the separation of the fine-structure components of the L shell;
- The subshell (nlj) selective information about population cross section for capture into hydrogen- and helium like uranium.

Chapter 1

X-Ray production processes in ion atom collisions

In this chapter the x-ray production processes involving highly charged ions will be discussed. The analysis of spectral information, obtained from different astrophysical objects, provides an unique possibility for the study of physical processes taking place in these objects. The most abundant emission in the UV and x-ray region comes from the stars, supernova remnants, so-called compact x-ray sources, galactic nuclei and quasi-stellar objects, signifying highly energetic phenomena in them. While galactic and extra-galactic x-ray astronomy is still in its beginning stage, solar UV and x-ray spectroscopy have already given invaluable contributions to the understanding of physical processes and conditions in the solar plasma. On the other hand, precise data about the cross sections of radiative and collision processes of multiply charged ions are a prerequisite both for the diagnostics and modeling of the solar plasma. In controlled thermonuclear fusion research, modern accelerator-based ion physics, in the creation of powerful laser light in xuv and x-ray wavelength region, there is a stringent demand of data in the atomic physics.

1.1 Recombination

The capture of free electrons in bound ion states is essentially described by three competing recombination mechanisms, i.e. radiative recombination (RR), dielectronic recombination (DR) and three body recombination (TR). Radiative recombination and dielectronic recombination represent the time-reversed photoionisation process and Auger effect, respectively. The triple collision recombination could be described as the time reversed ionisation by electron collision .

The main and the simplest recombination mechanism is the radiative recombination, in which the free electron is directly captured by an ion A^{Q+} and the excess energy and momentum are carried away by a photon (see Fig. 1.1):

$$A^{+Q} + e^{-} \rightarrow \begin{cases} \left[A^{+(Q-1)}\right] + \hbar\omega & \text{for capture in the ground state} \\ \left[A^{+(Q-1)}\right]^{*} + \hbar\omega & \text{for capture in excited states} \end{cases}$$

After the capture, the electron can be in an excited state and there will be further radiative transitions within the ion until the electron has reached the lowest accessible energy level. RR is a non-resonant process with a diverging cross section at zero center-of-mass energy which continuously decreases towards higher energy.

On the opposite to radiative recombination, is the dielectronic recombination, as a consequence of the electron-electron interaction between the continuum electron and the bound electron of the ion, therefore possible only in the case of ions which have at least one electron. The free electron is captured in an excited state j, the energy difference being nonradiatively transferred to an electron in a bound state i, which undergoes a transition to a higher excited state f:

$$A^{+Q} + e^{-} \rightarrow \left[A^{+(Q-1)}\right]^{**} \rightarrow \left[A^{+(Q-1)}\right]^{*} + \hbar\omega \tag{1.1}$$

Considering the energy conservation law, this process is only possible when the energy difference between the two levels i and f is equal to the sum between the kinetic energy of the electron in the initial free state and the binding energy of the excited level j, giving the resonance condition:

$$\Delta E = E_f - E_i = E_{kin} + E_j \tag{1.2}$$

DR is a resonant capture process, by simultaneous electron excitation, with the formation of an intermediate doubly excited state. In the doubly excited ion, the electrons will finally decay either individually to the ground state or by emission of an Auger electron describing a two-step process. In Fig. 1.1 the KLL-resonance (excitation from the K to the L shell with simultaneous capture in the L-shell of the projectile) in H-like ions is presented.

Another recombination mechanism possible for a bare ion is the three-body recombination (TBR)

$$A^{+Q} + e^{-} + e^{-} \rightarrow \left[A^{+(Q-1)}\right]^{*} + e^{-} \tag{1.3}$$

This process is important at high electron densities and very low center-of-mass energies between electrons and ions (see Fig. 1.1). The difference to DR is that the energy produced by the capture of the continuum electron is transferred to a second free electron as kinetic energy. The electron is captured in this case in a Rydberg state, for which the binding energy is comparable to the kinetic energy of free electrons.

In the next subsections, the recombination processes RR and DR will be discussed in more detail, as well as the scaling behaviour of the recombination cross section as a function of the projectile energy ($E_{kin} = (m_e/M)E_P$ the transformed kinetic energy of the projectile per atomic mass unit), the projectile nuclear charge and the adiabaticity parameter η, defined by:

$$\eta = \left(\frac{v_e}{v_0 Z_P}\right)^2 = \frac{E_{kin}}{E_K} \tag{1.4}$$

.

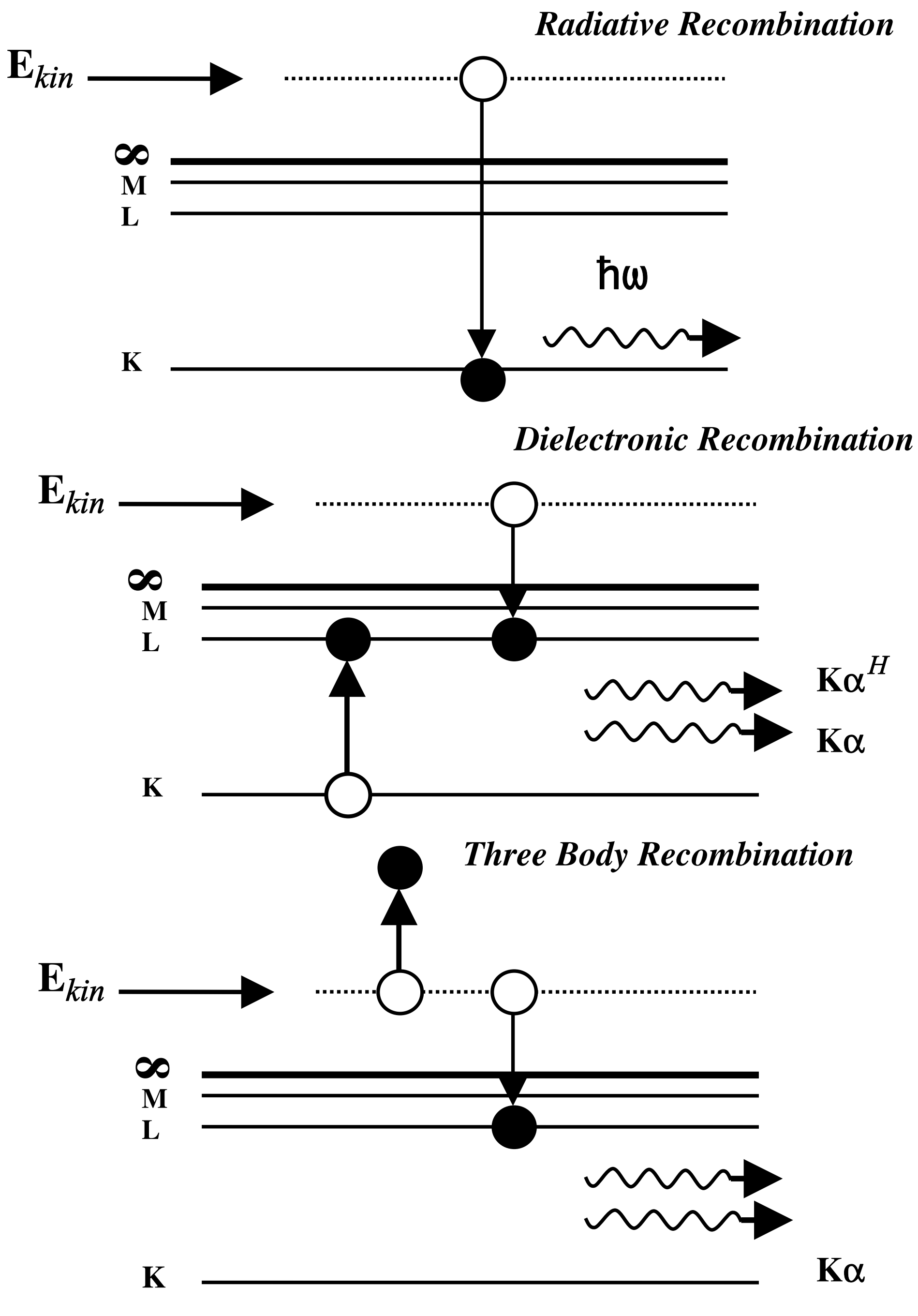

Figure 1.1: Schematic representation of recombination processes. radiative recombination; dielectronic recombination, in this example the KLL resonance in H-like ions; the three-body recombination in fully ionized atoms.

1.1.1 Radiative recombination

The transition amplitude for the radiative transition of an electron from the continuum state $|i>$ to the bound state $|f>$ is given by:

$$T_{if}^{RR} =< i|D|f > \tag{1.5}$$

where D is the photon operator (generally the dipole operator r_{12}). Considering the time reversal invariance, the transition rates as well as the interaction cross sections can be deduced according to the principle of detailed balance from the cross sections for the time reversed process, the photoionisation [9]. The general relation between time reversed processes is given by the rate equation:

$$\Gamma_{i\to f} g_i = g_f \Gamma_{f\to i} \tag{1.6}$$

where g_i and g_f are the respective degeneracies of the quantum states and $\Gamma_{i\to f}$ the rate of the transition from state i to state f. From (1.6) one can deduce directly the relation for the cross section:

$$\sigma_{i\to f} = \frac{p_f^2 g_f}{p_i^2 g_i} \sigma_{f\to i} \tag{1.7}$$

where p_i and p_f are the relative momenta of the particles in the initial and final state, respectively. Considering the photon impulse $p_f = (\gamma - 1)m_e c + E_K/c$ and the electron momentum $p_i = m_e \gamma \beta c$, the cross section for the radiative recombination in the K-shell of an atom will be:

$$\sigma_{RR} = \left[\frac{E_{RR}}{\gamma \beta m_e c^2}\right]^2 \sigma_{PE}(E_{RR}) \tag{1.8}$$

where σ_{PE} is the photoionization cross section. In this way the photoionization process can be directly and completely described by the radiative recombination. For a detailed discussion upon the different theoretical descriptions of the photoeffect and their domains of applicability we refer to Ref.[10].

In the following we will describe the nonrelativistic treatment of the radiative recombination for capture into fully stripped ions.

Bethe and Salpeter gave a formula for the radiative recombination cross section in the K-shell of a fully stripped ion in the nonrelativistic approach (nonrelativistic Coulomb wave functions for the continuum states, hydrogenic wave functions for the projectile bound state and no retardation ($\beta \ll 1$) ([1], [11]) :

$$\sigma_{RR} = 9.1 \times 10^{-21} \left(\frac{\kappa^3}{1+\kappa^2}\right)^2 \frac{\exp(-4\kappa \arctan \kappa^{-1})}{1 - \exp(-2\pi\kappa)} cm^2 \tag{1.9}$$

where the parameter $\kappa = \sqrt{\frac{E_K}{(E_{RR} - E_K)}}$ and E_K is the K-shell binding energy. In the high-energy domain, the cross section becomes:

$$\sigma_{RR} = 1.4 \times \kappa^5 10^{-21} cm^2 = 1.4 \left(\frac{Z_P}{v}\right)^5 10^{-21} cm^2 \tag{1.10}$$

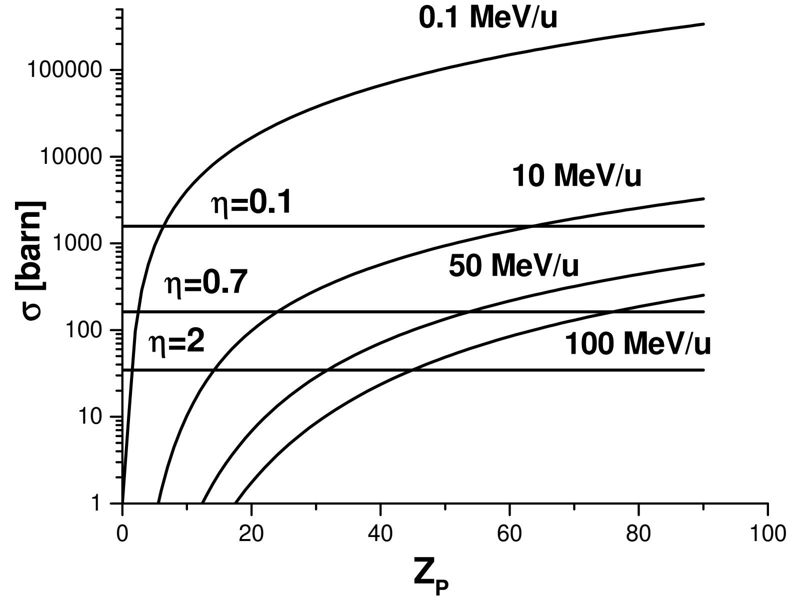

Figure 1.2: RR cross section (dipole approximation, see chapter 4) for capture in the empty K-shell of the projectile as function of Z_P for different collision energies and adiabaticity parameters η (nonrelativistic description).

and the parameter $\kappa = 1/\sqrt{\eta}$. From (1.10), the cross section is constant for all the systems with the same adiabaticity parameter η. The general cross section dependence of the projectile charge is given in Fig. 1.2. For kinetic energies $E_{kin} \gg E_K$ the capture in states with $l \neq 0$ is negligible, and the cross section decreases rapidly with the increase of the principal quantum number ($\sigma_{RR} \approx 1/n^3$). For small relative energies, ($E_{kin} < E_K$) the above dependence of n and l is not valid anymore. The capture in the K-shell remains the dominant recombination channel. Analytical formulas up to a principal quantum number $n = 3$ for the nl-sensitive radiative recombination cross section are calculated in Ref. [1]. A detailed description of these processes was done by Spindler [12]. A more detailed description, including recent results of relativistic theory for radiative recombination, will be made in the chapter 3 of this thesis.

1.1.2 Dielectronic recombination

The dielectronic recombination transition amplitude can be described taking into account the radiative stabilization of the intermediate state $|d>$:

$$T_{if}^{DR} =< i|V\, G^{\Gamma}\, D|f > \tag{1.11}$$

with

$$V = \frac{1}{|\vec{r_1} - \vec{r_2}|} \tag{1.12}$$

the operator for electron-electron interaction (here nonrelativistic),

$$D = r_{12}^{l} \tag{1.13}$$

the multipole operator for the electron-photon interaction, and G^{Γ} the Green function that describes the coupling of all the decay channels of the intermediate state. With the assumption that the single dielectronic resonances with the same total angular momenta do not overlap in the intermediate state, the transition amplitude of DR can be simplified to

$$T_{fi}^{DR} = \sum_{d} \left(\langle f|D|d \rangle \frac{1}{E_i - E_d + \frac{i\Gamma\hbar}{2}} \langle d|V|i \rangle \right) \tag{1.14}$$

The width of the resonance can be expressed as the total decay rate of the intermediate state

$$\Gamma_d = \Gamma_a + \sum_i \Gamma_{r_i} \tag{1.15}$$

where Γ's are the Auger (Γ_a) and the radiative rates (Γ_{r_i}), respectively, that can be derived from:

$$\Gamma_{i\to f} = \frac{2\pi}{\hbar} |T_{f\to i}|^2 \rho_{i\to f} \tag{1.16}$$

The dielectronic recombination rate can be now deduced from the transition amplitudes $T_{df}^{R} =< d|D|f >$, $T_{id}^{A} =< i|V|d >$ and applying the rule (1.16), analogous with (1.11)

$$\Gamma_{i\to d\to f}^{DR} = \pi\hbar \frac{\Gamma_r}{\Gamma_d} \Gamma_a(i \to d)\delta(E_{kin}) \tag{1.17}$$

where $\delta(E_{kin})$ is a Lorentz distribution function normalized to one, which reflects the resonant character of the process, and $\Gamma(i \to d)$ is the rate for nonradiative capture with simultaneous excitation. Considering the principle of detailed balance (1.7), the Auger rate is

$$\Gamma(i \to d) = \frac{g_d}{2g_i} \Gamma_a(d \to i) \tag{1.18}$$

where the factor 2 reflects the spin of the continuum electron.

From the normalization of the transition rate to the electron flux, the total interaction cross section is:

$$\sigma_{i\to f}^{DR} = 4\pi \times \frac{g_d}{2g_i} \Gamma_a \frac{E_0}{E_{kin}} \tau \omega_{d\to f} \delta(E_i) \pi a_0^2 \tag{1.19}$$

where τ and E_0 are the atomic time and energy units, respectively. The fluorescence yield defines the branching relation between the radiative and the Auger decay of the intermediate state and is defined by

$$\omega_{d\to f} = \frac{\sum \Gamma_r}{\sum \Gamma_r + \Gamma_a} \tag{1.20}$$

The nuclear charge dependence of the dielectronic recombination cross section can be directly derived from (1.19), taking into account the Z-dependence of the radiative and Auger rate, respectively. The transition amplitude for the Auger process, $< i|\frac{1}{r_{12}}|d >$ includes four electron orbitals: three bound wave functions : ψ_1^i, ψ_1^f, ψ_2^f, and a continuum wave function ψ_2^i, with $|i> = |\psi_1^i\,\psi_2^i>$ and $|f> = |\psi_1^f\,\psi_2^f>$. In the nonrelativistic case, the bound wave function scales with $Z^{3/2}$ and the continuum wave function with $Z^{1/2}$. The Z-dependence is then defined exclusively by the normalization factors of the wave functions. Furthermore, all states scale with Z^{-1} and consequently $1/r_{12} \approx Z$, respectively d^3r_1, $d^3r_2 \approx Z^{-3}$ [13]. Thus, the scaling law for the Auger rates results in

$$\Gamma_a \approx |< i|\frac{1}{r_{12}}|d>|^2 \approx |Z^{3/2}Z^{3/2}ZZ^{3/2}Z^{1/2}Z^{-3}Z^{-3}|^2 = Z^0 \tag{1.21}$$

From (1.16) and $\Delta E_{df}^3 \approx Z^2$ for the electric dipole transitions with $\Delta n = 0$, one can express the nuclear charge dependence of the radiative transition rate between two bound states characterized by ψ_d, ψ_f :

$$\Gamma_r \approx \Delta E_{df}^3|< d|r|f>|^2 \approx Z^6|Z^{3/2}Z^{-1}Z^{3/2}Z^{-3}|^2 = Z^4 \tag{1.22}$$

While for small Z the relation $\Gamma_r \ll \Gamma_a$ is satisfied, for heavy ion systems, considering the different scaling laws valid for Γ_a and Γ_r, the relation is inversed. This results in a decrease of the electron-electron interaction relevance, with increasing Z. For the DR cross section, only the following scaling law remains:

$$\sigma_{DR} \approx \frac{1}{E_{kin}}\frac{\Gamma_a\Gamma_r}{\Gamma_a+\Gamma_r} \approx \begin{cases} Z^{-2} & \text{for } \Gamma_a \ll \Gamma_r \quad (Z \gg 30) \\ Z^2 & \text{for } \Gamma_a \gg \Gamma_r \quad (Z \ll 30) \end{cases}$$

with $E_{kin} \approx Z^2$. It should be emphasized that this result is based on the scaling laws valid for nonrelativistic wavefunctions.

The relativistic calculations for two-electron systems show that in particular for high Z the use of relativistic wave functions and the consideration of the Breit interaction can lead to a bigger increase of the Auger rates in such a way that the relativistic corrections become comparable with the nonrelativistic rates [14]. In this reference, the Z-scaling laws for the relativistic corrections show a Z^2 dependence for $Z < 45$ and a Z^4 dependence for $Z > 45$.

In the case that the RR cross section and the DR cross section are approximately equal, interference processes may appear [15].

Meanwhile, precise experimental data are available for heavier elements [16]. Measurements of the cross section for dielectronic recombination between electrons and multiply charged ions have reached high accuracy suitable for a detailed comparison with theoretical predictions. Many experiments were done at several storage rings on a number of atomic systems [17, 18, 19].

The three body recombination process (TR) is typical for high electron densities and small relative velocities between the ion and the electron. Only in this case, this process can have a significant influence on the total electron recombination rate. Other recombination processes, but with much smaller probability are the multi-electron recombination processes, i.e. the resonant capture of two electrons with simultaneous excitation of the projectile (2eDR) and the simultaneous capture of two electrons with emission of one photon (2eRR) [20],[21].

1.2 Electron Capture in Ion-Atom Collisions

In this chapter the charge exchange processes will be discussed, which dominate the x-ray production and charge exchange rates in collisions between highly charged ions and atoms. They can be divided in two main groups of mechanisms: capture of quasi-free electrons i.e. the radiative electron capture (REC) and the radiative transfer excitation (RTE), and the Coulomb capture processes, the non-radiative electron capture and the non-radiative transfer excitation.

1.2.1 Quasi-free electron capture

The radiative electron capture (REC) and the resonant transfer excitation (RTE) are the analogue charge exchange processes of RR and DR in ion-atom collisions. For the three body recombination, the collision of two quasi-free electrons in the projectile Coulomb field can lead to the capture of one electron. In contrast to recombination, here the electrons are captured from the bound states of the target into the bound state of the projectile. As long as the binding energy of the target electron is negligible compared with the relative kinetic energy, these electrons are regarded as "quasi-free". Consequently, REC and RTE can be described as recombination processes within the impulse approximation, taking into account the momentum distribution of the electrons in the target atom. The impulse approximation can be applied as long as:

$$\frac{v_i}{v} = \left[\frac{E_B^T}{E_{kin}}\right]^{1/2} \ll 1 \tag{1.23}$$

where v_i is the orbital velocity of the target electron i, E_B^T the binding energy in the target and v the projectile velocity.

Radiative Electron Capture (REC)

Due to the binding of the electrons in the target potential V_T, the target electrons are not at rest, but their motion is described by a symmetric momentum distribution $f(\vec{v_i})$. One can write the total electron energy E in the projectile system

$$E = \frac{m_e(\vec{v} + \vec{v_i})^2}{2} + V_T = E_{kin} - E_T^B + m_e\vec{v}\vec{v_i}\,. \tag{1.24}$$

If E_f is the electron binding energy in the projectile, one has for the REC photon energy in the projectile system:

$$E_{REC} = \hbar\omega_{REC} = E_{kin} + E_f - E_i + \vec{v}\vec{p_i} \tag{1.25}$$

and in the relativistic form, respectively

$$E_{REC} = \hbar\omega_{REC} = (\gamma - 1)mc^2 + E_f - \gamma E_i + \vec{\beta}\gamma c\vec{p_i} \tag{1.26}$$

The last term in (1.26), the momentum distribution of the target electrons (Compton profile) defines in addition a characteristic width of the energy distribution of the REC photons centered at

$$E_{REC} = \hbar\omega_{REC} = (\gamma - 1)mc^2 + E_f - \gamma E_i \tag{1.27}$$

In the laboratory system, in (1.27) the Doppler shift and the Doppler broadening have to be considered in addition . For small angles and energies the width of the REC energy distribution (FWHM) is mainly determined by the Compton profile of the target electrons given by [22], [23] :

$$\Delta E_{FWHM} = 2.04[E_{kin}E_i]^{1/2} \tag{1.28}$$

The width of the Compton profile is proportional to the projectile velocity. The energy dependence of the cross section will be reflected in a slight asymmetry of the distribution, i.e. the small energy part will rise while the high energy part will steepen. Both the total and the angle-differential REC cross sections can be deduced from the respective equations for the radiative recombination (e.g. (1.9)). This cross section has to be multiplied by the number of quasi-free target electrons with the help of (1.23). However, it should be stressed that the RR angular distribution of the photons in the laboratory system can be considered valid only partially for the REC process. The binding of the electrons in the target will introduce a deviation from the sin^2- distribution at small forward and backward angles. In case the electron momentum distribution in the target can be neglected, REC can be viewed as the time-reversed photoionization process. In this case, the deviations from the symmetric $\sin^2\theta$ distribution provide a direct measure of relativistic corrections becoming significant for ions with nuclear charge higher than Z=70 even for energies lower than 300 MeV/u. In these cases, a non-zero cross section at forward and backward angles has shown to be the unique signature of spin-flip transitions (see chapter 5, [4]).

1.2.2 Coulomb Capture

The interaction between the Coulomb potential of the projectile and the target electrons can lead to another group of capture processes, i.e. the Coulomb capture. Several mechanisms can be described here, like nonradiative electron capture (NRC), nonradiative transfer excitation (NTE), multi-electron nonradiative capture. As a consequence of the capture in excited states of the projectile, a cascade decay from the upper levels gives the specific x-ray spectra of the projectile.

Nonradiative electron capture (NRC)

In Coulomb capture, the energy difference between the initial bound state of the electron in the target and the final bound state in the projectile is converted in kinetic energy of the collision partner, for which:

$$E_f \approx E_{kin} + E_i \tag{1.29}$$

For medium collision energies, i.e. $\eta < 1$ and asymmetric collision systems ($Z_T < Z_P$) the capture of the most tightly bound electrons in the target in an excited state of the projectile is followed by a radiative decay to the ground state. The width

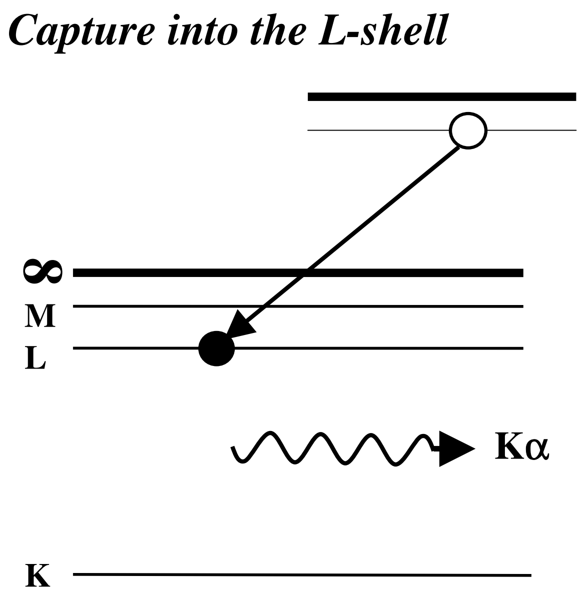

Figure 1.3: Schematic representation of Coulomb capture.

of the momentum distribution of the target K-shell electrons determines a broad maximum of the final state distribution $f(n_f)$. The capture in the K-shell, on the contrary, is in this energy domain negligible.

The cross section for NRC from inner target orbitals in fully ionized projectiles is described by the first-order Born approximation (OBK - approximation). Here it is considered that projectile moves on a straight trajectory and the target and projectile states can be described by hydrogenic wave functions. The influence of the electrons on the binding energies will be introduced by considering the Slater screening constants. The relativistic Oppenheimer Brinkmann Kramers (OBK) theory of Shakeshaft and Moiseiwitsch and Stockman predicts cross sections for low-Z projectiles that are more than a factor of 3 too high compared with experiment. This is typical for results seen also at nonrelativistic velocities where the application of second-order Born approximation theories improve the agreement between theory and experiment. For low-Z relativistic heavy ions, even second-order Born approximation calculations are generally higher than experiment. However, the typical energy dependence for the Coulomb capture is maintained. The OBK cross section for the nonradiative capture of an electron from an initial state n_i in the target to a final state n_f of the fully ionized projectile is given by:

$$\sigma^{NRC} = 12.54 \frac{Z_P^5 Z_T^5}{n_f^3 n_i^3} \frac{1}{E_{kin}} \left[\frac{1}{4E_f + (E_{kin} + E_i - E_f)^2 / E_{kin}} \right]^5 \times 10^{-14} cm^2 \qquad (1.30)$$

where E_f, E_i and E_P are expressed in keV and E_{kin} is the transformed projectile energy per atomic unit ($E_{kin} = m_e/M\, E_P$). For the high-energy domain ($E_{kin} \gg$

E_f, E_i), (1.30) gives the energy dependence $\sigma^{NRC} \sim 1/E_P^6$ (relativistic calculations give for high relativistic collision energies a $1/E_P$-dependence [24]).
A comparison with the scaling law for the REC cross section (1.31), where the number of quasifree electrons in the target has to be considered)

$$\sigma^{REC} \sim Z_T Z_P^5/(n_f^3 v^5) \tag{1.31}$$

shows that in the case of heavy targets and small collision energies the NRC capture is the dominant capture process.

Another theory proposed for NRC is the eikonal-approximation [25] which gives a better agreement with the experimental data for medium as well as for relativistic collision velocities. One of the formal difficulties with the eikonal approximation is that it is an asymmetric theory. One active electron-nucleus interaction is treated in higher order while the other interaction is treated in the first order perturbation theory. Within this approach, in its prior (post) version, treats the electron-projectile (electron-target) in first order while the electron-target (electron-projectile) interaction is treated in all orders of perturbation theory, albeit in an approximate way. The conceptual basis of the eikonal approximation has been discussed in detail, [25],[26], and it has been shown that, physically, the prior version of the theory describes a hard collision of the electron with the projectile nucleus followed by multiple soft collisions with the target nucleus. Similarly, the post version of the theory describes a hard collision of the electron with the target nucleus preceded by multiple soft collisions with the projectile nucleus. The approximate summation of multiple scattering terms, characteristic of the eikonal approximation, avoids divergent terms that can arise [27] in exact perturbation summations, e.g., in the strong potential Born approximation [28]. With the existence of two versions of the theory, the problem arises as to which one is appropriate for a given case. In principle, the answer is unique: The stronger of the two potentials Z_p/r_p or Z_t/r_t should be treated nonperturbatively and the other one in first order. Identifying the charge number Z_p or Z_t with the parameter that measures the strength of the potential customarily leads to the "higher charge" prescription.

Another theory which proves to be applicable for the treatment of NRC is the Continuum Distorted Wave approximation (CDW) which will be treated in more detail in the chapter 4 of this work.

Other nonradiative capture processes:

- Multielectron capture is treated within the Independent Particle Model, i.e. the electrons are captured independently as a consequence of the electron-projectile interaction. Here the electron-electron interactions are included, the theory being applicable especially for medium to high-energy collisions. However, considering the total cross section over all values of the impact parameter, generally the two-electrons capture cross sections are with at least one order of magnitude smaller than the nonradiative one-electron capture cross sections.

- Nonresonant transfer and excitation (NTE), i.e. the non-resonant electron capture by simultaneous projectile excitation is, besides REC, a concurrent charge exchange process for RTE. Within NTE, two uncorelated precesses occur: projectile excitation simultaneous with a kinematic electron capture during the collision, leading to a doubly excited state of the projectile by simultaneous charge exchange.

1.3 Bremsstrahlung

The electron bremsstrahlung arises when electrons undergo strong acceleration in the nuclear magnetic field of an atom and are radiating part of their kinetic energy. The energy spectrum of the bremsstrahlung ranges from 0 to the full kinetic energy of the electron E_{kin}. The total cross section has only a weak dependence on the energy of the radiation E_r and on E_{kin}, given in the classical limit by the simple Sommerfeld-Kramers result

$$\frac{\mathrm{d}\sigma}{\mathrm{d}E_r} = C_B \cdot Z^2/(E_r \cdot E_{kin}) \tag{1.32}$$

with $C_B = 1.43 \cdot 10^{-24}\, cm^2$ keV, [29]. (1.32) gives reliable results for the kinetic electron energy in the range of 1 keV $\leq E_{kin} <$ 500 keV. The bremsstrahlung spectrum is peaked perpendicular to the incident electron direction, and due to the retardation for electron energies higher than 10 keV, the maximum will be at forward angles in the laboratory system.

In ion-atom collisions, electrons are ejected from the collision system due to the ionization process, becoming a source of bremsstrahlung with a fairly high probability, i.e. producing a continuous radiation spectrum (secondary electrons). This process is more pronounced for solid targets, where the secondary electrons are stopped, but it can also be seen in many gas targets and thin solid targets, where the electrons are only slowed down. For the direct ionization by a light ion incident on a heavy target, [30], the energy distribution of secondary electrons in a single collision is well known. The intensity of ejected electrons is generally decreasing with increasing electron energy E_{kin}, roughly as E_{kin}^{-2}, from the lowest kinetic energies to the maximum energy T_m transferred to a free electron in a "head on" collision with an ion:

$$T_m = \frac{4mA_1M}{(A_1M + m)^2} \cdot E_1 \simeq 0.00218 \cdot E_1/A_1 \tag{1.33}$$

For energies higher than this value the intensity decreases rapidly, e.g. like E_{kin}^{-10}. In this classical forbidden region, only the high-momentum tail of the bound electron wave function can contribute to ejection of high-energy electrons. The secondary electrons will be slowed down by subsequent collisions and can also emit bremsstrahlung according to (1.32). The bremsstrahlung spectrum is simply a folding of the electron distribution with the factor of (1.32) to the electronic stopping power which essentially preserves the shape of the spectral distribution. The secondary electron bremsstrahlung is the dominant source of continuum x-ray emission for $0 < E_r < T_m$. The angular distribution of the radiation is peaked perpendicular to the beam or at small forward angles, because the electrons are mainly ejected in the forward direction (for high E_{kin}). The intensity may change as much as a factor 2 with the angle, but the theoretical calculation is difficult as the electrons may be severely deflected from their direction of ejection before they radiate, due to the slow-down process.

For heavy ions, the secondary electron bremsstrahlung is more complex, as the electrons are ejected both from target and projectile and from transient formed collision molecule. The target will be excited following a Z^2-scaling. The projectile will also emit electrons as a result of the collision with the target atom which moves with relative velocity -$\vec{v}$ with respect to the ion. Thus the projectile electrons are mainly ejected in the backward direction in the projectile frame.

The interest in secondary electron bremsstrahlung is partly motivated by the desire to know how much it contributes, when other processes such as quasi-molecular radiation are studied or when the emission of characteristic x-rays from the target is used for trace element analysis of small samples. The study of bremsstrahlung may contain information on the electron distribution in the target and the projectile.

Inner bremsstrahlung is the first step in secondary electron bremsstrahlung, namely the radiation from an electron in the field of the colliding nuclei from which it has been ejected. Generally its contribution is much less than that from many subsequent collisions, however this one-collision process survives for low-pressure gas targets and is important for heavy projectiles.

Inverse bremsstrahlung occurs for heavy-ion beams as the usual bremsstrahlung of target electrons in the field of the projectile and has a flat spectrum from 0 up to $\sim T_m/4$; the quasi-free electron of the target moves with $-\vec{v}$ relative to the projectile, corresponding to a kinetic energy $E_{kin} = mv^2/2 = T_m/4$.

For not too heavy targets, the cross section for this process is given by the bremsstrahlung cross sections for electrons moving with projectile speed multiplied by the number of available target electrons. The underlying assumption is that this process can be treated within the framework of the impulse approximation, i.e. the loosely bound electrons can be treated as quasi-free particles.

The major advantage of ion-atom collisions for the study of bremsstrahlung is that the charge state of the projectile can be easily and selectively varied. The case of bare ions attracts the greatest interest since here the interaction of the electrons with the pure Coulomb potential of the projectile can be studied in the absence of many-body effects. Hence, the reliability of theoretical models can be most rigorously examined in such experiments. In particular, high-Z projectiles are of interest, as they exclusively probe the coupling between the continuum states and the radiation field in the presence of strong external potentials. The study of Anholt [31] established that solid targets pose problems which arise from secondary electron bremsstrahlung, in particular when dealing with forward observation angles. Precise knowledge of bremsstrahlung cross sections is also important from a practical point of view since bremsstrahlung constitutes a serious source of background radiation in all ion-atom collision experiments ([32],[22]).

In the last two decades electron bremsstrahlung accompanying ion-atom collisions has been thoroughly investigated for intermediate projectile energies ([33], [34], [35]). In this energy domain the adaptation of the relativistic Born approximation together with the impulse approximation generally gives reasonable agreement with the experimental data. These studies have established that the relativistic Born approximation ([36]), modified by screening and Coulomb corrections is capable of describing fairly well the experimental data for moderate values of the characteristic parameter $Z\alpha/\beta$, where Z is the target nuclear charge, α is the fine structure constant, and β is the electron velocity in units of the speed of light. For the case of high-Z targets computationally much more sophisticated approximations ([37]) and exact all-order calculation schemes ([38], [39]) have been developed.

In recent years, a particular attention has been paid to the tip region (hard photon emission) of the spectrum since this energy domain is, in particular, sensitive to Coulomb distortions caused by the large nuclear charge of the projectile. Moreover, it is well established ([40], [41]) that hard-photon bremsstrahlung is closely related to the radiative recombination, i.e. the time-reversed photo-electric effect. The bremsstrahlung process may be interpreted as radiative recombination (RR), or radiative electron capture (REC) to positive energy states of the projectile, and indeed the matrix elements for the tip-region can be obtained by analytic continuation of those for REC. The latter process has been intensively studied theoretically as well as experimentally even for the highest nuclear charges ([42], [43], [44], [45]).

1.4 Radiative Transitions

The line spectra of highly charged ions are mostly studied in high-temperature laboratory sources (tokamak discharges, low-inductance sparks, exploding wires, laser produced plasmas) and astrophysical plasmas (solar flares and active regions). Such spectra are widely used for plasma diagnostics, providing important information on plasma densities and temperatures, chemical impurities and other parameters. An increase in plasma temperature leads to an increase of the ionization stages of heavy elements, which radiate spectral lines mostly in the vacuum ultra-violet (vuv) and x-ray regions.

The general structure of a multiply charged ion resembles the spectrum of a neutral atom in the same isoelectronic sequence. However, an important difference is the fact that the ion spectrum is shifted to the shorter-wavelength region. Another difference between the atomic and ionic spectra is connected with the clear spectral resolution of ionic lines which are not resolved in the corresponding atomic case. First of all, this concerns the fine structure components. In case of multiply charged ions, the relativistic corrections to the characteristics of orbital electrons increase strongly when the ionic charge increases. This leads to a significant increase in those transition probabilities which are usually small in the neutral atom in the same isoelectronic sequence.

The classification and calculation of the energy levels of multiply charged ions require a choice of the correct coupling scheme of the angular and spin momenta of the electrons. In the following we will shortly discuss the atomic structure, i.e. the coupling schemes, the electron binding energies and the transition probabilities between the bound states.

1.4.1 Coupling Schemes

The *coupling scheme* (or *vector coupling*) is the term describing the interaction of electrons in atoms, ions or molecules, showing the scheme of the vector addition of the orbital (l_i) and spin (s_i) momenta of the atomic electrons into the total momentum J.

In the zero-order approximation, the energy of the atomic system is defined by the electrostatic interaction V_{es} of the electrons with the nucleus and electrons themselves. In this approximation, the energy level is described by the configuration n_1l_1, n_2l_2, ..., n_N, which is g-times degenerate over all possible projections m_{li} and m_{si}:

$$g = 2(2l_1 + 1)(2l_2 + 1)...(2l_N + 1) \tag{1.34}$$

The non-central part of the electrostatic interaction V_{nc} and magnetic spin-orbit interaction V_{so} cause the splitting of the atomic level into sublevels; their relative positions can be described by the scheme of vector coupling of momenta l_i and s_i.

The types of coupling schemes can be easily illustrated considering two non-equivalent electrons with momenta l_1, s_1 and l_2, s_2:

$$\begin{array}{llll}
LS - coupling & \mathbf{l}_1 + \mathbf{l}_2 = \mathbf{L}, & \mathbf{s}_1 + \mathbf{s}_2 = \mathbf{S}, & \mathbf{L}_1 + \mathbf{S}_2 = \mathbf{J}; \\
LK - coupling & \mathbf{l}_1 + \mathbf{l}_2 = \mathbf{L}, & \mathbf{L} + \mathbf{s}_1 = \mathbf{K}, & \mathbf{K} + \mathbf{s}_2 = \mathbf{J}; \\
jK - coupling & \mathbf{l}_1 + \mathbf{s}_1 = \mathbf{j}_1, & \mathbf{j}_1 + \mathbf{l}_2 = \mathbf{K}, & \mathbf{K} + \mathbf{s}_2 = \mathbf{J}; \\
jj - coupling & \mathbf{l}_1 + \mathbf{s}_1 = \mathbf{j}_1, & \mathbf{l}_2 + \mathbf{s}_2 = \mathbf{j}_2, & \mathbf{j}_1 + \mathbf{j}_2 = \mathbf{J}.
\end{array}$$

In the case of equivalent electrons nl, due to the Pauli principle, the LS- and jj-couplings are the only possible couplings because all electrons participate symmetrically.

Each type of coupling scheme characterizes values of different types of interactions. The LS-coupling (also called Russel-Saunders coupling) is used when the electrostatic interaction V_{es} is much larger than the spin-orbit one $V_{es} \gg V_{so}$.

With increasing nuclear charge Z ($Z \to \infty$), the opposite situation occurs ($V_{es} \ll V_{so}$) and the jj-coupling scheme is used, which is of particular interest for highly-charged ions.

In the case $V_{es} \approx V_{so}$, the states are described by the so-called *intermediate coupling scheme*. With increasing nuclear charge, the coupling suffers a smooth transformation from the LS - to the jj-coupling.

The jK- coupling is usually called jl-coupling; jl-coupling is used when the spin-orbit interaction of the electrons with the nucleus is larger than the interaction of the latter with the excited electron. The jl-coupling appears in the spectra of excited states of noble-gas atoms (Ne, Ar, KR, Xe and Rn, e.g. configuration $np^5n's$) and of some other atoms when one of the electrons is in average at a large distance from the atomic core.

The LS-coupling scheme is the most commonly used. The designation for terms in LS-coupling is $^{2S+1}L_J$, where S, L and J are the spin, orbital and total momenta, respectively. For example, for the two-electron configuration $npn'p$, one has the singlet (S=0) and the triplet (S=1) states:

$$^1S_0, \quad ^1P_1, \quad ^1D_2, \quad ^3S_1, \quad ^3P_{1,2,3}, \quad ^3D_{1,2,3}.$$

The designation of terms in other coupling schemes is more complicated [46]. The number of sublevels is the same for a given total momentum J for all types of coupling schemes.

In many cases, the use of a "pure" scheme is not possible and it is necessary to use the intermediate coupling scheme [47].

The two-electron atom is a celebrated problem in quantum mechanics. The He-like atoms have two s electrons outside filled shells. The ground state of He is the state $1s^2\ ^1S_0$. Two systems of terms are possible on the excitation of one of the s electrons - the singlet system, $S = 0$, $2S + 1 = 1$, and the triplet $S = 1$, $2S + 1 = 3$. There are four possible combinations associated with the two electrons: the singlet when both orbital functions can be associated with spin $1/2$, or the first can have $1/2$, the second $-1/2$, or the first can have $-1/2$, the second $1/2$, or both can have $-1/2$. The closed shell $1s^2$ is extremely stable, and thus the He ground term lies very deep, considerably deeper than in the case of hydrogen. The ionization potential of helium is greater than that of any other element. The binding energy of the electron in an excited state is considerably less than in the ground state because the second electron, remaining in the state $1s$, screens the nuclear charge in this case. Transitions between triplet and singlet terms are forbidden in the LS-coupling approximation.

1.4.2 Binding Energies

The ground-state atomic levels are occupied according to the Pauli principle. If the electron configuration is known, the term of the ground state can be determined by *Hund's rule* [47]. According to this rule, the level with the greatest possible value of S for the given electron configuration and the greatest (possible for this S) value of L has the lowest energy.

The relativistic analogue to the Schrödinger equation is the four-dimensional Dirac equation:

$$\mathrm{i}\hbar = \frac{\partial}{\partial t}\psi(\mathbf{r}, t) = H\psi(\mathbf{r}, t) \tag{1.35}$$

considered for a central field, where the Hamiltonian is:

$$H = \mathrm{c}\alpha \cdot \mathbf{p} + \beta mc^2 + V \tag{1.36}$$

with $V = e\phi$. The energy eigenvalues, in the case of a hydrogenic atom, where $V(r) = -Ze^2/r$, give the energy levels:

$$E = mc^2 \left[1 + \frac{\gamma^2}{(s + n')^2}\right] \tag{1.37}$$

where n' is the *radial quantum number*, $n' = n - |k|$, $\gamma = Ze^2/\hbar c$ and $s = \pm(k^2 - \gamma^2)^{1/2}$.

According to Dirac theory, levels with different $l = j \pm 1/2$, same j, have exactly the same energy. This degeneracy, however is removed by including radiative corrections, as the Lamb-shift, vacuum polarization, etc. The radiation corrections to the energy are of the order of $\alpha(\ln\alpha)E_1 \ll E_1$.

The interaction of nuclei having a non-zero magnetic moment or a non-zero quadrupole moment with atomic electrons leads to a splitting of a level with the angular momentum J into components. This splitting is called the *hyperfine splitting*.

The energy levels of two isotopes of an atom are shifted relative to each other. The isotope shift is related with the finite mass and finite size of the atomic nucleus, and the mass effect is opposite in sign to the volume effect. For light elements, the volume effect is quite small, while for heavy atoms with nuclear charge $Z \gg 50$ it becomes dominant.

The main contribution to the total Lamb shift is given by a sum of the so-called *self-energy, vacuum polarization* and nuclear finite-size corrections.

For non-hydrogenic ions, the difficulties involved in the problem increase significantly due to additional interactions between the electrons. The relativistic corrections for many electron systems are accounted for usually in the framework of the Breit relativistic equation. The Breit-Pauli equation [11] can be solved on the basis of perturbation theory, with the eigenfunctions of the non-relativistic Hamiltonian and using the Hartree-Fock or Coulomb wave functions as zero*th* approximation.

1.4.3 Transition energies and probabilities

The fundamental formula of radiation theory for the probability of a spontaneous transition of an atom from a state n to a state n' (energies E_n and $E_{n'}$) with emission of one photon per unit of time is [11]:

$$W_{n'n}(\mathbf{k}, x)\mathrm{d}\Omega = \frac{e^2\hbar\omega_{nn'}}{2\pi m^2 \mathrm{c}^3}|D^{\mathbf{k}x}_{nn'}|^2\mathrm{d}\Omega \tag{1.38}$$

where $\mathbf{k}$ is the propagation vector in the solid angle $d\Omega$, x the polarization direction, $k = |\mathbf{k}|$ the wave number,$\nu_{nn'}$ and $\omega_{nn'}$ the "ordinary" and "angular" frequency of the photon, which satisfy the Bohr energy relation:

$$\omega_{nn'} \equiv 2\pi\nu_{nn'} \equiv ck = \frac{1}{\hbar}(E_n - E_{n'}) \tag{1.39}$$

In (1.38) D is the following matrix element

$$D^{\mathbf{k}x}_{n'n} = \int u^*_{n'} \sum_i e^{i\mathbf{k}\cdot\mathbf{r_i}} \frac{\partial u_n}{\partial x_i} \mathrm{d}\tau \tag{1.40}$$

where r_i is the position of the i-th atomic electron and the integral extends over the configuration space of all the electrons. The approximations made for deriving (1.39), (1.40) are the following : (1) the electrons have been treated nonrelativistically and the Schrödinger equation has been used instead of the Dirac and Pauli equations (neglect of magnetic moment and of specific relativistic effects); (2) the interaction of the electron with the radiation field has been treated as a small perturbation (with the fine structure constant α as the perturbation parameter) and only the lowest order term kept in the expansion in powers of α.

In most cases one can simplify (1.40) considerably by making further approximations. Considering that the distances r_i of the electrons from the nucleus are of the order of Bohr radius, i.e. 10^{-8} cm for low nuclear charges, and the wave number of the emitted light in the discrete spectrum is much smaller than 10^8 cm^{-1}, one can replace the exponent $\mathbf{k}\cdot\mathbf{r_i}$ by unity, i.e. the "retardation" is neglected. In this approximation, $D^{\mathbf{k}x}_{nn'}$ is the x component of the vector $D_{nn'}$ which does not depend on $\mathbf{k}$. Writing $D_{nn'}$ in a different form : $D_{nn'} = \frac{m}{\hbar}\omega_{nn'}\mathbf{r}_{n'n}$, where $\mathbf{r}_{n'n}$ is the dipole matrix element, one can obtain

$$W(\Omega, j)d\Omega = \frac{e^2}{2\pi\hbar c^3}\omega^3_{nn'}(\mathbf{e}_j\cdot\mathbf{r}_{n'n})^2\mathrm{d}\Omega \tag{1.41}$$

the probability that an atom will undergo a transition from the state n to n' and emit light of polarization direction $\mathbf{e}_j$ into the solid angle $d\Omega$. The intensity of light J_j, obtained by multiplying the probability by the energy of the light quantum $\hbar\omega$ is precisely the classical formula for the intensity of light emitted by an oscillating dipole having dipole moment $e\mathbf{r}_{n'n}e^{i\nu_{n'n}t}$ and frequency $\nu_{nn'}$. Multiplying J_j by the number of atoms in the state n and integrating over all directions of propagation of the emitted light, one can obtain the total transition probability for going from n to n':

$$A_{n'n} = \frac{4}{3}\frac{e^2\omega^4}{c^3}|\mathbf{r}_{n'n}|^2 \tag{1.42}$$

The total probability per unit of time that the level n decays through light emission is then the sum of $A_{n'n}$ over all inferior states n' :

$$\beta_n = \sum_{E_{n'}<E_n} A_{n'n} \tag{1.43}$$

and thus, the reciprocal of the mean life time of the state n is given by:

$$T_n = \frac{1}{\beta_n} = \frac{1}{\sum_{E_{n'}<E_n} A_{n'n}}. \tag{1.44}$$

Another useful quantity is the oscillator strength :

$$f_{n'n} = \frac{2m}{\hbar}\omega_{n'n}|x_{n'n}|^2 \tag{1.45}$$

A further expansion of $exp(i\mathbf{k}\cdot\mathbf{r_i})$ in powers of $\mathbf{k}\cdot\mathbf{r_i}$ gives the radiation of the higher electric and magnetic multipole moments. Considering an atom having a single electron, one can express the eigenfunctions in polar coordinates. Expressing the matrix elements of each coordinate, x, y and z, one can obtain several conditions for which these elements do not vanish:

$$\begin{aligned} z^{n'l'm'}_{nlm} &= \int u^*_{n'l'm'} z u_{nlm}\mathrm{d}\tau = \int_0^\infty r^2 dr R_{n'l'}(r)R_{nl}(r)\times \\ &\times \int_0^\pi \mathcal{P}_{l'm'}(\theta)\mathcal{P}_{lm}(\theta)\cdot cos\theta\cdot sin\theta\mathrm{d}\theta\cdot\int_0^\pi \frac{1}{2\pi}e^{i(m-m')\psi}\mathrm{d}\psi. \end{aligned} \tag{1.46}$$

If $m'\neq m$, the integral over ψ vanishes, i.e. one obtains the following selection rule for the magnetic quantum number for radiation emitted with polarization parallel to z : $\Delta m \equiv m' - m = 0$. From the othogonality relations obeyed by the associated Legendre functions: $\int_0^\pi \mathcal{P}_{l'm}\mathcal{P}_{lm} sin\theta d\theta = \delta_{ll'}$ and (1.46) we obtain the selection rule : $\Delta l \equiv l' - l = \pm 1$.

Evaluating the matrix elements of the coordinates x and y, the selection rule for the magnetic quantum number is obtained for radiation polarized parallel to the x and y axes : $\Delta m \equiv m' - m = \pm 1$. If one adds the intensities of the transitions from a certain state nlm to all the substates m' of the level $n'l'$ without regard to the direction of polarization of the emitted radiation, one finds that the sum is independent of m. A corollary of this is that the life time of a state is independent of its magnetic number and depends only on n and l. In the case of multipole radiation of order κ, q, the selection rules are the following:

$$|\Delta J| = |J' - J| = \kappa, \kappa - 1, ..., 0; J + J' \geq \kappa \tag{1.47}$$

$$\delta M = M' - M = q = -\kappa, -\kappa + 1, ..., \kappa \tag{1.48}$$

These selection rules have a simple physical meaning. Since the energy of multipole field, $\mathcal{E}$, the square of angular momentum, K, and the z component of the angular momentum, K_z satisfy:

$$K_z = \frac{m}{\omega}\mathcal{E};\ K^2 = \frac{l(l+1)}{\omega^2}\mathcal{E}^2 \tag{1.49}$$

then, to each quantum $\hbar\omega$ of the multipole radiation field there corresponds an angular momentum κ, q (square of the angular momentum $\hbar\kappa(\kappa+1)$ and z component $\hbar q$). The selection rules (1.47, 1.48) express the conservation of angular momentum $\mathbf{J} = \mathbf{J}' + \kappa$.

Chapter 2

The experimental environment

The GSI operates a quite complex accelerator structure for heavy ions, which consists of the linear accelerator UNILAC (UNIversal Linear ACcelerator), the synchrotron for heavy ions SIS, and the experimental storage ring ESR. As the knowledge of the experimental environment is indispensable for the understanding of atomic physics experiments, in this section we will essentially describe the accelerator facility and the storage ring. The measurements presented in this work have been carried out mainly at the ESR. Hence, a more detailed description of the ESR will be given in the following, with its most important properties and technical parameters. The description of the experiments will be done insofar as they will be needed for a full comprehension of this work.

2.1 Accelerator facilities at GSI

Since 1975 GSI has been operating an accelerator facility for ions having masses spanning between ^{4}He and ^{238}U. The heavy ions synchrotron SIS and the experimental storage ring ESR have been put into operation since 1990 as a first upgrade of the structure. Fig. 2.1 shows a global overview of the accelerator facility of GSI.

The ions that must be accelerated are produced first in one of the ion sources (Penning, Chordis, or Mevva depending upon the desired ion species) from one of the two injectors. After a first bending section for charge and mass separation, the ions are injected into the UNILAC. The first part of the UNILAC consists now of a new 36 MHz high current injector (made up of RFQ's - Radio Frequency Quadrupoles), which should be able to produce an accelerating voltage 2.5 times stronger than the one formerly obtained with the Wideroe structures on the same path length. The energy of the ions at the end of this section must be ~ 1.4 MeV/u, before they get further ionized through a stripping foil. The advantages of the new high current injector with respect to the former Wideroe structure are essentially:

- More particles can be accelerated through this section because lower charge state ions can be brought up to the desired energy level, the accelerating voltage being up to 2.5 times bigger (the ion sources always produce lower charge state ions in larger amounts);

- Any space charge inconvenience across this section is limited thanks to the lower charge state of the transported ions, in spite of their higher number.

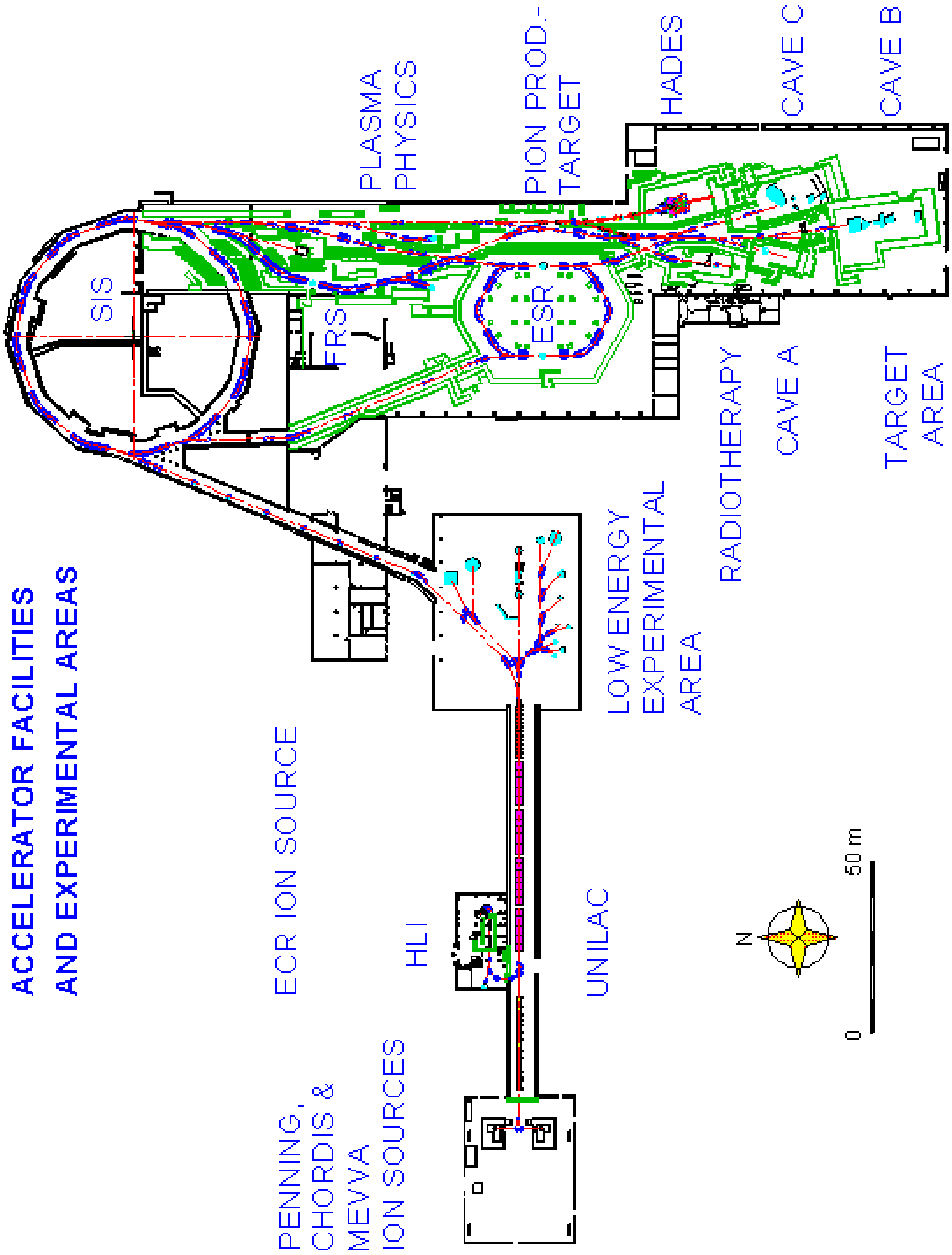

Figure 2.1: Global overview on the GSI accelerator complex.

The pre-accelerated ions will be then converted to a higher charge state by means of a stripping foil, and subsequently injected into the following Alvarez-accelerator, which works at a frequency of 108 MHz (4×27 MHz). The final energy of the UNILAC is normally 11.4 MeV/u, but it may as well be differently set by simply choosing a different phase relation between the fields oscillating in subsequent HF-cavities. After 110 m acceleration, the beam is according to necessity injected into one of the three low energy experimental areas, or it is bent into the transfer channel towards the Schwer-Ionen-Synchrotron SIS.

The linear accelerator UNILAC works as injector machine for the heavy ion synchrotron SIS (circumference 217 m, energies reached up to 2.1 GeV/u for ions with $Q/A = 0.5$). In fact, the ions that have reached the energy level of 11.4 MeV/u either are shot into the SIS over one single revolution (single-turn injection), or they get accumulated therein over several revolutions (multi-turn injection). The injection energy is sufficient to get the light ions (up to $Z \simeq 28$) fully stripped by means of a "Stripping Target" situated before the injection point; heavier ions are not completely ionized at this stage. In the SIS the ions are eventually accelerated to the beam energies which are required for the respective experiment. The magnetic rigidity of the SIS is $B\rho = 18$ Tm, and thus the maximum energy that can be reached is limited to 2.1 GeV/u for lighter particles, whereas it strongly depends upon ion mass and its charge state for heavier not fully ionized particles (for instance, 1 GeV/u can be reached for U^{73+}).

After acceleration and extraction from the SIS, it is possible to finally guide the beam to one of the different experimental areas, or inject it into the storage ring ESR, or send it to the treatment area for the heavy ion therapy for cancers [48]. According to the application, the beam can be extracted from the SIS either quickly (within one revolution), or slowly (over some seconds). There exist two possibilities of beam transfer from the SIS to the ESR or to the experimental areas: either the beam goes directly, or it is guided through the fragment separator FRS [49]. There the fragments coming from a production target can be selected according to their masses or charges, in order to produce in this way beams of exotic particles. Along the line which connects the SIS to the ESR, one more Cu Stripping-Target of medium thickness (0.01 to 0.1 g/cm^2) is also installed, which is able to strip off all the electrons even from heavier ion sorts if the energy of the beam is high enough.

In the ESR [50], ions suitable for experiments in the fields of atomic or nuclear physics, as well as for beam physics measurements and observations, can be stored for quite long times. Besides an electron cooler, a Gas-Jet-Target and a Nd:YAG-laser beam are also available there. Details about the ESR and its characteristics will be given in the next subsection 2.1.2. After being stored in the ESR, the beam can eventually be re-injected from the ESR to SIS for further acceleration, or it might as well be ejected and directed to the experimental areas.

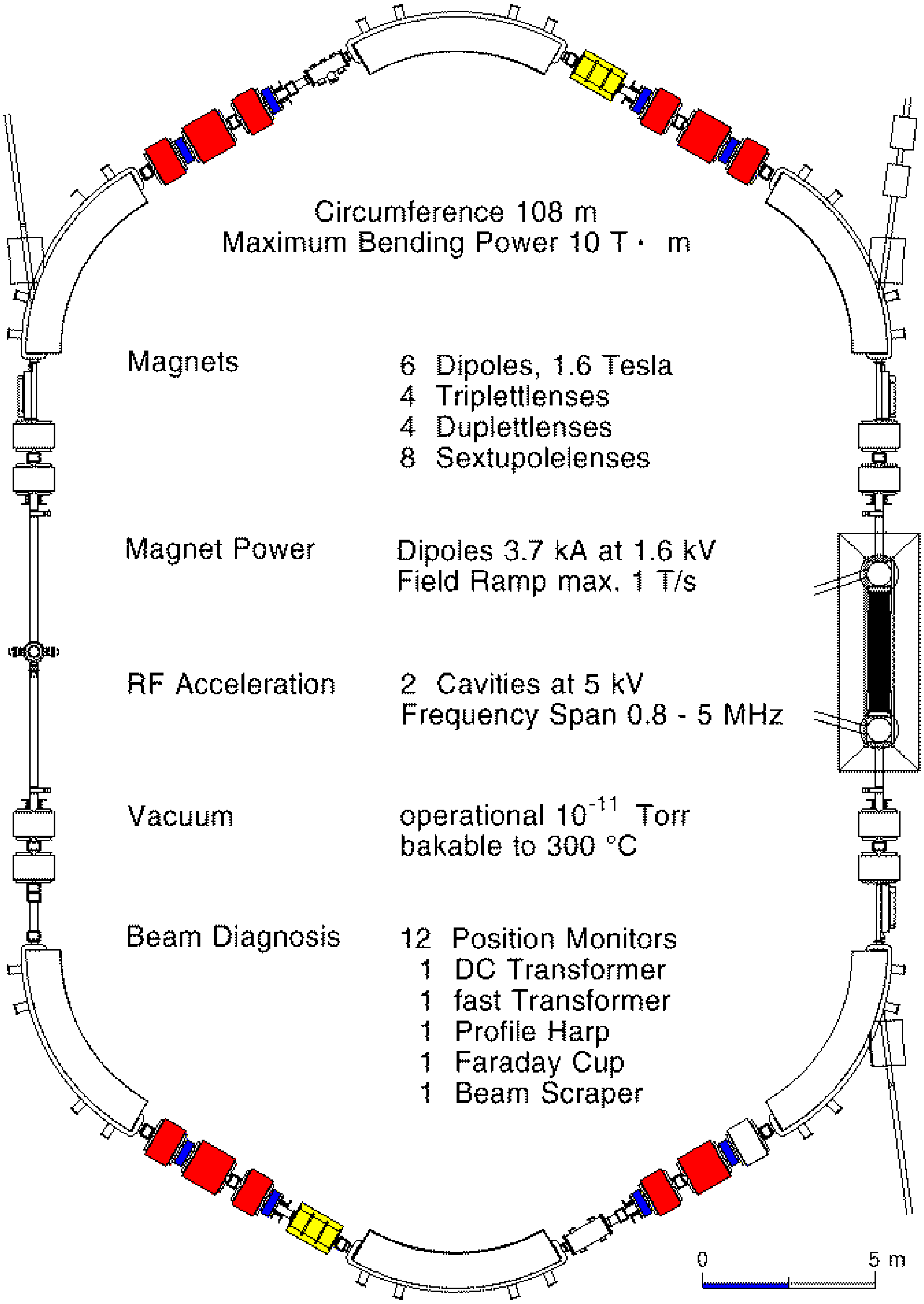

Figure 2.2: Overview of the heavy ion storage ring ESR and list of its main components.

Circumference	108.36 m
Magnetic rigidity	0.5 – 10 Tm
Ion species	C^{+6} to U^{92+}, radioactive beams
Energy range	3.0 – 560 MeV/u for U^{92+}
	3.0 – 840 MeV/u for ions with $Q/A = 0.5$
Maximum beam current	20 mA
Horizontal betatron tune	$Q_{\mathrm{x}} \simeq 2.31$
Vertical betatron tune	$Q_{\mathrm{y}} \simeq 2.30$
Transition point	$\gamma_{\mathrm{t}} \simeq 2.7$
Full momentum acceptance	$(\Delta p/p_0)_{\mathrm{max}} \approx 2.5\%$
Bending magnets:	
Number × angle	6×60^o
Bending radius	6.25 m
Used aperture ($h \times v$)	220×70 mm^2
Quadrupole magnets:	
Families × no.	10×2
Field gradient	0.31 – 6.1 T/m
Used aperture ($h \times v$)	300×120 mm^2
Sextupoles (families × no.)	2×4
Working pressure in the pipe	5×10^{-11} mbar

Table 2.1: Overview on technical and physical parameters for the ESR.

2.2 The Experimental Heavy Ion Storage Ring ESR

The layout of the ESR with its major components is shown schematically in Fig. 2.2 and the most important ring parameters are listed in Table 2.1. With respect to detailed information on design considerations and technical parameters described in Ref. [51], only a brief overview on characteristic features of the ESR is given here:

- The maximum *magnetic bending power of* $B \times \rho = 10$ Tm makes the ESR capable to accept fully stripped uranium ions at a maximum *specific ion energy of* 560 MeV/u. At present, the beam energy is limited for electron-cooled ion beams to values ≤ 400 MeV/u, because the maximum accelerating voltage at the electron cooler is restricted to about 210 keV.

- The *large momentum acceptance* $(\Delta p/p)_{\mathrm{max}}$ *of about 2.5%* (in the usual ion optical mode) makes the ring well suited for beam accumulation by applying the RF-stacking technique [52] as well as for accepting multi-component beams containing ions of rather different magnetic stiffness [52] – very useful for Schottky mass spectrometry [53].

- *Large transverse acceptances* in connection with the large $(\Delta p/p)_{\mathrm{max}}$ are, in addition, helpful for efficient injection and storage of "hot" secondary beams of nuclear fragments delivered by the FRS.

- *Electron cooling* is routinely applied at the ESR [54] for beam cooling in the longitudinal as well as transverse directions. Because the electron cooling time amounts to up to several minutes for "hot" fragment beams delivered by the FRS, additional *stochastic pre-cooling* is foreseen to speed up the cooling. Commissioning of the stochastic cooling system has recently started [56].

- A *supersonic gas jet* of about 5 mm diameter crossing the circulating ion beam in vertical direction is applied as *internal target* [57]. At maximum jet density of approximately 1×10^{13} cm^{-3} luminosity values between 10^{27} cm^{-2} s^{-1} for secondary (fragment) beams and 10^{30} cm^{-2}s^{-1} can be attained. The internal target was used for example in the experiments described in Ref. [53] to produce projectile-near nuclear fragments by projectile-fragmentation reactions. A more detailed description of the ESR internal gas-jet target will be given later in this chapter.

- The average *ultra-high vacuum (UHV) pressure is typically* 5×10^{-11} mbar (without internal target operation). *Beam life-times of up to several hours* are achieved, depending on the charge state of the stored ions and the electron cooler current. The beam loss rates are determined by radiative recombination between ions and cooler electrons rather than by interaction with residual gas atoms.

- Extremely *sensitive non-destructive beam diagnostics* is available with Schottky diagnosis and BTF (Beam Transfer Function) measurements. The ESR Schottky diagnosis system [58] is sensitive to a single stored highly charged ion.

The ESR is arranged as a doubly mirror symmetric stretched hexagon with a design circumference of 108.36 m, half the circumference of the SIS. The two long straight sections are provided for electron cooling – possibly laser cooling – and internal experiments around the internal target apparatus. The *six 60°-bending magnets* are fed in series by a single power supply. The bending field can be varied by 1 T/s from 0.08 T at 170 A excitation current to 1.6 T at 3600 A. The beam focusing is performed by *20 quadrupole magnets* arranged in *4 triplets* (two in either of the arcs) and *4 doublets* (two in either of the two long straight sections). Highly flexible ion optics is achieved by means of 10 independently controlled quadrupole power supplies. In terms of synchrotron lattice parameters, the ring may be operated either far below transition (i.e. $\gamma_{\mathrm{t}} < \gamma$) with maximum momentum acceptance, or at $\gamma_{\mathrm{t}} = \gamma$ with essentially reduced $(\Delta p/p)_{\mathrm{max}}$. As we can see from Fig. 2.2, the ESR has two cavities that can be used for beam bunching. These are cavities loaded with ferrite, such as to be able to sustain even relatively low frequency fields for the beam bunching at low harmonic numbers. In the ordinary ESR operation, one of the two cavities is constantly kept short circuited, whereas only the other one is constantly used for bunching purposes. Due to the high-revolution frequency of the ions within the storage ring of about 10^6 s^{-1}, even collisions processes with tiny reaction cross section (0.1 barn or smaller) are accessible at the ESR.

2.2.1 The Electron Cooler in the ESR

The ESR storage ring offers the unique opportunity to store and cool fully stripped heavy ions up to uranium at energies between 50 and 370 MeV/u. By beam cooling the phase space density of the ion beams can be improved by several orders of magnitude. The commonly used technique for phase space compression is electron cooling.

Electron cooling is based on the Coulomb interaction of the circulating ions with the electrons in the cooler; is a fast process for shrinking the size the divergence and the energy spread of the stored charged-particle beams without removing particles from the beam. It is achieved by combining a circulating beam with a monochromatic and well directed electron beam over a certain distance in a section of a storage ring. The electrons are continously produced in an electron gun with a heated cathode. They are accelerated electrostatically to a velocity equal to the average ion velocity, and are inflected into the ion beam. Both beams overlap over a certain length. At the end of the section, the electrons are separated again from the ion beam. The ions traverse under different angles and velocities the stream of parallel electrons, all moving with the same velocity. In a frame moving with the velocity of electrons, the latter are at rest, while the ions passing through the electron gas with a variety of velocities, from every direction, resemble the motion of particles in a hot gas. The ions undergo Rutherford scattering in the gas and lose energy. The heat is transferred to the electrons through this Coulomb interaction. The motion of the ions in the rest frame is reduced. Owing to the reduction of the velocity vector, the distribution of the ion velocities in the rest frame will become narrower in all three space dimensions, which means that the temperature of the ion beam will decrease.

Electron cooling improves the quality of the hot ion beam which has passed one or more stripper foils and can also compensate for heating effects in the storage ring. The main heating source for the cold ion beam is the intrabeam scattering, but also the heating by internal targets used in many storage rings experiments can be balanced.

Electron cooling is applied over a wide energy range from 290 keV/u up to 370 MeV/u for the heaviest ion species [59]. Cooling times of order 100 milliseconds for hot ion beams have been achieved decreasing to milliseconds for the cooled beam in equilibrium with heating by intrabeam scattering. The equilibrium emittances of the cooled ion beam are usually bellow 1 π mm mrad, momentum spreads of order 10^{-6} to 10^{-4} of the cooled ion beam have been demonstrated. Laser cooling in storage rings can presently cool the longitudinal temperature only providing longitudinal temperatures in the sub-Kelvin range, but limited to a few single charged ions. A schematic representation of the electron cooler in ESR is presented in Fig. 2.3.

The strength of cooling at relativistic energies is extremely sensitive to the fine tuning of the electron beam alignment in the cooling section. The electron currents currently applied are between 0.2 and 0.5 A. This range of electron currents was a trade off between better beam quality for higher electron currents and increased

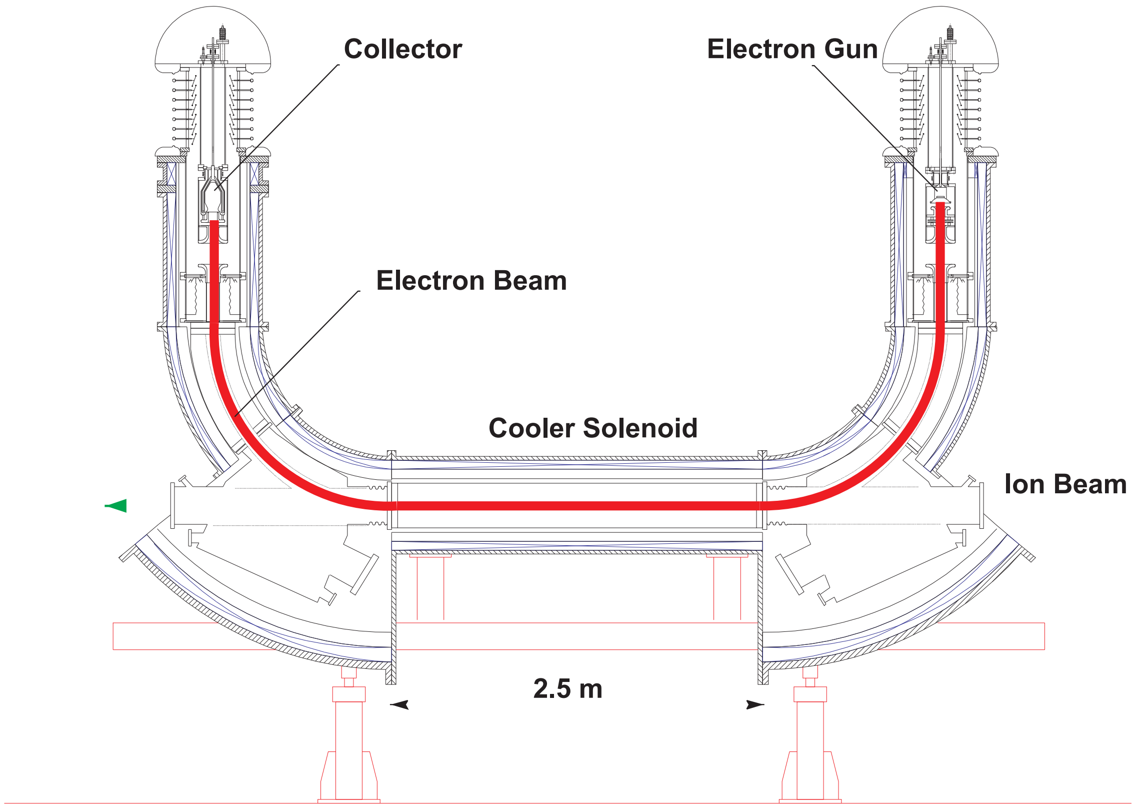

Figure 2.3: Schematic figure of the ESR electron cooler

beam lifetime for smaller electron currents, due to radiative electron capture. Electron currents exceeding 1 A were prevented by electron beam instabilities. The quality of the cooled beam was determined by a balance between the cooling rate and heating due to the intrabeam scattering. The equilibrium depends on both the intensity of the ion and the electron beam. The momentum spread of the cooled ion beam increases for a certain electron current with a $N^{0.3}$- dependence on the number of stored ions N, the transverse emittance grows proportional to $N^{0.6}$. The reduction of the momentum spread can be attributed to a change of the state of the beam from a gaseous phase to a liquid like phase. This reduction is most pronounced for ions with high charge. The potential force which acts as repulsive force between the ions increases with the square of the charge whereas the temperature is only proportional to the ion mass. For small numbers of stored ions (below a few thousand) a suppression of intrabeam scattering was observed [60]. This results in an extremely small momentum spread ($\delta p/p \leq 1 \times 10^{-6}$) and allows experiments with extraordinary resolution. The electron cooling technique provides cooled and intense beams of unprecedented quality, with precisely known energies, charge states, momentum spread and beam diameters close to 1 mm.

2.2.2 The internal ESR gas-jet target

Another experimental facility in the ESR storage ring is the internal gas-jet target, which provides an important tool for a broad range of atomic as well as nuclear physics experiments. Here the interaction of brilliant beams with matter can be uniquely studied with single-collision.

The provided gas densities can be compared with a typical density of a solid-state target of about 10^{21} particles/cm^3 [61]. The target delivers molecular densities in the range of : 10^{12} - 10^{14} cm^{-3} of various gases, with 5.0 mm diameter and 70 mm height in an UHV (ultra high vacuum) surrounding of 5×10^{-9} mbar, with an interaction length of 3-5 mm. As specified before, the main loss mechanism for highly charged ions is electron capture or interaction to the residual gas, therefore the most critical boundary condition for the operation of an internal target is the UHV system of the ESR (base pressure 10^{-11} mbar) which must remain almost unaffected. The densities of the targets vary as function of the target gas; from $\approx 2 \times 10^{12}$cm^{-3} for light gases up to 5×10^{13}cm^{-3} for heavy gases. The option to deliver high intensity gas-targets of very different gas species, reaching from light gases (He, H_2) and medium weight gases (N_2, CH_4) up to heavy noble gases (Xe, Kr), made it necessary to install an oil-free, multi-stage mechanical pumping system of high compression and pumping speed. Expensive noble gases are cleaned and recompressed in a recycling unit, the use of inflammable gases is controlled by a safety system.

In the reaction chamber the stored ions cross a perpendiculary oriented molecular or atomic supersonic gas jet. The jet is produced by expanding a gas through a Laval nozzle of 0.1 mm in diameter. To meet the UHV requirements of the ESR, the actual setup consists of an injection and a dump part, both separated by skimmers in four stages of differential pumping system. The diameter of the gas-jet in the reaction chamber amounts to about 5 mm. In Fig. 2.4 a schematic picture of the gas-jet is shown. The first stage of the injection part with nozzle and first skimmer is pumped by a system of roots pumps, with pumping speeds of 12000 m^3/h, 2000 m^3/h, 500 m^3/h, 200 m^3/h, 40 m^3/h for oil-free compression to atmosphere pressure. The maximum gasload to this stage to this is 300 mbar l/s for all gas species in use. The remaining three stages of the injection part and the four stages of the gas-jet dump are pumped by a differential pumping system of turbo-pumps. To perform standard services without breaking the ESR vacuum, the injection part and gas-jet dump can be separated from the interaction chamber by the use of two UHV compatible valves. The pass of the free jet in the UHV of the interaction chamber is 70 mm. The installation of the large pumping speed at the injection part made it necessary to choose a distance between the nozzle and the interaction point of approximately 500 mm. With an interaction length of 5 mm, the geometric acceptance of the skimmer system is approximately 1 mrad.

To operate with the target with very different gas species at optimum performance, the distance of the nozzle to the first skimmer can be adjusted 3-dimensionally via remote control. Typical distances between nozzle and first skimmer are 40 mm for light gases and 80 mm for heavy gases. To optimize the overlap between ESR-ion beam and target, the counting rate of photons detected from the interaction point, detected by a photomultiplier, is maximized by shifting the position of the ESR-ion beam. As a further and new option, the nozzle can be now cooled with liquid

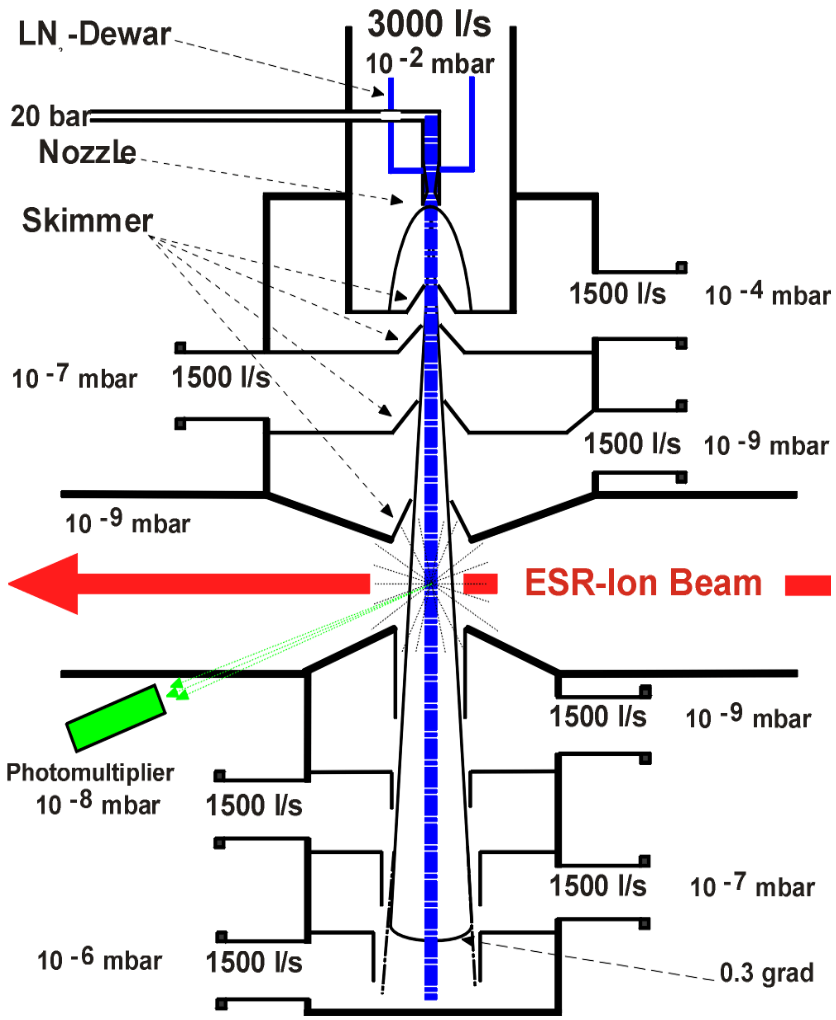

Figure 2.4: Schematic figure of the ESR internal gas-jet target

nitrogen to a temperature of 77 K. The stagnation pressure can be varied between 100 mbar and 20 bar, depending on the nozzle geometry and the gas species in use. This leads to clusters for light gases especially for hydrogen. As a consequence, the target density is increased with two orders of magnitude [62].

An example of experimental setup at the gas-jet target is shown in Fig. 2.5. In this experiment, charge exchange cross sections were studied for He-like uranium ions at

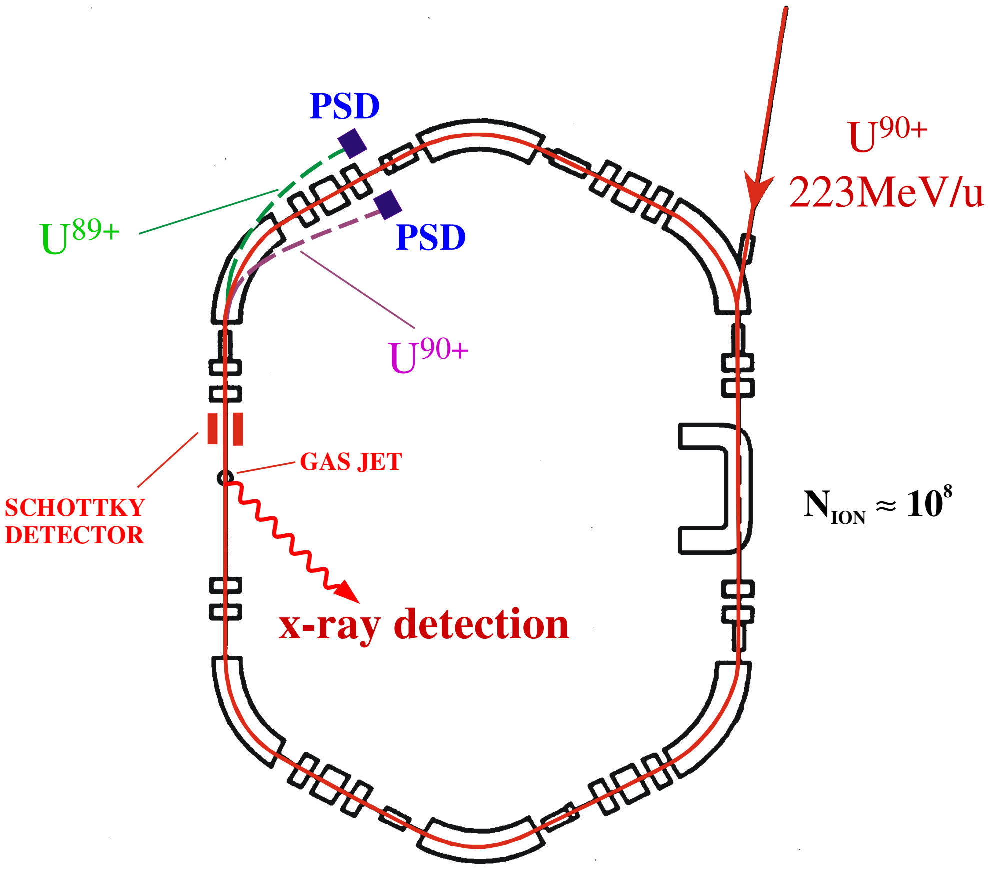

Figure 2.5: ESR storage ring at GSI and experimental setup for charge exchange experiment with U^{90+} at 223 MeV/u.

the ESR storage ring. The electron pickup cross sections were obtained in collisions of 223 MeV/u U^{90+} with N_2, Ar, Kr and Xe gaseous targets.

The results provide an experimental basis for estimates of beam losses at accelerator facilities exploiting highly charged decelerated heavy ions. Such data are urgently needed, since for He-like high-Z ions neither reliable relativistic theoretical estimates nor experimental data on total charge-exchange cross sections exist. The study of electron-capture processes by U^{90+} ions was performed at the heavy-ion synchrotron and storage ring facility SIS and ESR. He-like uranium ions, delivered by the SIS with an initial energy of 358 MeV/u, were stacked and accumulated in the ESR storage ring. In the electron-cooler device, the ions were cooled to the final beam energy of 223 MeV/u by an electron beam of 200 mA providing U^{90+} ions with a relative momentum spread of about 5×10^{-5} .More detailed description of the experiment, the results and comparison with theory will be done later on in chapter 6.

In Fig. 2.6, a scheme of the present experimental arrangement at the ESR gas-jet target is depicted. With this setup, complete angular distribution studies are now accessible for the first time [4]. Various x-ray detectors viewing the gas-jet/beam

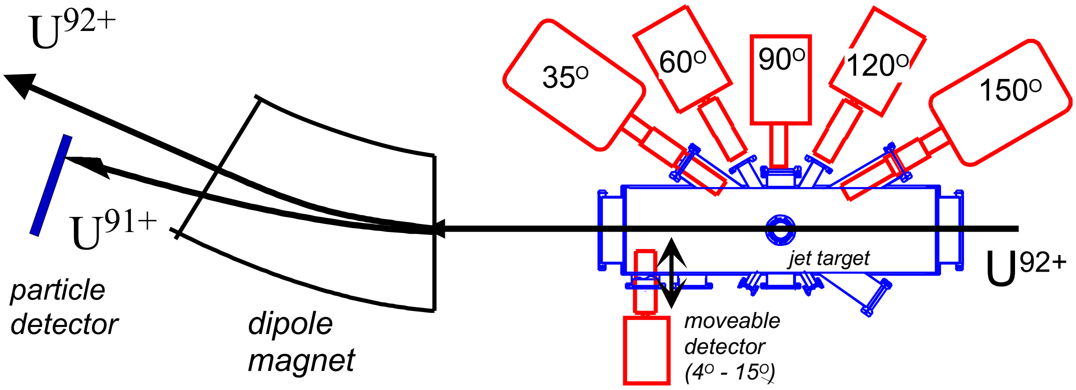

Figure 2.6: Layout of the experimental arrangement at the ESR-jet target. Photon emission is observed in coincidence with the down-charged ions, detected in a particle counter behind the dipole magnet.

interaction zone at different observation angles whereby covering the range from almost 0° to almost 180° [81].

With the present concept, the ESR Internal Target meets the unique boundary conditions for the operation of an internal gas jet target at the ESR.

Chapter 3

RR cross sections and rate coefficients - recombination in the low energy regime

Radiative recombination (RR) is one of the most important interaction processes in collisions of highly-charged heavy ions with free electrons or light target atoms, where RR is a good approximation for radiative electron capture (REC). The electron capture into the bound state of the moving projectile, with the simultaneous emission of a photon is in the projectile frame the radiative recombination of the ion with free electrons moving towards it with the corresponding velocity v. This process reversed in time is the photoionization process, in which the photon with energy $h\nu$ hits the projectile atom and ejects an electron with velocity v. Radiative recombination is in this way an useful tool in the experimental study of the photoeffect, especially in the special cases where such investigations are not possible in the direct channel, e.g. for high-Z ions and low interaction energies.

3.1 The dipole approximation

The differential and the total cross sections for the photoionization process have been calculated by Stobbe within a nonrelativistic dipole approximation [1], and are treated in detail in many textbooks [11] and papers [63, 64]. From these cross sections the corresponding REC cross sections can be easily obtained by the principle of detailed balance. Within this thesis a computer code has been developed based on a technique of Burgess [64], which calculates state selective REC cross sections within this approximation, as a function of the nuclear charge and the collision energy of a bare ion with respect to electrons assumed to be at rest in the laboratory frame. The results will be then compared with other nonrelativistic approaches and with the complete relativistic calculations.
The cross section for K shell ionization is given by an analytical formula which, owing to its simplicity, is still widely used today. The matrix element within this approach is given by

$$M_{fi}^{\mathrm{Stobbe}} = \langle \mathbf{p} m_s | \mathbf{r} \cdot \hat{\mathbf{u}}_\lambda | \mathbf{j_i} \mu_\mathbf{i} \rangle, \tag{3.1}$$

where $\mathbf{p}$ and m_s describe the asymptotic momentum and spin projection of the emitted electron, respectively, $\hat{\mathbf{u}}$ is the unit polarization vector of the photon, and j_i, μ_i define the initial bound state.
Let us consider now the ionization by photons of energy $h\nu$ of a hydrogenic atom or ion initially in the state specified by the principal quantum number n and angular momentum quantum number l. The ejected electron energy k^2 in units of the ionization energy of hydrogen I_H (or, equivalently, in Rydberg units of energy) is given by the energy conservation condition $h\nu = (Z^2/n^2+k^2)I_H$, where $(Z^2/n^2)I_H = |\epsilon_b|$, with ϵ_b being the binding energy of the initial state . The photoionization cross section may be written in the form [64]

$$\sigma_{nl}^{ph}(\kappa^2) = \left(\frac{4\pi\alpha a_0^2}{3}\right)\frac{n^2}{Z^2}\sum_{l'=l\pm1}\frac{l_>}{2l+I}\,\Theta(n,l;\kappa,l') \tag{3.2}$$

with

$$\Theta(n,l;\kappa,l') = (I+n^2\kappa^2)|g(n,l;\kappa,l')|^2 \tag{3.3}$$

where $g(n,l;\kappa,l')$ are the dipole bound-free matrix elements, mentioned above for the case $n=1$ (3.1)

$$g(n,l;\kappa,l') = \frac{z^2}{n^2}\int_0^\infty P_{nl}(r)rF_{kl}(r)dr, \tag{3.4}$$

where l' is the orbital angular momentum quantum number of the ejected electron, $l_>$ the greater of l and l', κ is k/Z, α is the fine structure constant and a_0 is the Bohr radius. In (3.3), $P_{nl}(r)$ and $F_{nl}(r)$ are respectively the initial and final radial wave functions of the electron, which satisfy

$$\left[\frac{l(l+1)}{r^2}+\frac{2Z}{r}+\begin{pmatrix}-Z^2/n^2\\ k^2\end{pmatrix}\right]\begin{pmatrix}P_{nl}(r)\\ F_{kl}(r)\end{pmatrix} = 0 \tag{3.5}$$

and are normalized such that

$$\int_0^\infty P_{nl}(r)P_{n'l}(r)dr = \delta_{nn'} \tag{3.6}$$

and

$$\int_0^\infty F_{kl}F_{k'l}(r)dr = \pi\delta(k^2-k^{'2}). \tag{3.7}$$

Explicitly they may be written [2]:

$$P_{nl}(\rho) = \sqrt{\frac{(n+l)!}{(n-l-1)!}}\left(\frac{2\rho}{n}\right)^{l+1}\frac{e^{-\rho/n}}{n(2l+1)!}\quad {}_1F_1\left(l+1-n;2l+2;\frac{2\rho}{n}\right) \tag{3.8}$$

and

$$F_{kl}(\rho) = \sqrt{\frac{\pi}{2(1-e^{-2\pi/\kappa})}\prod_{s=0}^{l}(1+s^2\kappa^2)}\quad e^{i\kappa\rho}\quad {}_1F_1(l+1-i/\kappa;2l+2;-2i\kappa\rho) \tag{3.9}$$

The integral (3.4) may be evaluated by choosing convenient integral representations for the degenerate hypergeometric functions in (3.5) and (3.6) and changing the order of integration to perform the integration over ρ first. The resulting integral can be then expressed in terms of hypergeometric functions. The result has been given by several authors: Gordon [2], Biedenharn , McHale and Thaler [65], and Alder and Winther [66]. After simplifying, we have

$$\begin{aligned} g(n,l;\kappa,l'=l\pm 1) &= \sqrt{\tfrac{\pi}{2}\tfrac{(n+l)!}{(n-l-1)!(1-e^{2\pi/\kappa})}\prod_{s=0}^{l'}(1+s^2\kappa^2)} \\ &\times\left(\tfrac{4n}{1+n^2\kappa^2}\right)^{l_<+1}\tfrac{exp\left[-\frac{2}{\kappa}arctan(n\kappa)\right]}{4n^2(2l\pm1)!}Y_\pm \end{aligned} \tag{3.10}$$

where

$$\begin{aligned} Y_+ &= i\eta\left(\tfrac{n-i\eta}{n+i\eta}\right)^{n-l}\Big[{}_2F_1\left(l+1-n,l-i\eta;2l+2;\tfrac{-4ni\eta}{(n-i\eta)^2}\right) \\ &-\left(\tfrac{n+i\eta}{n-i\eta}\right)^2{}_2F_1\left(l+1-n,l+1-i\eta;2l+2;\tfrac{-4ni\eta}{(n-i\eta)^2}\right)\Big] \end{aligned} \tag{3.11}$$

and

$$\begin{aligned} Y_- &= i\eta\left(\tfrac{n-i\eta}{n+i\eta}\right)^{n-l-1}\Big[{}_2F_1\left(l-1-n,l-i\eta;2l;\tfrac{-4ni\eta}{(n-i\eta)^2}\right) \\ &-\left(\tfrac{n+i\eta}{n-i\eta}\right)^2{}_2F_1\left(l+1-n,l-i\eta;2l;\tfrac{-4ni\eta}{(n-i\eta)^2}\right)\Big] \end{aligned} \tag{3.12}$$

with $\eta = 1/\kappa$. Since the hypergeometric series involved in the equations (3.11) and (3.11) terminate after a finite number of terms due to the fact that the first variables are either zero or a negative integer, all the required $g(n,l;\kappa,l-1)$ could be calculated from (3.10) directly. However, this procedure is not suitable in general, because of the large number of terms occurring in the series when $n-l$ is large; also for some ranges of parameters, there is a gross cancellation between the terms of the series (see below). The following alternative procedure was adopted.
For given n and κ the following recurrence relations connect matrix elements having different values of l (see [64]),

$$\begin{aligned} &2n\sqrt{[n^2-(l-1)^2][1+l^2\kappa^2]}g(n,l-2;k,l-1) = [4n^2-4l^2+l(2l-1) \\ &\times(1+n^2\kappa^2)]g(n,l-1;\kappa,l) - 2n\sqrt{[n^2-l^2][1+(l+1)^2\kappa^2]}g(n,l;\kappa,l+1), \end{aligned} \tag{3.13}$$

$$\begin{aligned} &2n\sqrt{[n^2-l^2][1+(l-1)^2\kappa^2]}g(n,l-1;k,l-2) = [4n^2-4l^2+l(2l+1) \\ &\times(1+n^2\kappa^2)]g(n,l;\kappa,l-1) - 2n\sqrt{[n^2-(l+1)^2][1+l^2\kappa^2]}g(n,l+1;\kappa,l). \end{aligned} \tag{3.14}$$

Also, we note that when $l \approx n$, only a small number of terms occur in the hypergeometric series in (3.10), (3.11). In particular, when $l = n-1, n-2$ the expressions (3.9) to (3.11) simplify to give

$$g(n,n-1;0,n) = \sqrt{\frac{\pi}{2(2n-1)}}4(4n)^n e^{-2n} \tag{3.15}$$

$$g(n,n-1;\kappa,n)=\sqrt{\frac{\prod_{s=1}^{n}(1+s^2\kappa^2)}{1-e^{-2\pi/\kappa}}\frac{exp[2n-2\kappa^{-1}arctan(n\kappa)]}{(1+n^2\kappa^2)^{n+2}}}g(n,n-1;\kappa,n), \tag{3.16}$$

$$g(n,n-2;\kappa,n-1)=\frac{1}{2}\sqrt{(2n-1)(1+n^2\kappa^2)}g(n,n-1;\kappa,n), \tag{3.17}$$

$$g(n,n-1;\kappa,n-2)=\frac{1}{2n}\sqrt{\frac{i+n^2\kappa^2}{1+(n-1)^2\kappa^2}}g(n,n-1;\kappa,n), \tag{3.18}$$

$$g(n,n-2;k,n-3)=\frac{4+(n-1)(1+n^2\kappa^2)}{2n}\sqrt{\frac{2n-1}{1+(n-2)^2\kappa^2}}g(n,n-1;\kappa,n-2). \tag{3.19}$$

Equations (3.12) to (3.18) define completely the set of matrix elements required. A set of equations alternative to (3.12) to (3.18) which in many respects is more convenient may be obtained by putting

$$g(n,l;\kappa,l')=\sqrt{\frac{(n+l)!}{(n-l-1)!}}\prod_{s=0}^{l'}(1+s^2\kappa^2)(2n)^{l-n}G(n,l;\kappa,l') \tag{3.20}$$

and obtaining equations analogous to (3.14) to (3.18) defining $G(n,l;\kappa,l')$ for $l=n-1,n-2$. The quantities $G(n,l;\kappa,l')$ then satisfy the recurrence relations

$$\begin{aligned} G(n,l-2;\kappa,l-1) &= [4n^2-4l^2+l(2l-1)(1+n^2\kappa^2)]G(n,l-1;\kappa,l) \\ &\quad -4n^2(n^2-l^2)[1+(l+1)^2\kappa^2]G(n,l;\kappa,l-1), \end{aligned} \tag{3.21}$$

$$\begin{aligned} G(n,l-1;\kappa,l-2) &= [4n^2-4l^2+l(2l+1)(1+n^2\kappa^2)]G(n,l;\kappa,l-1) \\ &\quad -4n^2(n^2-(l+1)^2)[1+l^2\kappa^2]G(n,l+1;\kappa,l). \end{aligned} \tag{3.22}$$

Since repeated use of (3.21) and (3.22) obviously does not involve division or the evaluation of square roots, this scheme is very suitable for fast computing.

Due to the complicated expression of the dipole matrix elements (3.10), most of the nonrelativistic treatments used further approximations in order to calculate the RR cross section. However, this set of recurrence relations allowed us to write a Fortran code that generates the matrix elements $G(n,l;\kappa,l')$ and computes without any further approximation, first the cross section for the photoeffect $\sigma_{nl}^{ph}(\kappa^2)$ (3.2),(3.3), from which the cross section $\sigma_{nl}^{RR}(\kappa^2)$ for radiative recombination is immediately derived.

This is the cross section for capturing a free electron of energy κ^2 into a bound atomic state with main quantum number n and angular momentum quantum number l with the simultaneous emission of a photon of energy $h\nu$, for which the energy conservation condition is, like before for the time reversed process, $h\nu=\kappa^2+|\epsilon_b|$.

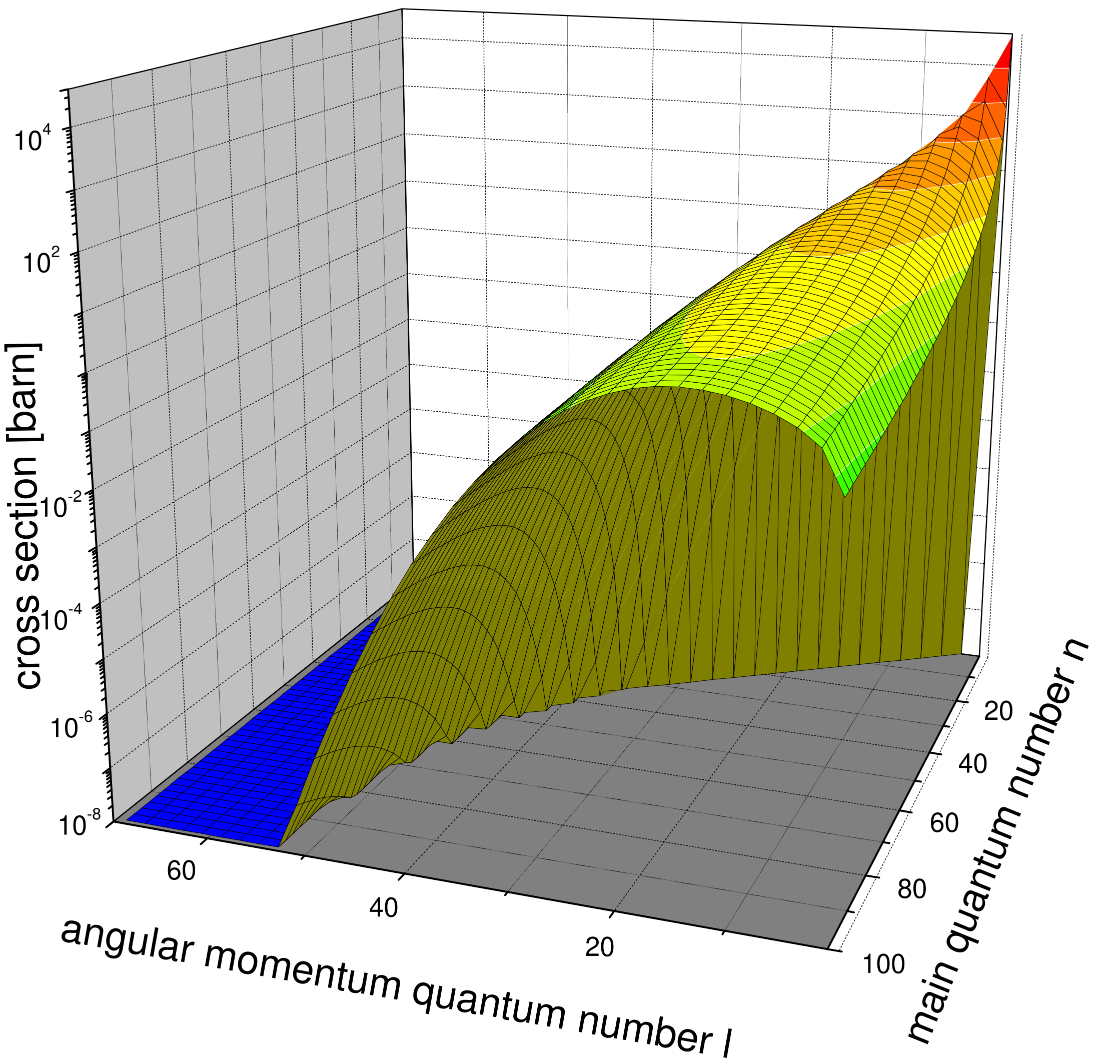

Figure 3.1: State selective total cross sections for radiative recombination into bare uranium ions at 0.1 MeV/u (corresponding to an electron kinetic energy of 54.86 keV) as a function of the principal and the angular momentum quantum numbers as calculated by the Fortran code.

By the principle of detailed balance, the cross section for radiative recombination into a vacant shell, in the nonrelativistic limit is written as

$$\sigma_{nl}^{RR}(\kappa^2) = \frac{(h\nu)^2}{\kappa^2}\frac{1}{2m_e c^2}\sigma_{nl}^{ph}(\kappa^2) \tag{3.23}$$

The RR cross sections are calculated for arbitrary n, l states, up to very high n (i.e. $n = 600$). Fig. 3.1 shows the cross sections as a function of n and l, for $Z = 92$ and $\kappa^2 = 54.86$ eV.

3.1.1 Comparison with other theoretical approaches

The results of the code developed in this thesis will be compared with other nonrelativistic results and with the exact relativistic theory for radiative recombination.

The radiative recombination process was studied theoretically, in the 1920s, by Kramers [67], Oppenheimer [68], Wessel [69], Stueckelberg and Morse [70]. In the early work of Stobbe, the cross sections for capture into the lowest hydrogenic levels were calculated analytically. Later Bethe and Salpeter [11] derived an approximate analytical formula for the cross section for RR for a fixed n state. In their work, advantage was taken of the fact that the oscillator strength crosses the continuum limit smoothly. Bethe and Salpeter obtained the following simple expression for the cross section for radiative recombination to a hydrogenic level with main quantum number n

$$\sigma_n = 2.10 \times 10^{-22} cm^2 \frac{Z^4 E_0^2}{nE_e(Z^2 E_0 + n^2 E_e)} \tag{3.24}$$

where E_e is the kinetic energy of the free electron, and E_0 is the Rydberg energy. Due to the approximate way Bethe and Salpeter derived formula (3.24), corrections must be applied for the lower states. For these states, where the largest cross sections were found, the more accurate calculations by Stobbe yield corrections (the so-called *Gaunt* factors) , which are about 20% for $n = 1$, 12% for $n = 2$ and 9% for $n = 3$. A comparison between the results of this code and Bethe and Salpeter's formula are shown in Fig. 3.2 for radiative recombination into the shells of U^{92+} ions (moving with 12.83 MeV/u towards at rest, corresponding to a relative kinetic electron energy of 10 eV).

Later the process was studied by several authors in the context of different experiments, and from the point of view of atomic physics planned at heavy-ion storage rings, it was discussed extensively by Liesen and Beyer [71] and Schuch *et al* [72]. Also, the influence on the radiative recombination process of the core electrons in not fully stripped ions was discussed by Hahn and Rule [73], Kim and Pratt [74] and McLaughlin and Hahn [75]. The last presented RR cross sections and rate coefficients for all ions using the scaling property of the cross section in the parameter $\eta = Z_{eff}/(ka_0)$ where Z_{eff} is the effective charge, expressed by an empirical formula, which is weakly dependent on the electron energy k^2.

Table (3.1) shows a comparison with these results, calculated for the pure Coulombic case and for fully stripped ions. The effective charge can be used safely in the code leading to the same agreement even for higher states, considering full or partially filled shells, but using McLaughlin and Hahn's formula for Z_{eff}.

In 1992, M.Pajek and R.Schuch [76] gave compact analytical results for state selective cross sections for radiative recombination of free electrons with bare ions, in the low-energy limit. They calculate the asymptotic expressions for the dipole matrix elements when $E_e/E_{nl} << 1$, where E_{nl} is the binding energy of the (n, l) state, showing that in this limit the RR cross section scales as $1/E_e$ and giving a simple analytical result for a fixed *arbitrary* (n, l) state:

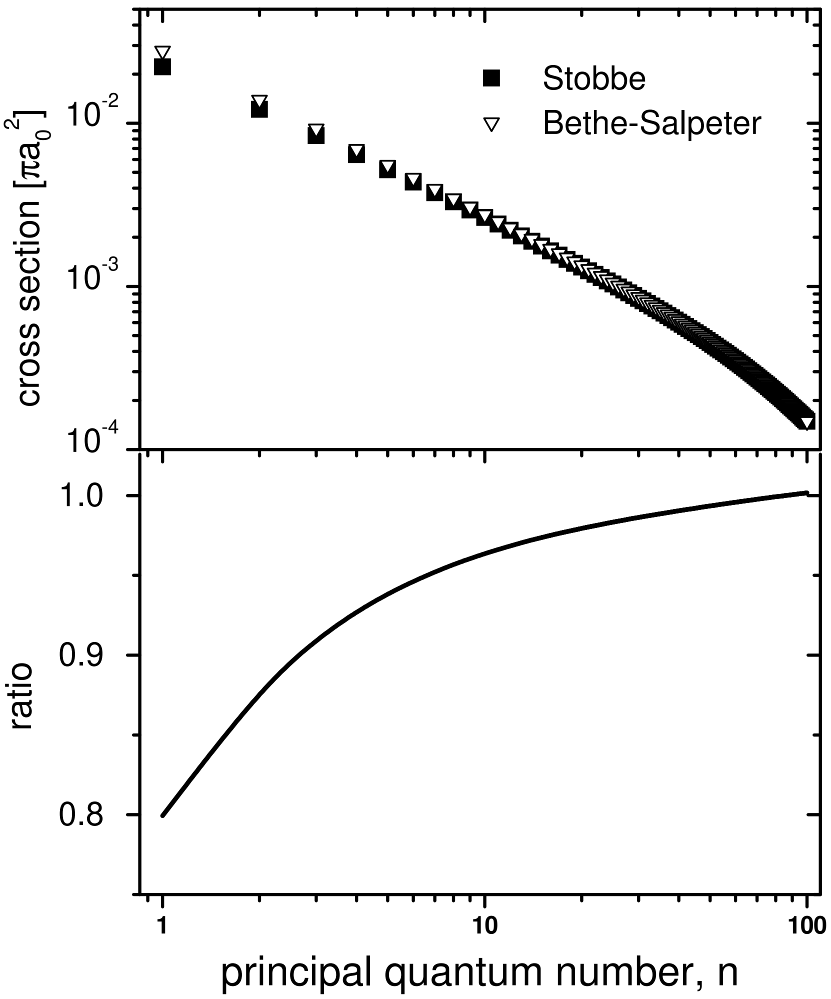

Figure 3.2: Comparison of total cross sections calculated in the Stobbe approximation (results of the code) and in Bethe and Salpeter approximation (3.24) (upper part), and the ratio $\sigma_{Stobbe}/\sigma_{BS}$ (lower part).

$$\sigma_{nl}(E_e) \approx \frac{E_{nl}}{E_e}\sigma(n,l), \tag{3.25}$$

where $\sigma(n,l)$ is introduced as the *reduced* RR cross section

$$\sigma(n,l) = \frac{\pi^2}{3}\alpha^3 a_0^2[(l+1)c_{l+1}^2(n,l) + lc_{l-1}^2(n,l)]. \tag{3.26}$$

.

The asymptotic behaviour of the cross section for $E_e/E_{nl} \to 0$ is shown in Fig. 3.3.

Table 3.1: Direct capture cross sections for capture into individual empty nl shells, $\sigma_{nl}^{R}R$, are given in units of πa_0^2 for values of the scaling parameter $\eta = 0.25, 1.0, 10.0$ and 100. The numbers in the square brackets are powers of ten.

nl η	0.25[75]	0.25	1.0[75]	1.0	10.0[75]	10.0	100.0[75]	100.0
1s	7.55[-9]	7.68[-9]	1.13[-6]	1.14[-6]	1.78[-4]	1.91[-4]	1.82[-2]	1.92[-2]
2s	9.57[-10]	9.75[-10]	1.59[-7]	1.61[-7]	2.81[-5]	2.81[-5]	2.82[-3]	2.82[-3]
2p	4.40[-11]	4.51[-11]	9.16[-8]	9.33[-8]	7.37[-5]	7.43[-5]	7.69[-3]	7.75[-3]
3s	2.85[-10]	2.90[-10]	4.89[-8]	4.96[-8]	9.56[-6]	9.45[-6]	9.58[-4]	9.48[-4]
3p	1.55[-11]	1.59[-11]	3.32[-8]	3.38[-9]	2.83[-5]	2.83[-5]	2.93[-3]	2.94[-3]
3d	1.03[-13]	1.23[-13]	3.79[-9]	3.89[-9]	2.99[-5]	3.01[-5]	3.38[-3]	3.40[-3]
4s	1.20[-10]	1.22[-10]	2.09[-8]	2.12[-8]	4.49[-6]	4.41[-6]	4.51[-4]	4.44[-4]
4p	6.90[-12]	7.08[-12]	1.50[-8]	1.52[-8]	1.36[-5]	1.35[-5]	1.41[-3]	1.41[-3]
4d	5.15[-14]	7.40[-14]	2.30[-9]	2.36[-9]	1.88[-5]	1.89[-5]	2.12[-3]	2.13[-3]
4f	0.00[00]	2.17[-16]	1.01[-10]	1.04[-10]	1.20[-5]	1.22[-5]	1.57[-3]	1.59[-3]
5s	6.15[-11]	6.27[-11]	1.08[-8]	1.09[-8]	2.51[-6]	2.45[-6]	2.53[-4]	2.49[-4]
5p	3.61[-12]	3.71[-12]	7.89[-9]	8.04[-9]	7.62[-6]	7.56[-6]	7.93[-4]	7.91[-4]
5d	5.15[-14]	4.35[-14]	1.35[-9]	1.39[-9]	1.15[-5]	1.15[-5]	1.30[-3]	1.30[-3]
5f	0.00[00]	1.86[-16]	8.65[-11]	9.00[-11]	1.06[-5]	1.07[-5]	1.39[-3]	1.40[-3]
5g	0.00[00]	2.58[-19]	2.06[-12]	1.92[-12]	4.68[-6]	4.72[-6]	7.59[-4]	7.65[-4]
6	3.78[-11]	3.85[-11]	1.18[-8]	1.20[-8]	2.84[-5]	2.87[-5]	3.73[-3]	3.78[-3]
7	2.37[-11]	2.42[-11]	7.51[-9]	7.63[-9]	2.28[-5]	2.27[-5]	2.80[-3]	3.26[-3]
8	1.60[-11]	1.62[-11]	5.06[-9]	5.14[-9]	1.75[-5]	1.82[-5]	2.08[-3]	2.86[-3]
9	1.12[-11]	1.14[-11]	3.57[-9]	3.63[-9]	1.44[-5]	1.47[-5]	1.45[-3]	2.55[-3]
10	8.19[-12]	8.32[-12]	2.61[-9]	2.65[-9]	1.05[-5]	1.21[-5]	1.06[-3]	2.30[-3]

[75] McLaughlin and Hahn

Table (3.2) shows a good agreement, for three different values for E_e/E_{nl} where $E_{nl} = Z^2 E_0/n^2$ and $Z = 92$.

In recent years, an exact relativistic formulation [63] has been implemented that takes into account a relativistic motion of the electron both in the bound and in

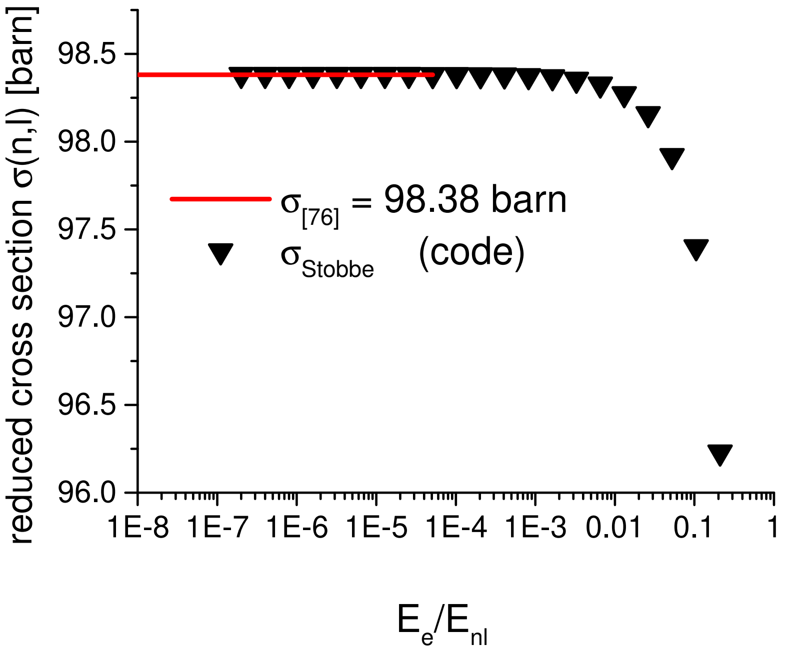

Figure 3.3: Reduced cross sections for RR into $2s_{1/2}$ as a function of the ratio E_e/E_{nl} between the kinetic energy of the electron and the binding energy of the level in which the latter is captured. Comparison between the results of the code (Stobbe theory) and the asymptotic value calculated by Pajek and Schuch [76].

the continuum state subject to the Coulomb field of the nucleus. Moreover, all multipoles in the electron-photon interaction, i.e. retardation effects are included. The corresponding matrix element mentioned above,(3.1) is given in this case by

$$M_{fi}^{\text{exact}} = \langle \mathbf{pm_s} | \alpha \cdot \hat{\mathbf{u}}_\lambda \mathbf{e^{ik}} \cdot \mathbf{r} | \kappa_\mathbf{i} \mu_\mathbf{i} \rangle, \tag{3.27}$$

with the initial and final states now defined as Coulomb-Dirac eigenstates. The quantity α denotes the Dirac matrix and the exponential describes the photon wave function with wave vector $\mathbf{k}$. The differential cross section within this approach is, for a single electron

$$\frac{d\sigma_{ph}}{d\Omega} = \frac{\alpha}{4\omega} \frac{1}{2j_b+1} \sum_{\mu_b} \sum_{m_s} |M_{\mathbf{p},b}(m_s, \lambda_+, \mu_b)|^2 \tag{3.28}$$

where

$$M_{\mathbf{p},b}(m_s, \lambda_+, \mu_b) = M_{fi}^{\text{exact}} \tag{3.29}$$

and where an average over the $(2j_b+1)$ angular momentum projections in the bound state and a summation over the spin projections $m_s = \pm\frac{1}{2}$ of the emitted electrons has been made. The transition matrix element can be written as

$$M_{\mathbf{p},b}(m_s, \lambda_+, \mu_b) = \int \psi^\dagger_{\mathbf{p},m_s}(\mathbf{r}) \alpha \cdot \hat{\mathbf{u}}_+ e^{i\mathbf{k}\cdot\mathbf{r}} \psi_{j_b\mu_b}(\mathbf{r}) d^3r, \tag{3.30}$$

Table 3.2: The reduced radiative recombination cross section σ_{nl} for n=1,2 and 3 (n,l) subshells for different E_e/E_{nl} and $Z = 92$ in comparison with the values obtained in the low-energy approximation $E \ll E_{nl}$ [76].

State (n,l)		$\sigma(n,l)$			$\sigma(n,l)^{[76]}$
E_e/E_{nl}	10^{-1}	10^{-2}	10^{-3}	10^{-5}	$\ll 1$
1 0	157.33	166.74	167.74	167.856	167.9
2 0	97.45	98.297	98.37	98.380	98.38
2 1	244.16	267.70	270.26	270.544	270.5
3 0	74.201	74.47	74.495	74.497	74.5
3 1	221.182	230.08	230.99	231.09	231.1
3 2	232.912	263.78	267.20	267.58	267.6

where $\hat{\mathbf{u}}_\lambda = \hat{\mathbf{u}}_+$ due to the fact that averaging over the circular polarizations of the incoming photon $\lambda_+ = 1$ and $\lambda_- = -1$ and summing over all μ_b and m_s is equivalent to taking one photon polarization, e.g. $\lambda_+ = 1$. and where

$$\begin{aligned}\psi_{\mathbf{p},m_s}(\mathbf{r}) &= 4\pi \sum_{\kappa,\mu} i^l e^{i\Delta_\kappa} \langle l, \mu - m_s, \frac{1}{2}, m_s | j, \mu\rangle Y^*_{l,\mu-m_s}(\theta, 0) \\ &\times \left\{ \begin{array}{c} g_\kappa(r)\chi^\mu_\kappa \\ i f_\kappa(r)\chi^\mu_{-\kappa} \end{array} \right\}\end{aligned}$$

is the partial-wave expansion of the wave function describing the relativistic electron emitted with asymptotic momentum $\mathbf{p}$ ($p^2 = E^2 - m_e c^2$, $p_z = pcos\theta$) and spin projection m_s with respect to the z-axis. The summation extends over the relativistic quantum number $\kappa = \pm(j + \frac{1}{2})$ and the angular momentum projection μ. Associated with κ are the orbital angular momenta l and l' of the upper and lower components, respectively. The χ^μ_κ are the usual normalized two-component spin angular functions, and the $g_\kappa(r)$ and $f_\kappa(r)$ are the (real) radial continuum wave functions. The Clebsch-Gordan coefficient in (3.1.1) mediates a projection onto the definite spin component m_s in the z direction and onto a definite orbital angular momentum l entering into the directional dependence expressed by $Y^*_{l,\mu-m_s}(\theta, 0)$. The bound state wave function is written as

$$\psi_{j_b,\mu_b}(\mathbf{r}) = \left(\begin{array}{c} g_b(r)\chi^{\mu_b}_{\kappa_b} \\ i f_b(r)\chi^{\mu_b}_{-\kappa_b} \end{array} \right) \tag{3.31}$$

After inserting the Raleigh expansion of the photon plane wave and performing the spinor algebra, the integrals over three spherical harmonics can be expressed by Clebsch-Gordan coefficients. The matrix element becomes

$$\begin{aligned} M_{\mathbf{p},b}(m_s, \lambda_+, \mu_b) &= 4\pi\sqrt{2} \sum_{L=0}^{\infty} \sum_{\kappa} i^{L+1-l} e^{i\Delta_\kappa} \\ &\times \langle l, \mu_b + 1 - m_s, \frac{1}{2}, m_s | j, \mu_b + 1\rangle F^+_{\mu_b}(L, \kappa) Y_{l,\mu_b+1-m_s}(\theta, 0), \end{aligned} \tag{3.32}$$

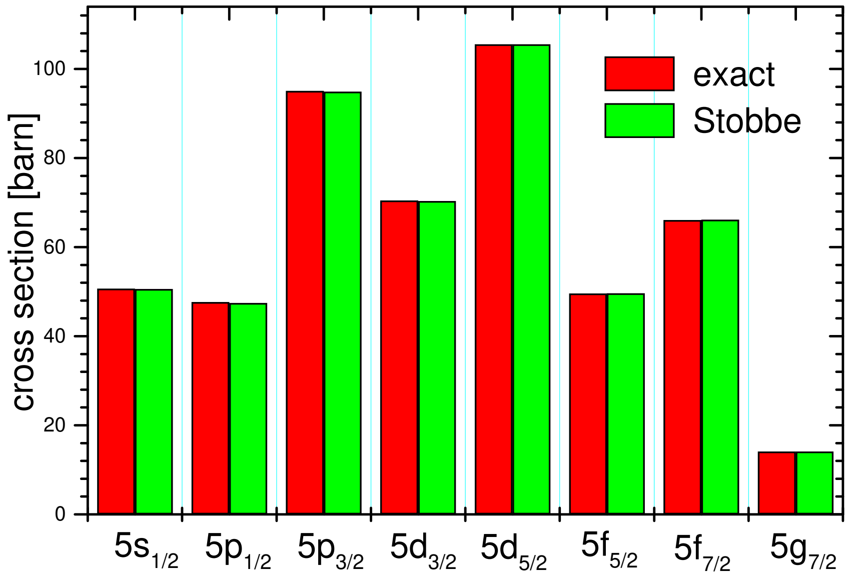

Figure 3.4: Comparison of total cross sections for radiative recombination into the $n = 5$ subshells of Ne^{10+} ions moving with 0.1 MeV/u towards electrons at rest calculated in the Stobbe approximation (code) and in an exact relativistic formulation [63].

where

$$F^{+}_{\mu_b}(L,\kappa) = \Big[A_L(j_b\mu_b j; l'_b l)\int_0^\infty g_\kappa(r) j_L(kr) f_b(r) r^2 dr - A_L(j_b\mu_b j; l_b l')\int_0^\infty f_\kappa(r) j_L(kr) g_b(r) r^2 dr\Big], \tag{3.33}$$

and

$$A_L(j_b\mu_b j; l_1 l_2) = (2L+1)\sqrt{\frac{2l_1+1}{2l_2+1}}\langle l_1, \mu_b + \frac{1}{2}, \frac{1}{2}, -\frac{1}{2}|j_b, \mu_b\rangle \times\langle l_2, \mu_b + \frac{1}{2}, \frac{1}{2}, -\frac{1}{2}|j_b, \mu_b + \frac{1}{2}\rangle\langle l_1, \mu_b + \frac{1}{2}, L, 0|l_2, \mu_b + \frac{1}{2}\rangle\langle l_1, 0, L, 0|l_2, 0\rangle. \tag{3.34}$$

The summations are limited by the selection rules included in the Clebsch-Gordan coefficients. Once the cross section $\sigma_{ph}(\omega', \theta')$ of the photoelectric effect in the projectile frame is computed, the cross section $\sigma_{RR}(E', \theta')$ for radiative recombination will be

$$\frac{d^2\sigma_{RR}(E',\theta')}{dE' d\Omega'_{ph}} = (2j_b+1)\frac{\omega'^2}{q'^2}\frac{d^2\sigma_{ph}(E',\theta')}{dE' d\Omega'_{el}} \tag{3.35}$$

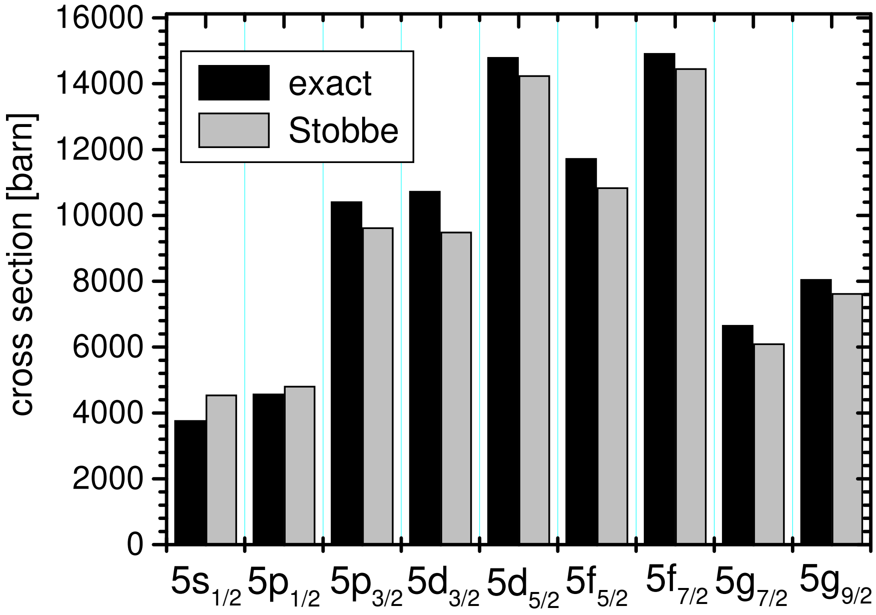

Figure 3.5: Same as Fig.3.4, but for U^{92+} ions moving with 0.1 MeV/u.

Here, the factor $(2j_b + 1)$ turns the averaging of (3.28) into a summation while the factor ω'^2/q'^2 replaces the phase space factor of the outgoing electron by that one of the emitted photon. In applications to relativistic ion-atom collisions, the z-direction is usually defined as the direction of the projectile motion. This is opposite to the direction of the electron momentum as seen from the projectile. Hence for REC, the angle θ' of the photoelectric effect or of the radiative recombination has to be replaced by $\pi - \theta'$, or cosθ' is replaced by - cosθ'. We will provide a comparison between the nonrelativistic results of our code and the complete relativistic formulation based on (3.28) and (3.1.1).

To this end, we first consider total cross sections as a function of the nuclear charge and of the collision energy of a bare ion with respect to electrons assumed to be at rest in the laboratory system.

For a low nuclear charge $Z = 10$, a principal quantum number $n = 5$ and a low projectile energy of 0.1 MeV/u (corresponding to a relative kinetic electron energy of 54.86 eV), it turns out that the non relativistic treatment and the relativistic formulation yield the same result within very close limits, as to be expected, see Fig. 3.4. However, retaining low relative velocities but choosing a high nuclear charge $Z = 92$, we obtain sizeable differences in the cross sections, see Fig. 3.5. This means that even for $n = 5$, relativistic effects in U^{92+} survive or, possibly, retardation effects (higher powers in kr) play a role, owing to tighter binding. In this particular case, with $n = 5$ the corresponding photoelectron energy is smaller but comparable to the electron binding energy of the $n = 5$ levels in bare uranium. At a considerably higher energy of 68 MeV/u (corresponding to a relative kinetic electron energy of 37.3 keV), the differences between the two approaches become still larger, see Fig. 3.6. At this larger relative velocity, the interaction of the current produced by the projectile motion and the electron spin can certainly not be neglected.

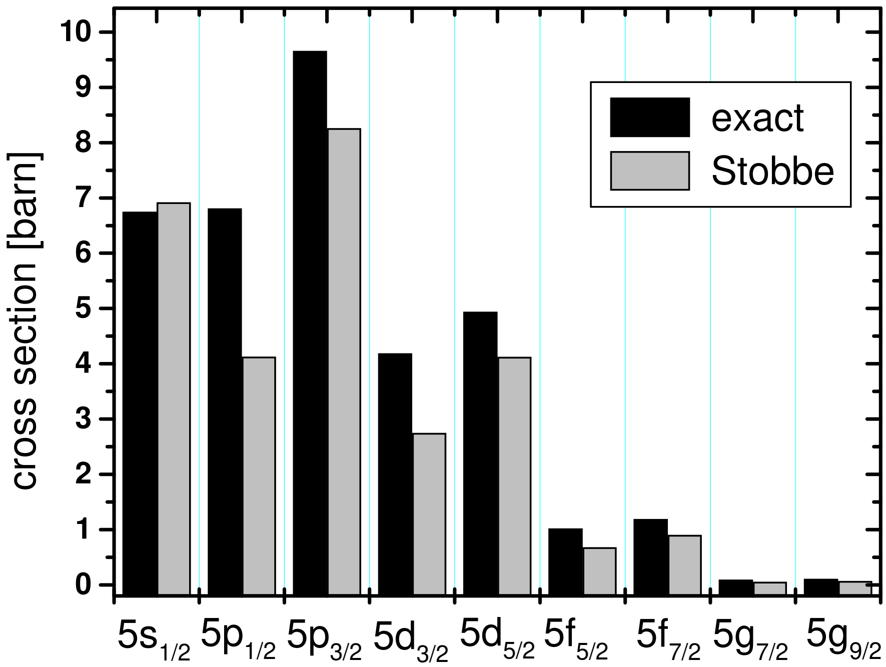

Figure 3.6: Same as Fig. 3.5., but for the energy of 68 MeV/u (corresponding to a relative kinetic electron energy of 37.3 keV).

The differences between the two approaches as a function of energy are shown in Fig. 3.7 for the K-shell of bare uranium. The Stobbe theory is seen to overestimate the K-RR cross section for low energies, and decreases more rapidly with increasing projectile energy than the relativistic prediction as is to be expected. In Fig. 3.8, the total cross sections calculated with both approaches are depicted as a function of the projectile energy. The agreement can be seen up to energies as high as 200 MeV/u.

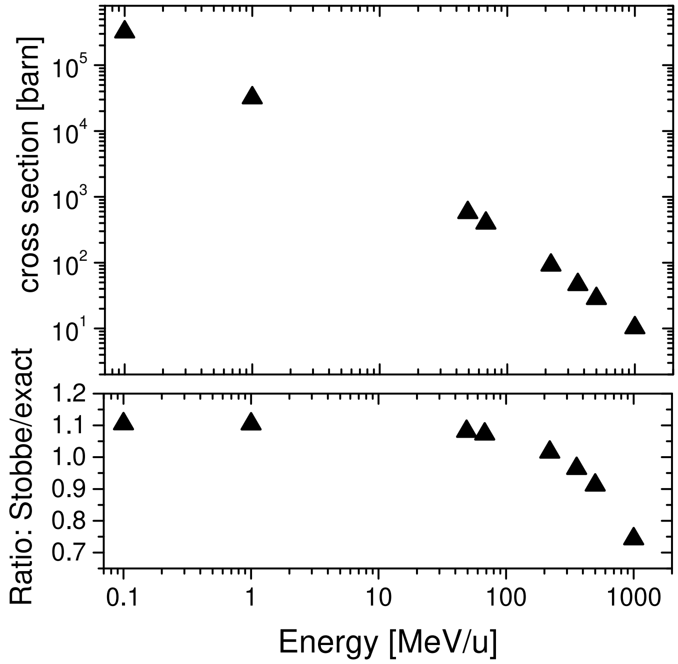

Figure 3.7: RR into the K-shell of bare uranium. In the upper figure, only the exact relativistic cross sections are presented.

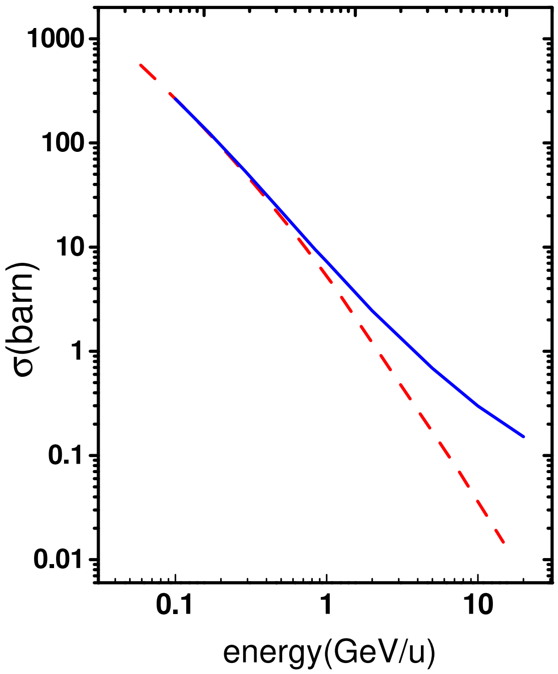

Figure 3.8: The dipole approximation total cross sections (dashed line) compared to the complete relativistic calculations (solid line, as a function of the projectile energy.

3.2 Radiative recombination rate coefficients

The processes in which ions capture cooling electrons are extremely important for accelerator physics and also for atomic physics. Electron cooling is based on the Coulomb interaction between a cold electron beam, in which cold electrons are supplied continuously, and a hot ion beam. The ions and the electrons move parallel on a straight section of a storage ring. The Coulomb interaction leads to energy and momentum transfer between the two beams, so that finally a thermodinamical equilibrium is reached, the temperature of the ion beam being drastically reduced. The value of the capture rate in comparison with the cooling rate has to be small enough in order to cool the ion beam with a negligible loss of intensity. When the electron beam has some velocity distribution $f(\mathbf{v})$, instead of the radiative recombination cross section defined for a fixed electron velocity, it is more convenient to introduce an integrated quantity, namely the rate coefficient α_{nl}, defined by

$$\alpha_{nl} = \langle \mathbf{v}\sigma_{nl}(\mathbf{v})\rangle = \int \mathbf{v}\sigma_{nl}(\mathbf{v}) f(\mathbf{v}) d^3\mathbf{v}. \tag{3.36}$$

For the velocity distribution of the electrons a Maxwellian (3.37) or a normalized flattened distribution (3.38) will be considered. The Maxwell distribution is given by

$$f_M(\mathbf{v}) = \left(\frac{m_e}{2\pi kT_e}\right)^{3/2} e^{-\frac{m_e \mathbf{v}^2}{2kT_e}} \tag{3.37}$$

where m_e is the electron mass, k denotes the Boltzmann constant and T_e is the temperature of the electron beam. Under realistic experimental conditions, the electron beam in the cooler is characterized by effective longitudinal $kT_{||}$ and transverse $kT_{\perp}$ beam temperatures and has, in the ion frame, the following relative velocity distribution

$$f_f(\mathbf{v}) = \left(\frac{m}{2\pi}\right)^{3/2} \frac{1}{kT_{\perp}(kT_{||})^{1/2}} e^{-\left(-\frac{m_e v_{\perp}^2}{2kT_{\perp}} - \frac{m_e v_{||}^2}{2kT_{||}}\right)} \tag{3.38}$$

In the electron cooler, the effective electron-beam temperatures in the ion frame ($kT_{||}$ and $kT_{\perp}$ result from convolution of the electron- and ion-beam velocity distributions, characterized by $(kT_{e||}, kT_{e\perp})$ and $(kT_{i||}, kT_{i\perp})$ beam temperatures, respectively. Consequently, one gets the following expression for the effective electron-beam temperature in the ion frame

$$kT_{||} = kT_{e||} + \frac{m_e}{M} kT_{i||}, \tag{3.39}$$

$$kT_{\perp} = kT_{e\perp} + \frac{m_e}{M} kT_{i\perp}, \tag{3.40}$$

Bell and Bell, [77], calculated approximate analytical formulas for α_r for both Maxwell distribution and a flattened distribution, valid as long as the relative kinetic energy between electrons and ions is comparable to kT_e. If kT_e is measured in eV, then

$$\alpha_r^M = \frac{1.92Z^2}{\sqrt{kT_e}} \left\{ \ln \frac{5.66Z}{\sqrt{kT_e}} + 0.196 \left(\frac{kT_e}{Z^2} \right)^{1/3} \right\} 10^{-13} \left[\frac{cm^3}{s} \right] \tag{3.41}$$

and

$$\alpha_r^f = \frac{3.02Z^2}{\sqrt{kT_e}} \left\{ \ln \frac{11.32Z}{\sqrt{kT_e}} + 0.14 \left(\frac{kT_e}{Z^2} \right)^{1/3} \right\} 10^{-13} \left[\frac{cm^3}{s} \right] \tag{3.42}$$

Kim and Pratt gave an analytical solution for the rate coefficient, using the simple formula based on Kramer's semiclassical prediction for the cross section with $Z_{eff} = \frac{1}{2}(Z + Z_i)$

$$\sigma_n = \frac{8\pi}{3\sqrt{3}} \frac{\alpha^5 Z_{eff}^4}{n^3 K (K + Z_{eff}^2 \alpha^2 / 2n^2)} \tag{3.43}$$

After summing over the n-states and integrating, they obtained the total rate coefficient for a Maxwell distribution:

$$\alpha = 2a^2 A' kT \left[e^{+sa^2/kT} E_1 \left[\frac{sa^2}{kT} \right] + C + ln \left[\frac{sa^2}{kT} \right] \right] \tag{3.44}$$

where E_1 is the first exponential integral

$$E_1(Z) = \int_Z^\infty (e^{-t}/t) dt \tag{3.45}$$

Liesen and Beyer did a calculation in a closed form for both Maxwell and a completely flattened distribution (3.46), using the formula of Bethe and Salpeter (3.24) for the total cross section σ_n

$$f_f(\mathbf{v}) = \left(\frac{\mathrm{m}}{2\pi \mathrm{kT_e}} \right) \mathrm{e}^{-\mathrm{E_e/kT_e}} \delta(\mathrm{v_z}) \tag{3.46}$$

$$\alpha_{r,n}^M = 4.2 \times 10^{-22} \sqrt{\frac{2}{\pi m k T_e}} \frac{E_0}{n} \left\{ 1 - \frac{n^2 k T_e}{e_0} + 2 \left(\frac{n^2 k T_e}{E_0} \right)^2 \pm \right\} \left[\frac{cm^3}{s} \right] \tag{3.47}$$

$$\alpha_{r,n}^f = 2.1 \times 10^{-22} \sqrt{\frac{2\pi}{m k T_e}} \frac{E_0}{n} \left\{ 1 - \frac{1}{2} \frac{n^2 k T_e}{e_0} + \frac{3}{4} \left(\frac{n^2 k T_e}{E_0} \right)^2 \pm \right\} \left[\frac{cm^3}{s} \right] \tag{3.48}$$

The calculations can be done analytically for the normal flattened distribution (3.37) up to where it can be, as above, written as series of powers.

Considering for the cross section the Bethe and Salpeter formula, the rate coefficient can be written as

$$\alpha_{r,n}^{f} = \int_0^{\infty} \int_0^{2\pi} \int_{-\pi/2}^{\pi/2} v\sigma(v) \left(\frac{m}{2\pi k}\right)^{\frac{3}{2}} \frac{1}{T_{\perp}\sqrt{T_{\|}}} \times e^{-\frac{m}{2K}\left(\frac{cos^2\phi}{T_{\perp}}+\frac{sin^2\phi}{T_{\|}}\right)} v^2 cos\phi \; dv \; d\psi \; d\phi \tag{3.49}$$

From Eqs. (3.24)and (3.49), after a change of variable, one can write

$$\alpha_{r,n}^{f} = A \int_0^{\infty} \int_0^{1} \frac{v \exp\left(-v^2(a^2y^2+b^2)\right)}{v^2+c^2} dx \; dy = AI \tag{3.50}$$

where

$$A = 2.1\sqrt{\frac{2}{\pi}} \frac{E_0^2}{n^3a^4} \times 10^{-22}, \; a^2 = \frac{m}{2}\frac{kT_{\perp}-kT_{\|}}{kT_{\perp}kT_{\|}}, \; b^2 = \frac{m}{2kT_{\perp}}, \; c^2 = \frac{2}{m}\frac{E_0}{n^2}. \tag{3.51}$$

We shall use the following simple formula:

$$\alpha_{r,n}^{f} = A \; I \; \int_0^{v} \exp\left(-t^2\right) dt = v \int_0^{1} \exp\left(-v^2u^2\right) du \; , \tag{3.52}$$

obtained by the substitution $t = vu$.
We can write

$$I = \int_0^{\infty} \left(\frac{v \exp\left(-b^2v^2\right)}{v^2+c^2} \int_0^{1} \exp\left(-(av)^2y^2\right) dy \right) dv.$$

By using formula (3.52) we get:

$$I = \frac{1}{a} \int_0^{\infty} \int_0^{av} \frac{\exp\left(-b^2v^2\right)\exp\left(-t^2\right)}{v^2+c^2} dtdv \; .$$

By the substitution $bv = u$ we obtain:

$$I = \frac{1}{\alpha} \int_0^{\infty} \int_0^{\alpha u} \frac{\exp\left(-(u^2+t^2)\right)}{u^2+\beta^2} dtdu \; , \tag{3.53}$$

where $\alpha = a/b$ and $\beta = bc$.
The domain of the last double integral is the angle between the semi-lines $u = 0$, $u > 0$ and $t = \alpha u$, $u > 0$. Passing to the polar coordinates $u = \rho\cos\theta$, $t = \rho\sin\theta$, we get the jacobian ρ and the domain $0 < \rho < \infty$, $0 < \theta < \arctan\alpha$. We have:

$$I = \frac{1}{\alpha} \int_0^{\infty} \frac{\exp\left(-\rho^2\right)}{\rho} \int_0^{\arctan\theta} \frac{1}{\cos^2\theta + (\beta/\rho)^2} d\theta d\rho \; . \tag{3.54}$$

Using the several substitutions, $\tan\theta = t$, $\rho^2 = t$, and $s = \sqrt{t+\beta^2}$, we get finally:

$$I = \frac{\exp\left(b^2c^2\right)}{ac}\int_{bc}^{\infty}\exp\left(-s^2+b^2c^2\right)\arctan\frac{ac}{s}ds\ . \tag{3.55}$$

The double integral (3.49) is reduced to a simple integral:

$$\alpha_{r,n}^{f} = 8.4\times10^{-22}\frac{E_0^2}{Zn^2}\left(\frac{mkT_\perp kT_\|}{2Z(kT_\perp - kT_\|)}\right)^{\frac{1}{2}}$$
$$\times\int_{\frac{Z}{n\sqrt{kT_\perp}}}^{\infty} e^{-s^2+\frac{Z^2}{n^2kT_\perp}}\arctan\frac{z}{n}\left(\frac{kT_\perp - kT_\|}{kT_\perp kT_\|}\right)^{\frac{1}{2}}ds$$

Using the corrections for the cross sections in the case of lower lying states (Gaunt factors), one can obtain a closed form for the RR rate coefficient for a flattened distribution as a function of the principal quantum number n and the two temperatures of the electron beam.

A different approach has been the development of a computer code that calculates the n,l rate coefficients for both distributions, using (3.40) and (3.41), and the dipole approximation result (see 3.1.) for the radiative recombination cross section. The integrals are evaluated using the Gauss method.

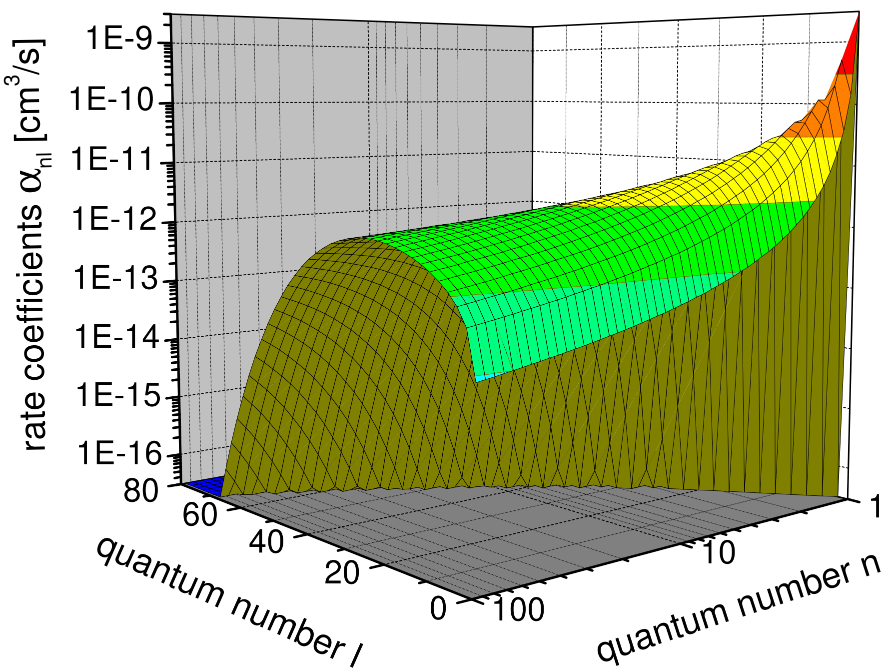

Figure 3.9: State selective total rate coefficients calculated for radiative recombination into bare uranium ions and for a Maxwell distribution with $T_e = 0.2$eV.

The code gives the rate coefficient as a function of the nuclear charge, the principal and angular momentum quantum numbers, and the temperature of the electron

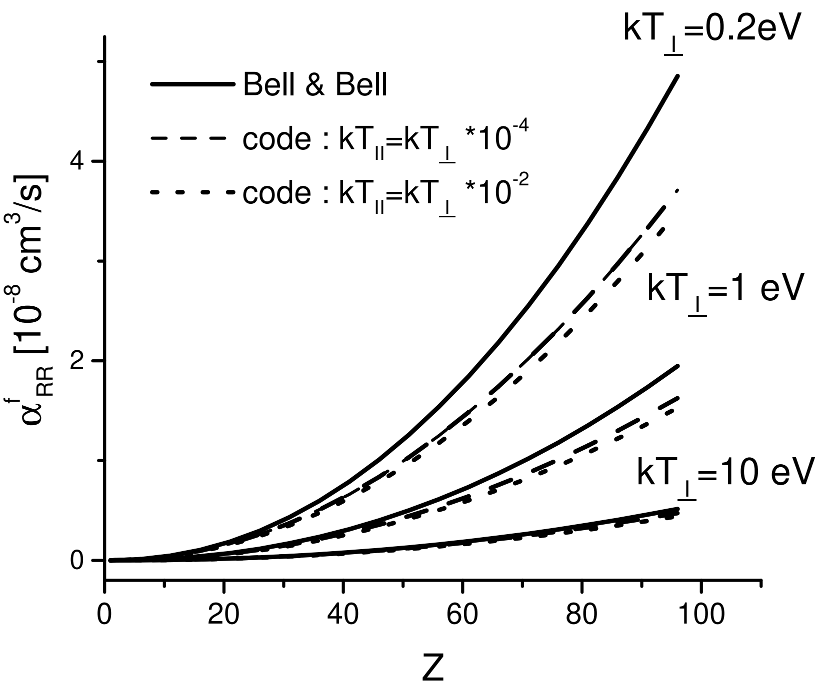

Figure 3.10: Rate coefficients for radiative recombination obtained by exact integration (code) and using Bell and Bell formula (3.42) for a flattened distribution as a function of the projectile nuclear charge Z.

beam, in the case of a Maxwell distribution, or the two temperatures, longitudinal and transverse, for a flattened distribution. Fig. 3.9 presents the results of the code for a nuclear charge $Z = 92$ for the projectile ion and a transverse electron-beam temperature in the ion frame of 0.2 eV, which is typical for the experiments in the storage rings.

For a flattened distribution, Fig. 3.10 shows a very good agreement with Bell and Bell formula for low nuclear charges but discrepancies for high nuclear charges. The rate coefficient has a maximum as function of the longitudinal temperature - here the agreement with (3.41) is reached, for small Z, as is shown in Fig. 3.11. Here we used the ratio between the integrated value and Bell and Bell's result, the latter being constant as function of this temperature $T_{\|}$. The comparison in the case of a Maxwell distribution shows the same agreement for low nuclear charges as above (Fig. 3.12).

The rate coefficients are calculated by McLaughlin and Hahn ([75]) as a function of a parameter $\Theta = k_B T/Z_{eff}^2$ called scaled temperature. The comparison (Fig. 3.13) shows a good agreement for a high scaled temperature, i.e. low nuclear charge or high electron beam temperature (high spread of transverse velocity). The comparison is made for the case of bare ions, but using the formulas for effective charge leads to the same result.

In the most precise experiments performed up to now, the recombination rates at the electron cooler were found significantly bigger than the theoretical values for complex heavy ions, but also for ions with simple structure and bare ions. However,

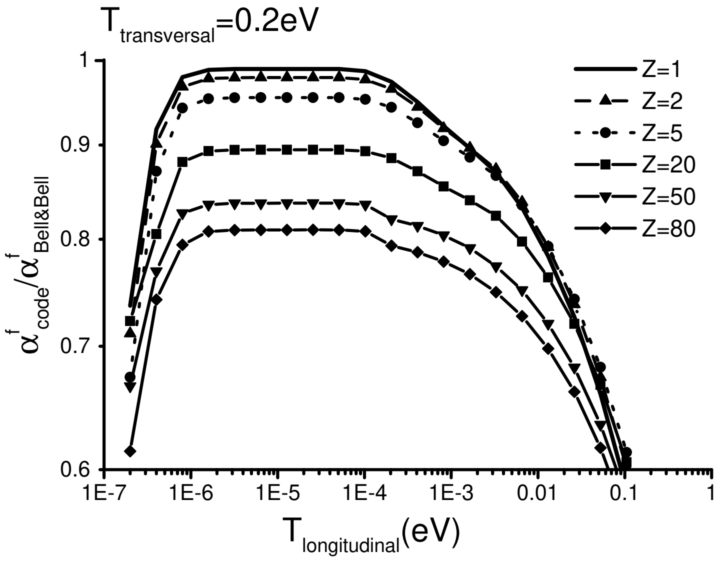

Figure 3.11: For a fixed transverse temperature $T_\perp$, the radiative recombination rate coefficient for a flattened velocity distribution, as a function of the longitudinal temperature $T_{||}$ for several nuclear charges of the projectile.

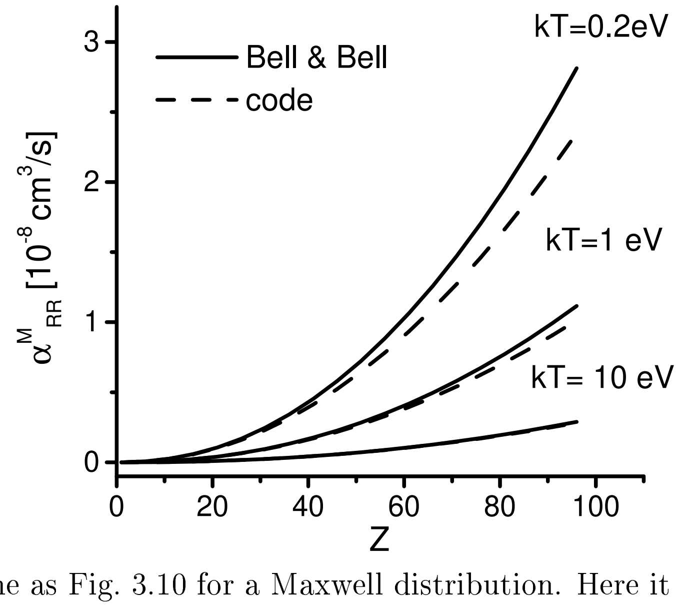

Figure 3.12: Same as Fig. 3.10 for a Maxwell distribution. Here it can be seen that the results of the code (this work) tend asymptotically to the values given by Bell and Bell's formula (3.41).

this increase of the rate by factors of up to ≈ 5 has not been theoretically explained up to now. The radiative recombination theory is well understood and not responsible for these discrepancies. As it has been discussed [78] the rate enhancement may be related with the low electron velocity spread in longitudinal direction and to the presence of a longitudinal magnetic guiding field for the electron beam. Recent experiments indicated that for certain complex highly charged ions the strong enhancement of the recombination rate is caused by low-energy dielectronic resonances

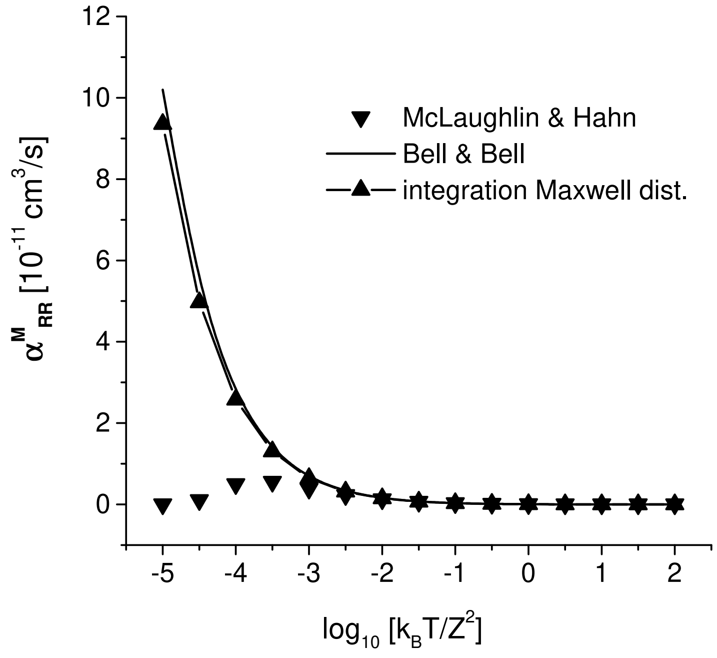

Figure 3.13: Comparison with the work of McLaughlin and Hahn for a Maxwell distribution. The radiative recombination rate coefficients are represented as function of the scaled temperature. The effective charge Z_{eff} defined in [75] is in this case the nuclear charge Z of a bare ion (see text).

---

[79]. Investigations regarding the dependence of the enhancement on experimental parameters like the ion charge, the electron density and external fields are expected.

3.3 Results and Conclusion

The exact calculations for the radiative recombination cross sections in the case of nonrelativistic energies within the dipole approximation were done using the Stobbe approach without any other approximation.

A computer code has been developed, that calculates the state selective n,l cross sections up to very high n. This results are needed in the case of recombination in the electron cooler where, due to the small relative velocity between ions and electrons the contribution from high Rydberg states might have a significant contribution to the total cross section. The capture in these high levels is important also for the study of the x-ray spectra resulted from the radiative cascade of the electron to the ground state (see chapter 4).

General features of the n,l dependent cross section can be deduced from the graphic in Fig. 3.1. Here it can be seen that the main contribution to the cross section is given by the K-shell, as is to be expected. The dependence of the principal quantum number n shows the scaling behaviour of the cross section : for low n-states, the cross section has a steep decreasing behaviour with increasing n, like the approximate scaling law $1/n$ and for high n, a slower decrease, consistent with $1/n^3$. Within one shell (i.e. fixed n) the cross section presents a maximum for a medium $l \approx n/3$.

The comparison with other nonrelativistic theoretical approaches shows further that they lead to the same results within very close limits. A bench-mark comparison with complete relativistic results for the time-reversed process cross sections for photoionization in the K, L and M shells of hydrogen shows a perfect agreement, within the first three digits [80].

The dipole approximation proves to be applicable in the low-energy regime, even for high nuclear charges as $Z = 92$. However, in such cases there are remaining differences from a relativistic formulation. These discrepancies appear mainly in the case of the subshell, j-sensitive cross sections for higher angular momenta quantum number l; for s and p states the agreement is better. The statistical weights considered for the calculations of the nlj cross sections are responsible for this discrepancies, the total cross sections showing a very good agreement in comparison to the complete relativistic calculations. Here the relativistic effects, as in the case of U^{92+} (see Fig. 3.8) have a significant contribution, or possibly retardation effects may play a bigger role.

In the case of radiative recombination rate coefficients, the main features in the nl dependence of the results are determined by the cross section dependence of n and l, as seen in Fig. 3.9. The influence of the longitudinal temperature shows that the smaller is $T_{\|}$ with respect to the transverse temperature, the result of the code is better approximated by the widely used Bell & Bell formula for a completely flattened distribution, as is expected. For a low nuclear charge and/or a high transverse temperature, the coefficient rates calculated for a Maxwell distribution of the electron velocity compared with other theoretical approaches lead to the same result within close limits.

In conclusion, the radiative recombination results based on Stobbe′s theory are accurate and there is no need for further approximations in the calculations. The cross sections and the rate coefficients can be calculated for any individual nl state. For high-Z ions the total cross sections and the rate coefficients are in a very good agreement with the complete relativistic calculations, test that was not performed up to now. However, as a result of a detailed comparison, the discrepancies that may appear from an exact theoretical treatment indicate for particular cases the need for more exhaustive validity tests.

Chapter 4

Radiative Electron Capture - Recombination at high energies

In the high-energy domain of high-Z ions collisions, where the relativistic effects have an important contribution in the interaction processes, several differential aspects of the photoionization can be studied for the case of few-electron heavy ions. The comparison between experimental data for the time reversed process, REC, and theoretical results allows a new and detailed understanding of the fundamental electron-photon interaction. In particular, the angular distribution measurements for REC are proved to be an unequaled and clear experimental method to study the magnetic contributions to the photoionization effect, in investigations that have not been done before [81]. In the following there will be no differentiation between the REC and the RR process as they are equivalent, within the impulse approximation, for light targets and relativistic highly charged projectiles.

4.1 Total REC Cross Sections

For the measurements of total REC cross sections, several experiments were performed utilizing the internal gas jet of the ESR for measurements with gaseous targets [44], [82].

4.1.1 Description of the experiment

In the case of the experiments performed at the ESR, the ions were stripped in front of the storage ring to high charge states in a 100 mg/cm^2-thick Cu foil. The outgoing bare or H-like ion species were magnetically separated and finally injected into the ESR. Here the ions were cooled and accumulated up to a typical number of stored projectiles of about 10^7. After the stacking procedure, the gas jet was switched on. Molecular nitrogen with a thickness of 4×10^{11} particles/cm^2 was used as reaction target for all applied projectile species and collision energies. Additionally, for the uranium experiment, an Ar jet with a target thickness of 5×10^{11} particles/cm^2 could be used for reaction studies. The reaction area of the gas target was surrounded by three Ge(i) x-ray detectors mounted at observation angles of 48°, 90°, and 132° with respect to the beam axis. In contrast to the backward direction (132°), where a conventional x-ray detector with an active area of 500 mm^2 and a thickness of

10 mm was installed, the large Doppler broadening at 90° and 48° observation angles required the application of specially designed granular x-ray detectors. In particular, the x-ray detector mounted at the 48° position (crystal thickness 12 mm) was subdivided into seven independent segments (parallel stripes with active areas of 3.5×24 mm^2 each,furnished with separate readouts). This detector delivered seven independent spectra with relatively small individual Doppler broadenings. The Doppler shift was corrected separately for each segment. The segmented 5-mm thick Ge(i) detector at 90° observation angle covered in total a solid angle of $\Delta\Omega/4\pi = 3 \times 10^{-4}$. The detector was divided into five independent segments, four quadrants (forward, backward, top, and bottom) with the same size of 65 mm^2 each, and one central part with an active area of 36 mm^2. The detectors at the forward and backward angles were separated by 100 mm thick Be windows from the high vacuum system of the ESR, whereas for 90° a 50 mm thick stainless steel window was used. Downstream from the target area, behind the next dipole magnet, a position sensitive multiwire detector (MWPC) detected ions having captured one electron in collisions with the target atoms (molecules). For the absolute normalization of the data, the current of the circulating ion beam was measured by a calibrated current transformer installed in the ring, whereas the revolution frequency of the particles was determined via the analysis of the Schottky noise spectrum [44].

4.1.2 Comparison with theoretical calculations

In Fig.4.1, the available data for total electron capture from light target atoms into bare, high-Z projectiles is presented. The data were collected at the Lawrence Berkeley Laboratory's BEVALAC, and at the FRS and ESR facilities. The corresponding capture cross sections plotted in the figure are normalized to the number of target electrons. The corresponding adiabaticity parameter η, defined in chapter 2, (1.4) is shown on the upper scale.

In this figure, the presentation shows mainly the high-velocity regime, where the electron capture by the projectile from light targets is dominated by far by radiative capture. The measured data are compared with theoretical predictions for REC done for Z=80, i.e. Stobbe's nonrelativistic dipole approximation and the complete relativistic calculations.

Even though the experimental differential and state selective cross section may differ significantly from the values predicted by the nonrelativistic dipole approximation, here it can be seen that this is not the case for total cross sections, as it was also already noted by Stöhlker and co-workers [83], and confirmed by the relativistic calculations of Ichihara, Shirai and Eichler [42].

A general excellent agreement between the experimental data, the nonrelativistic approach and the exact calculations is found in Fig.4.1. However, at the higher η regime, the results of the fully relativistic calculations deviate from the predictions of the nonrelativistic approach. The latter underestimates the measured cross sections at these highly energetic collisions, as is to be expected.

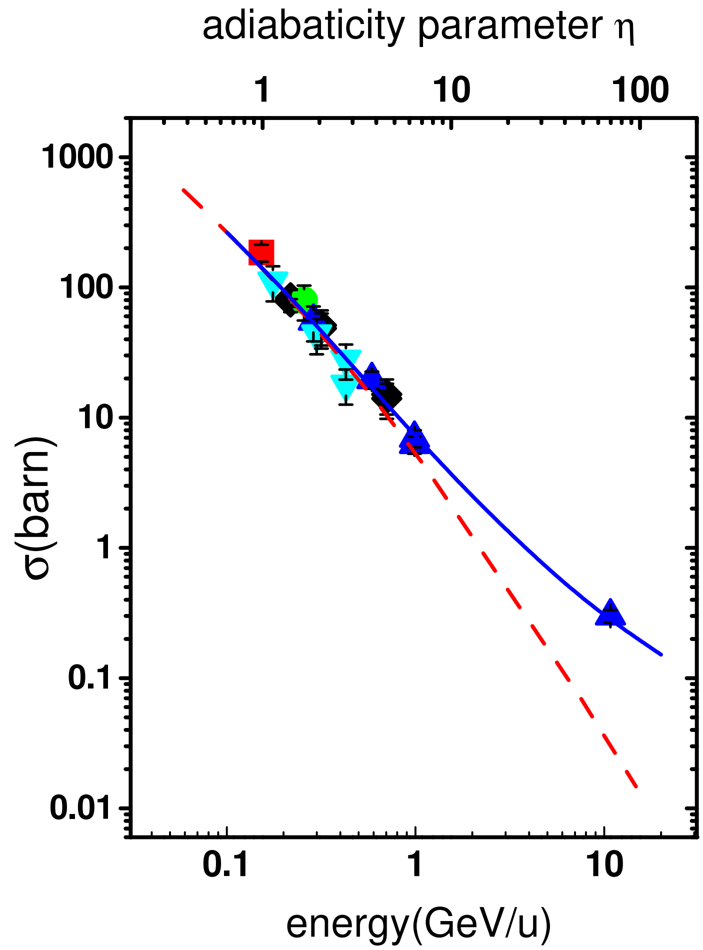

Figure 4.1: The dipole approximation (dashed line) in comparison with the complete relativistic calculations (solid line) and the experimental data covering the Z range between 54 and 92 (symbols) collected in different experiments at BEVALAC, Berkeley, FRS and ESR. The measured cross section were normalized to the number of target electrons.

4.2 Angular distributions

In order to describe the important relativistic effects that appear in the case of collisions with high-Z systems, an exact theoretical treatment is required. For the nonrelativistic domain of low-Z ions, differences from the symmetric dipole distribution have been observed. Moreover, at high-Z, the full retarded multipole expansion of the photon field (the expansion of the photon plane wave $e^{i\mathbf{k}\mathbf{r}}$ which is considered equal to 1 in the dipole approximation) must be considered and the strength of the relativistic effects may lead to significant corrections. However, they are difficult to be observed in direct photoionization experiments, since the retardation leads to a strong peaking of the photoelectron angular distribution towards forward angles (as it will be argued in the following). Photoionization usually deals with many electron systems, which are complicated to describe theoretically. REC, on the contrary can be studied on simple and clean atomic systems - capture into bare ions - giving experimental access to the study of photoionization for high-Z H-like ions, i.e. for a point-Coulombic system, where the process can be studied without any electron screening problems.

4.2.1 Nonrelativistic and relativistic theory

The differential cross section for the atomic photoeffect can be written as

$$\mathrm{d}\sigma/\mathrm{d}\Omega = (2\pi)^{-2}\, p\, E\, |M_{fi}|^2, \tag{4.1}$$

subject to energy conservation. Here p and E are the momentum and the energy of the ejected photoelectron. The photoeffect matrix element is

$$M_{fi} = \left(\frac{2\pi\alpha}{k}\right)^{1/2} \int \psi_f^\dagger\, \vec{\alpha}\cdot\vec{\epsilon}\, \exp(i\vec{k}\,\vec{r})\, \psi_i\, d^3r \tag{4.2}$$

where $\vec{k}$ and $\vec{\epsilon}$ are the momentum and polarization of the incident photon, ψ_i is the initial bound and ψ_f the final continuum electron wave functions. This reduces in the nonrelativistic dipole approximation to the simple form

$$M_{fi} = \left(\frac{2\pi\alpha}{k}\right)^{1/2} \int \psi_f^\dagger\, \vec{p}\cdot\vec{\epsilon}\psi_i\, d^3r \tag{4.3}$$

i.e. the electron-photon interaction $\exp(i\vec{k}\vec{r})$ (the so-called retardation) is neglected. From (4.2), $|M_{fi}|^2$ has to be quadratic in $\vec{\epsilon}$. If one sums over the magnetic substates of the shell from which the electron is ejected, the only other vector in $\sum |M_{fi}|^2$ is $\vec{p}$, since the wave function does not depend on the electron-spin direction. The only dependence of the scalar quantity $\sum |M_{fi}|^2$ on the momentum direction is then of the form $A + B|\vec{p}\cdot\vec{\epsilon}|^2$, where A and B depend on energy and shell but not direction. This shows that the shape of the angular distribution, even for polarized photons, only depends on one parameter. Averaging over photon polarization one obtains

$$|\hat{p}\cdot\hat{\epsilon}|^2 = \frac{1}{2}(\hat{k}\times\hat{p})^2 \tag{4.4}$$

so the unpolarized cross section is

$$\frac{\mathrm{d}\sigma}{\mathrm{d}\Omega} = \frac{1}{4\pi}\sigma_{nl}\,[1 - \frac{1}{2}\beta_{nl}P_2(cos\theta)] \tag{4.5}$$

with the asymmetry parameter $\beta_{nl} = 2B/(3A+B)$ and θ the angle between $\hat{k}$ and $\hat{p}$.

One can obtain an explicit expression for β_{nl}, expressing the bound and continuum wave functions in (4.3), as solutions of the Schrödinger equation, and using the recurrence relations and the orthogonality properties for the spherical harmonics [84].

$$\beta_{nl} = \frac{l(l-1)R_{l-1}^2 + (l+1)(l+2)R_{l+1}^2 - 6l(l+1)R_{l-1}R_{l+1}\cos(\delta_{l+1}-\delta_{l-1})}{(2l+1)[lR_{l-1}^2 + (l+1)R_{l+1}^2]} \tag{4.6}$$

where the radial matrix elements are

$$R_{l'}(p) \equiv \int_0^\infty R_{pl'}(r) r^3 R_{nl}(r) dr \tag{4.7}$$

Further, in the case of an s-wave bound state the distribution is simply proportional to $\sin^2(\theta) \equiv \frac{2}{3}[1 - P_2(\cos\theta)]$, or β_{n0}=2, for M_{fi} must be linear in $\vec{\epsilon}$ and now the only vector in M_{fi} is $\vec{p}$ (for a nonrelativistic s wave there is no vector associated with the magnetic substate), so M_{fi} is of the form $|C|^2|\vec{p} \cdot \vec{\epsilon}|^2$, giving $\sin^2\theta$ upon averaging over photon polarization.

The simple formula of Bethe and Salpeter for the angular distribution of the cross section for capture in the s-states of the projectile is

$$\frac{\mathrm{d}\sigma}{\mathrm{d}\Omega} = \frac{3}{8\pi}\sigma_{RR}\sin^2(\theta_p) \tag{4.8}$$

with $\theta_p = \pi - \phi_p$, where θ_p is the angle between the directions of the incoming electron and the emitted photon, respectively. For the point Coulomb $2p$ case the exact nonrelativistic dipole result of Schur is [85]:

$$\langle\frac{d\sigma}{d\Omega}\rangle \propto 1 + \frac{4\epsilon_L}{k}\sin^2\theta \tag{4.9}$$

or

$$\beta_{21} = \frac{16E_L}{3E_{kin} + 8E_L} \tag{4.10}$$

which varies from $\beta_{21} = \frac{16}{11}$ at threshold ($E_{kin} = E_L$), where E_L is the binding energy of the L-shell, to 0 (isotropic distribution) at high energies. The latter is in accord with the result of Bethe and Salpeter that for p waves in the Born approximation (i.e. high nonrelativistic energy) $\beta_{nl} = 0$ for any potential.

A treatment of the photoeffect based on the Born approximation and Dirac wave functions, gives for relativistic ions a deviation from the symmetric $\sin^2$ distribution of the angular distribution (4.11), [3], [12]:

$$I_{lab}(\theta_{lab}) \approx \sin^2(\theta_{lab})\left[1 + \frac{(\gamma-1)(\gamma-2)}{2\gamma(1-\beta\cos\theta_{lab})}\right] \tag{4.11}$$

A relativistic theory for RR has been developed in recent years. The exact relativistic differential photoelectric cross sections were calculated, from which the corresponding differential cross sections for the RR process were derived by the principle of detailed balance. The calculations use exact wave functions for bound and continuum states [42], [43].

For a given momentum distribution in the target, the rigorous treatment of the REC angular distribution proceeds by deriving the differential RR cross section from the calculated photoionization cross section, convoluting this cross section with the momentum distribution of the electrons within the target and finally Lorentz transforming the result from the projectile to the laboratory frame.

For a given photon energy, the differential cross section for the photoionization, $\sigma_{ph}(\omega', \theta')$ is given by

$$\frac{\mathrm{d}\sigma_{ph}}{\mathrm{d}\Omega} = \frac{\alpha^3 m_e c^2}{4\hbar\omega}\frac{a_0^2}{2(2j_b+1)}\sum_{\mu_b}\sum_{m_s}\sum_{\lambda}|M_{\mathbf{p},b}(m_s,\lambda,\mu_b)|^2, \tag{4.12}$$

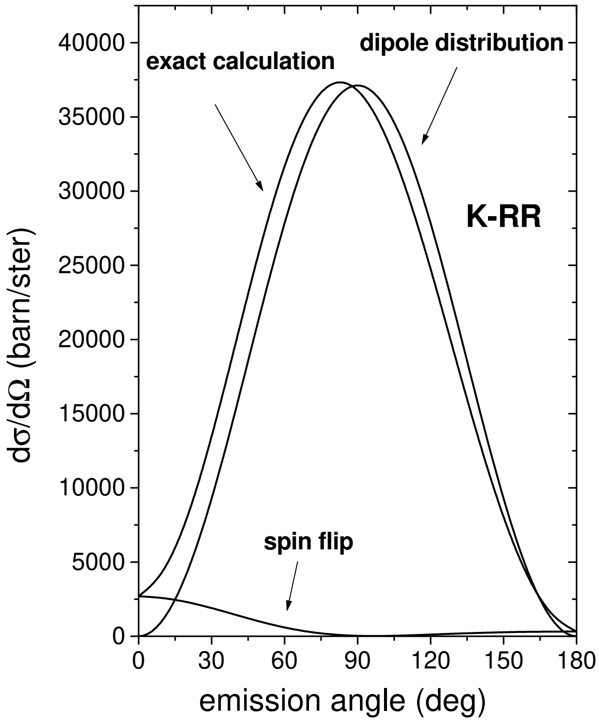

Figure 4.2: Angular distribution for RR into the K-shell of bare uranium, at 0.1 MeV/u. The dipole distribution ($\sin^2\theta$) is contrasted with the exact relativistic calculations. The contribution form the spin-flip transitions is shown separately.

where the average over the $2j_b + 1$ angular momentum projections μ_b in the bound state b and over the circular polarizations $\lambda = \pm 1$ of the incoming photon is taken and summation over the spin projections $m_s = \pm\frac{1}{2}$ of the emitted electron is performed. The transition matrix element is

$$M_{\mathbf{p},b}(m_s, \lambda, \mu_b) = \int \psi_{\mathrm{p},m_s}(\mathrm{r})\alpha \cdot \hat{\mathrm{u}}_\lambda e^{i\mathrm{k}\cdot\mathrm{r}} \psi_{j_b,\mu_b} d^3 \tag{4.13}$$

where α is the Dirac alpha matrix and $\hat{\mathrm{u}}_\lambda$ is the unit vector of photon polarization. By the principle of detailed balance, the cross section $\sigma_{RR}(E', \theta')$ is obtained

$$\frac{\mathrm{d}\sigma_{RR}(E', \theta')}{\mathrm{d}E'\mathrm{d}\Omega'_{ph}} = (2j_b + 1) \left(\frac{\hbar\omega'}{m_e c^2}\right)^2 \frac{1}{\beta^2\gamma^2} \frac{\mathrm{d}\sigma_{ph}(E', \theta')}{\mathrm{d}E'\mathrm{d}\Omega'_{el}} \tag{4.14}$$

Here the factor $(2j_b + 1)$ converts the averaging of (4.12) into a summation, while $\beta = v/c$ and $\gamma = (1 - \beta^2)^{-1/2}$ is the Lorentz factor. Furthermore, the REC cross section is obtained by adopting the impulse approximation and convoluting σ_{RR} with the momentum distribution $\rho(\mathbf{q})$ of the electrons in the target atom:

$$\frac{\mathrm{d}\sigma_{REC}(\omega', \theta')}{\mathrm{d}\omega'\mathrm{d}\Omega'} = \int \mathrm{d}^3 q \frac{\mathrm{d}\sigma_{RR}(\mathrm{q'})}{\mathrm{d}\Omega'} \rho(\mathrm{q'})\delta(\hbar\omega' + E'_f - E'_i) \tag{4.15}$$

where E'_i and E'_f are the total energies (including the rest mass) of the initial and final atomic states, and δ function ensures the energy conservation. If the transverse momentum distribution of the electrons in the initial state i is negligible, one may express the REC cross section with the aid of the Compton profile.The momentum density ρ(q') is obtained by Fourier transforming appropriate Roothaan-Hartree-Fock wave functions. Finally, one has to transform all quantities into the laboratory system [43].

For radiative electron capture into $1s$ states, as is mentioned above, the nonrelativistic dipole approximation yields the classical dipole distribution $W(\theta) = \sin^2\theta$, where θ is the angle between the electron momentum $\mathbf{p}$ and the photon momentum $\mathbf{k}$. If the retardation is considered, the photoelectron angular distribution for K-shell photoionization, as function of the observing angle θ_{PI}, which is the angle between the momenta of the incoming photon and the outgoing electron, can be written as:

$$\frac{d\sigma_{PI}}{d\Omega} \approx \frac{\sin^2(\theta_{PI})}{(1+\beta\cos(\theta_{PI}))^4} \tag{4.16}$$

The function on the right side of (4.16) shows a maximum for forward angles, i.e. the angular distribution of the emitted electrons in the relativistic case is strongly shifted towards the direction of the incoming photon momentum. This angle for which the angular distribution takes the maximum value depends on the velocity of the emitted electron. The bigger the energy of the electron, the angular distribution is more strongly shifted to forward angles. The photoionization process is the time-reversed REC in the projectile frame, where the incoming particle is the free electron moving towards the projectile with momentum $\mathbf{p}'$, and the photon is emitted via the capture into the K-shell. Due to this equivalence (time reversal), the angular distribution of the emitted REC photons with respect to the direction of the incoming electron is the same with the photoelectron angular distribution given in (4.16). In the projectile frame, this direction is inversed, thus the REC angular distribution will be strongly shifted to backward angles. With other words, the angle θ' between the photon and electron momenta in the projectile frame is $\theta' = \pi - \theta_{PI}$, and the angular distribution:

$$\frac{d\sigma_{REC}}{d\Omega'} \approx \frac{\sin^2(\theta')}{(1-\beta\cos(\theta'))^4} \tag{4.17}$$

In order to obtain the angular distribution in the laboratory frame, the Lorentz transformation of the angle θ' and of the solid angle Ω' are needed:

$$\begin{aligned} \cos(\theta_p) &= \frac{-\beta+\cos(\theta_{lab})}{1-\beta\cos(\theta_{lab})} \\ \frac{d\Omega'}{d\Omega} &= \frac{1}{\gamma^2(1-\beta\cos\theta)^2} \end{aligned} \tag{4.18}$$

Applying this transformation to $d\sigma_{REC}(\theta')/d\Omega'$, one obtains the simple angle differential cross section dependence in the laboratory frame:

$$\frac{d\sigma_{REC}(\theta)}{d\Omega} \approx \sin^2\theta \tag{4.19}$$

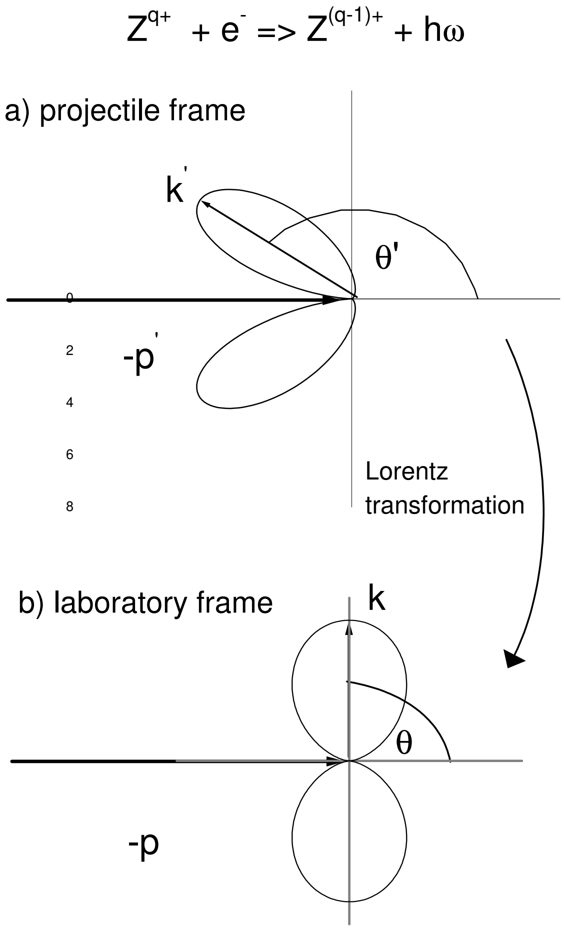

Figure 4.3: Photon angular distribution for REC into U^{92+} ions at 295 MeV/u, in the projectile frame (top figure) and laboratory frame (bottom figure), calculated by assuming only electric interaction. The Lorentz transformation to the laboratory frame re-establishes the nonrelativistic $\sin^2\theta$ distribution, as observed experimentally.

Thus, the backward shift of the REC distribution in the projectile system relative to the direction of projectile motion, caused by retardation, is canceled by the forward shift due to Doppler transformation (see Fig.4.3), and the forward-backward symmetry is established, as observed experimentally. In the above, the magnetic interaction is not considered. For heavier systems and even higher energies, and also for states with angular momentum different from 0, this cancellation is no longer valid.

In this rigorous treatment of radiative capture in relativistic atomic collisions, it has been shown that significant deviations from a $\sin^2\theta$ distribution may occur even more for the case of the L subshells. In particular, it has been pointed out that spin-flip processes are directly measurable in the angular distribution. Quite generally the differential cross section for RR into $l = 0$ states of a spinless electron vanishes in the forward and backward direction because initial and final states have $m_l = 0$, so that the emission of a transverse photon with angular momentum $\pm$ 1 in its direction of motion is forbidden by the conservation of the angular momentum. This means that RR into l=0 states at forward and backward angles can only occur by spin-flip processes due to magnetic interactions in a relativistic description [86], [42], [40], [10]. Spin flip transitions are able to create the angular momentum of the emitted photon.

The exact theoretical radiative recombination angular distributions as a function of the projectile energy and nuclear charge number Z have been presented in detail in Ref. [43]. For capture in the s-states, the non-spin-flip cross sections vanish at 0° and 180°. At small values of Z (smaller than 50), the angular distributions are practically pure $\sin^2$ distributions at all energies considered.

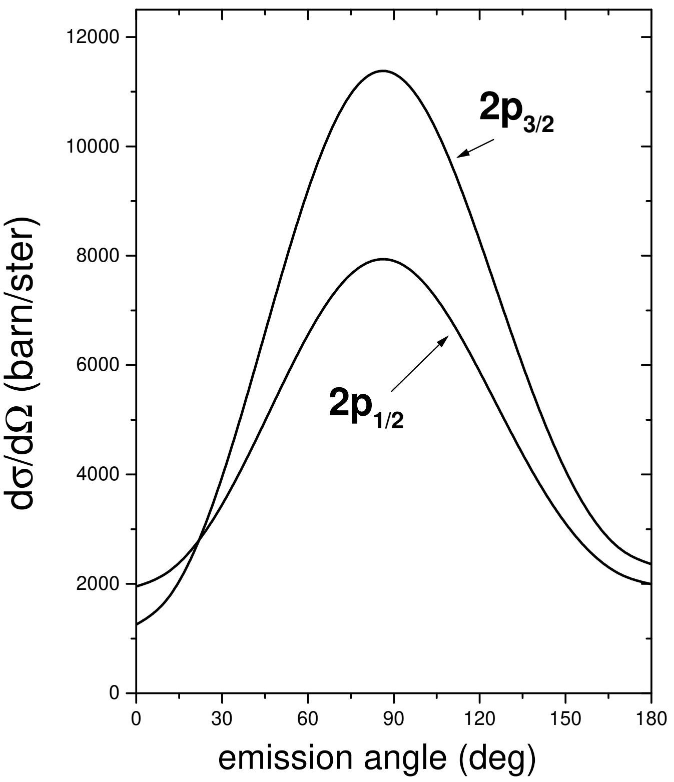

Figure 4.4: Angular distributions for radiative recombination into the *2p*-states of bare uranium, at 0.1 MeV/u as given by complete relativistic calculations [43]. The differential cross sections have significant values at 0° and 180° and they are slightly peaked towards backward angles.

As the projectile charge increases, the maxima of the angular distributions are shifted in the forward direction. Also, with increasing charge as well as with increasing projectile velocity, the relative contributions of the spin-flip transitions gain weight, leading to a finite cross section at forward and backward angles. The angular distributions for the L-shell, p-states tend to be more peaked towards backward angles and have appreciable values at 0° and 180°. With increasing projectile energy, RR into the l=0 ($2s_{1/2}$) shell becomes more important, because this shell contains higher momentum components necessary to fit to the fast moving electron. For the M-shell, the results are qualitatively similar to those of L-shell. The differential cross sections for the $3d_{3/2}$ are extremely asymmetric about 90° and show a dominant peak at around 120°; at 180° they are comparable to peak value and show a strong influence of the electron spin.

4.2.2 Angular Distribution at High Energies

Experimental technique

In this work, the first experimental study of a complete photon angular distribution for radiative electron capture into the K-shell of a bare high-Z ion (uranium Z = 92) will be described [81]. The measurements were done for laboratory observation angles from almost 0° to 150°, allowing the identification of spin-flip contributions that lead to photon emission at 0°. The electron angular distribution are deduced, considering the photoionization of hydrogenlike uranium, i.e., for an explicitly point Coulombic high-Z system. This is at present not accessible in the direct channel due to the lack of the necessary luminosity. This experiment became possible with the availability of high brilliance heavy ion beams at the ESR storage ring at GSI-Darmstadt. Typically, 10^8 bare $^{238}U^{92+}$ ions were accumulated in the ring at the energy of 309.7 MeV/u and cooled by electrons. A highly useful effect of electron cooling is that the ion energy is precisely determined by the acceleration voltage of the cooler. This also reduces the relative momentum spread to about 5×10^{-5} and provides a small beam size with a diameter close to 2 mm. After ion accumulation, the internal gas jet was switched on producing a N2 target of approximately 10^{12} particles/cm^2 areal density. The beam/ gas-jet interaction zone was determined to have a diameter of 5 mm. The jet target was equipped with a specially designed scattering chamber which now allows the simultaneous measurements of photon emission at 0°, 35°,60°,90°, 120°, and 150° with respect to the beam axis. In all cases, planar Ge(i) detectors were used (crystal thickness between 12 and 15 mm), separated from the ultra high vacuum of the ESR beam line by either 50 mm stainless steel or 100 mm beryllium windows. Except for 0°, all detectors were equipped with x-ray collimator slits, defining the effective active area of the detectors (depending on the observation angle in the range between 200 and 800 mm^2 at a typical distance to the jet target of 350 mm). The chosen collimator dimensions made it possible to resolve the splitting of the Lyα transitions into the Lyα_1 and Lyα_2 components (4.5 keV in the emitter frame). Projectiles having captured one electron were registered downstream beyond the next dipole magnet in a fast scintillator detector with a detection efficiency close to 100%. Only projectile x-rays which were in coincidence with these down-charged U^{91+} ions were recorded. In Fig.4.5 an x-ray spectrum measured at 150° in coincidence with electron capture is displayed (laboratory frame).

Here, the most prominent feature is due to radiative capture into the K shell of the projectile where the line width results from the momentum distribution of the quasi-free electrons bound in the N_2 molecule. Electron capture into excited states

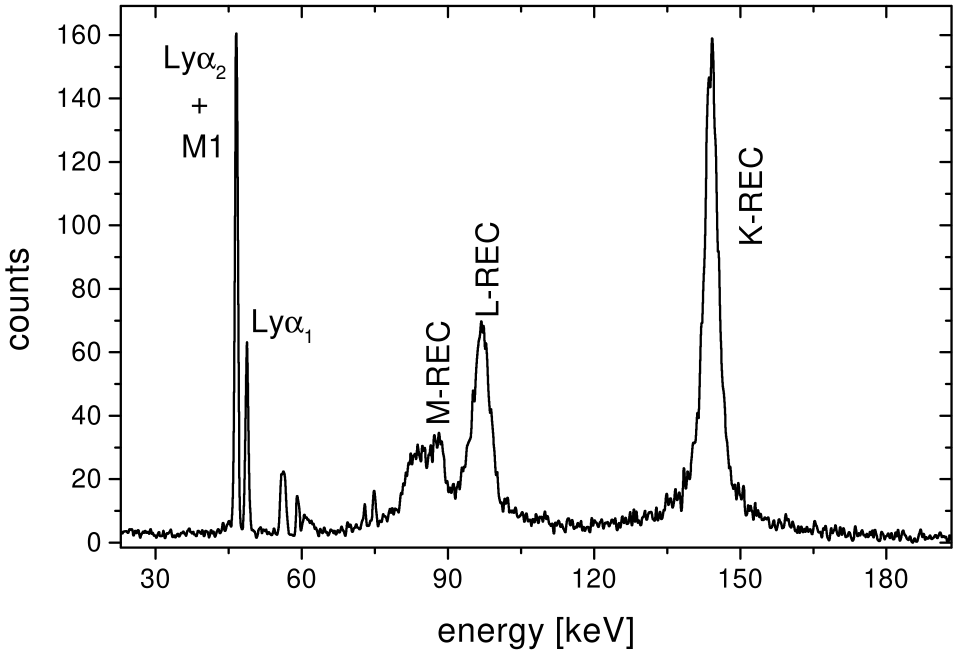

Figure 4.5: X-ray spectrum observed at nearly 150° for $U^{92+} \rightarrow N_2$ collisions at 309.7 MeV/u in coincidence with electron capture.

(L, M, and higher shells) is followed by cascades to the ground state producing the characteristic Lyman transitions with a narrow line profile.

For observation of x-rays in the forward hemisphere near the beam at 4.6°, the experiment benefits considerably from the clean experimental environment at the storage ring. In conventional single pass experiments with relativistic beams and solid targets, the production of secondary electrons and its related bremsstrahlung prevents photon detection close to the beam. In the current experiment, x-ray detection at almost 0° was accomplished by using a germanium detector with four independent segments, each of them with an individual readout. The horizontal and vertical sizes of each segment are 13 and 25 mm, respectively. The detector was mounted on a movable support, 510 mm downstream from the projectile-target interaction region. Periodically, after the accumulation procedure was finished, the detector was positioned at a perpendicular distance of just 1 cm from the circulating beam. For the first stripe, this position corresponds to a mean observation angle of 4.6° with an angular acceptance of $\Delta\theta = \pm 0.7°$.

In Fig. 4.6, a coincident x-ray spectrum, measured with the innermost segment of the Ge(i) detector is displayed. The K-REC line can be well identified at an x-ray energy of 660 keV. In addition, the Lyman transitions measured with the germanium detector are shown separately, demonstrating the good energy resolution obtained.

The procedure for data reduction has been described in detail elsewhere [82]. All x-ray spectra were first energy calibrated and corrected for detection efficiency.

Thereafter, the K-REC line profiles were fitted using a theoretical line shape based on the double differential cross section [42] which incorporates the correct Compton profiles of the target electrons. This method was applied to all spectra observed

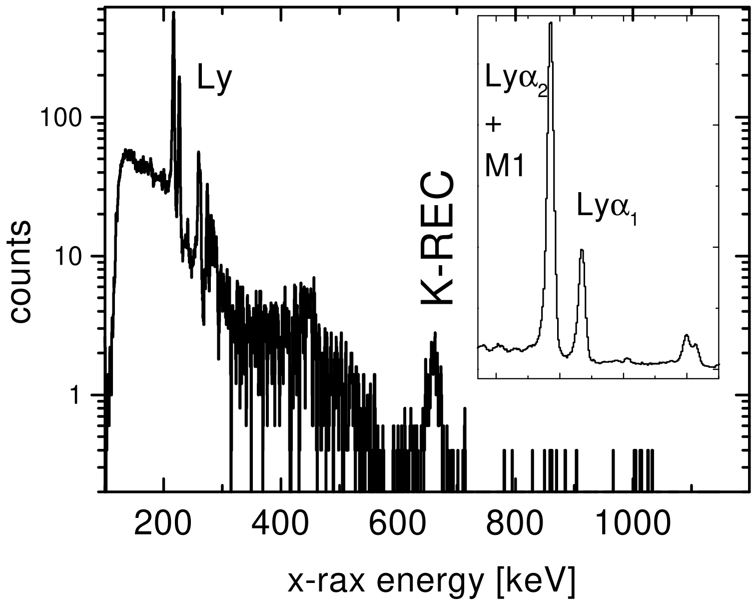

Figure 4.6: X-ray spectrum measured at nearly 0° observation angle for U^{92+} collisions at 309.7 MeV/u in coincidence with electron capture. The inset displays the subshell resolved Lyman transitions.

at the different observation angles, except for one of the four-fold detectors close to 0°. Here, the yield of K-REC photons was obtained from the sum of all events belonging to the relevant energy regime, subtracting a linear background. Since the determinations of absolute cross section values have usually only 30% precision, the relative differential cross sections were studied, which are much more precise. For this purpose the simultaneously observed Lyα_2 + **M1** transitions were analyzed. Since the Lyα_2 and the **M1** transitions arise from the decay of the $2p_{1/2}$ and the $2s_{1/2}$ levels, the corresponding line intensity is isotropic in the emitter frame and, consequently, its intensity pattern as a function of the laboratory observation angle is exactly known [87], being given by the relativistic solid angle transformation. All x-ray spectra were normalized by taking the Lyα_2 + **M1** as a reference line. The advantage of this technique is that the uncertainty caused by the determination of the solid angle is canceled. The only remaining uncertainty is introduced by the efficiency calibration. The latter was determined by using an absolutely calibrated mixed γ source (see, e.g., Ref.[82]). The efficiency correction was assumed to introduce an uncertainty of less than 5%.

Results and Discussion

In Fig.4.7, the measured differential cross sections for REC into the K shell of U^{92+} are presented as a function of the laboratory observation angle (solid triangles) and compared with predictions based on rigorous relativistic calculations [43]. These calculations use exact wave functions (see chapter 3) and take into account the finite nuclear size and all multipole orders up to about L=20. In order to achieve convergence, the summation was carried out over all electron partial waves with Dirac quantum numbers $|k| \leq 20$. For the comparison, the measured angular distribution was normalized to the theoretical prediction at 90°.

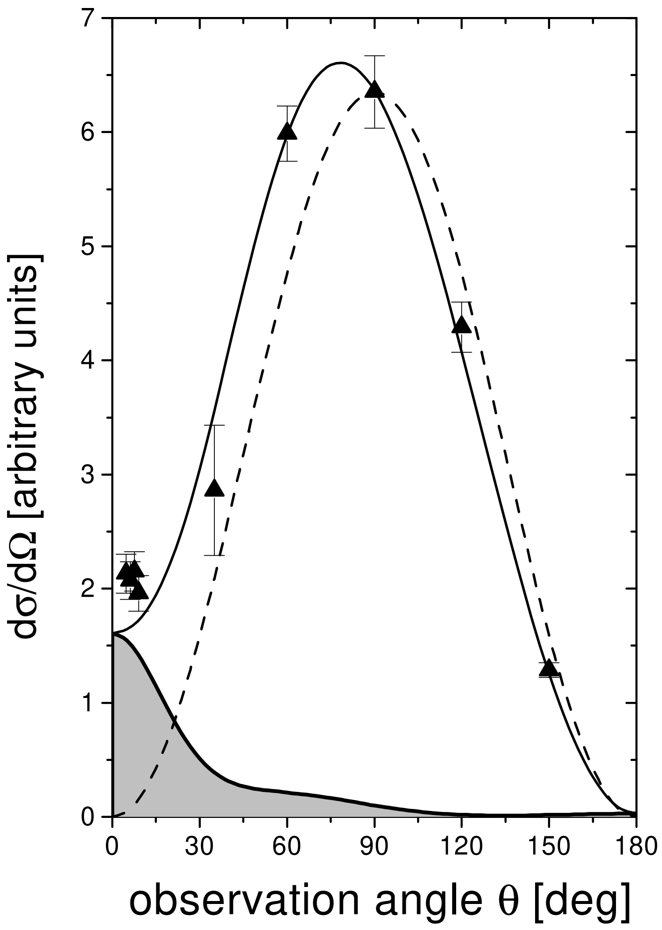

Figure 4.7: Angular distribution for REC into the K shell of bare uranium (solid triangles) as a function of the observation angle θ (309.7 MeV/u $U^{92+} \rightarrow N_2$). The solid line refers to complete relativistic calculations and the shaded area to the spin-flip contributions. The $\sin^2\theta$ shape of the nonrelativistic theory is given by the dashed line. The absolute values of the experimental data and of the nonrelativistic theory are normalized to the result of the complete calculations at 90°.

As seen in the figure, a very good agreement is obtained between the experimental data and the rigorous relativistic calculations. The necessity of a complete relativistic treatment for high-Z projectiles is shown in the figure by the $\sin^2\theta$ distribution given by the nonrelativistic treatment. The experimental data deviate considerably from symmetry around 90°. The large cross section observed at close to 0° is in contradiction with the assumption of a spinless electron or of a passive spin. Therefore, the measurement close to 0° provides an un-ambiguous identification of spin-flip transitions occurring in relativistic ion-atom collisions. This effect, predicted recently [88], [42], [43], has not been confirmed experimentally up to now. For example, for the case of Xe^{54+} $\rightarrow$ Be collisions at 197 MeV/u [89], no relativistic effects were observed and the measured K-REC angular distribution could be well reproduced by the nonrelativistic theory. In the relativistic Sauter approximation, in which the matrix element of the photoelectric effect is treated in the lowest order of αZ, spin-flip contributions at forward angles do not occur. Hence, these measurements prove that higher orders in αZ, which are automatically contained in the exact wave functions, are needed.

In order to elucidate the physics of the REC process and its relation to photoionization in more detail, the measured K-REC x-ray yield was normalized directly to the intensity of the simultaneously observed Lyα_2 + **M1** line. By applying this technique of normalization, the REC angular distribution in the emitter frame is obtained, requiring in addition only the Lorentz transformation of the observation angle. In Fig.4.8, this ratio is represented as a function of the emission angle in the emitter frame (the x-axis at the bottom) along with the corresponding results of the exact relativistic theory. Here it can be observed that both the experimental and the theoretical angular distributions have a pronounced backward shift, since the strong retardation effect (equivalently, the contribution of higher multipole orders) is no longer canceled by the Lorentz transformation to the observer system. The distribution has a maximum close to 150° and the cross section decreases significantly by more than a factor of 40 approaching 0°. Here the spin-flip transitions (compare shaded area in Fig.4.8) appear to be a small effect with an almost isotropic distribution. This is in clear contrast to the distribution in the laboratory frame, where the Lorentz transformation not only compensates retardation but also amplifies the relative weight of the spin-flip transitions close to 0° by more than an order of magnitude compared to the maximum of the distribution. This result compared to direct photoionization experiments shows that the observed spin-flip transitions are found at a lower energy because this effect appears to be enhanced by the Lorentz transformation.

From the experimental REC distribution in the emitter frame, the corresponding angular distribution for photoionization can also be derived by simply replacing the REC angle θ' with $\pi - \theta'$ since the roles of the photon and the electron are inversed. Therefore, the upper x-axis in Fig.4.7 refers to the electron angular distribution for photoionization of hydrogenlike uranium at the corresponding photon energy of 301.7 keV.

From the theoretical point of view, the advantage of a very simple single electron case is clear in contrast with the K-shell photoeffect in neutral atoms at high energies, where the screening effects and the electron correlations have to be taken into account. This shows the possibility of photoionization precision studies via the inverse reaction.

4.2.3 Angular Distributions for Decelerated Ions

In the following, the enhanced importance of spin-flip transitions due to Lorentz transformation will be used in order to study these effects at lower energy. In the usual photoionization studies for high-Z elements, the electron emission angle is enlarged by the electron scattering which occurs in solid targets. These corrections

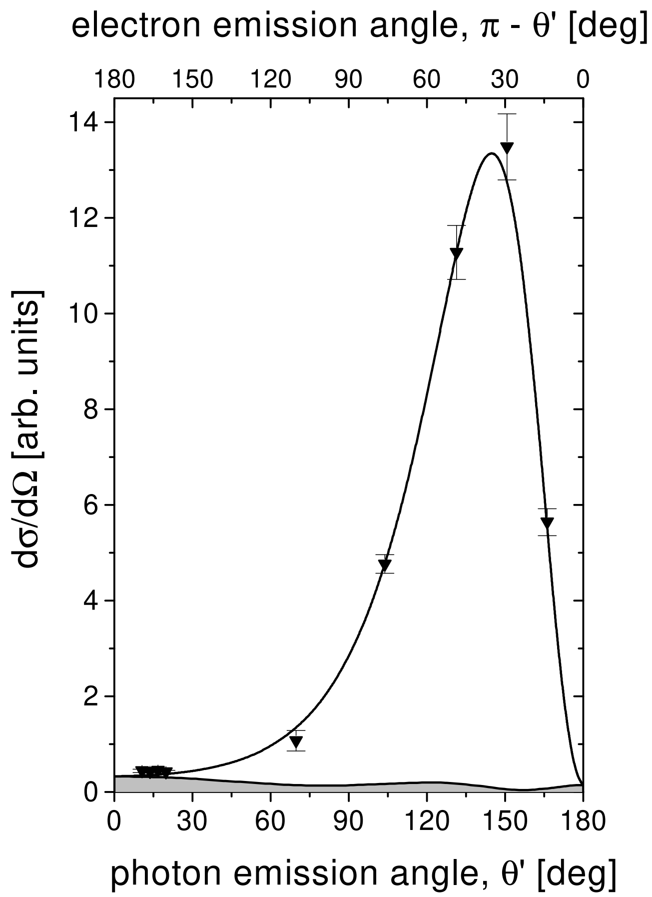

Figure 4.8: K-REC angular distribution (projectile frame) as a function of the emission angle θ (bottom x-axis). The x-axis at the top refers to the corresponding electron angular distribution for photoionization of H-like uranium (photon energy 301.7 keV) obtained by the interchanging θ' by $\pi - \theta'$. The full line gives the photoionization distribution as obtained from complete relativistic calculation. The shaded area represents the spin-flip contribution.

were not performed in the case of the few fine structure - sensitive data obtained in photoionization experiments, therefore almost no comparison with the theory predictions was possible. For electron capture, these corrections are not required and therefore the REC experiments allow the extension of photoionization studies to much lower photon energies than available in direct channel.

An angular-differential study of the time-reversed process was conducted at the jet-target for bare uranium ions in collisions with a N_2 target [7]. The ions were decelerated in the ESR to an energy of 88 MeV/u. This corresponds to a photoelectron energy of 48 keV, very small in comparison with the ground state ionization potential of H-like uranium of close to 132 keV.

REC into the K-shell as well as into the j-sublevels of the L-shell of bare uranium were measured at the same time. A sample x-ray spectrum (recorded at 150°) is depicted in Fig.4.9. In the spectrum the REC lines of interest show up as broad structures although the characteristic Lyman transitions are the most intense fea-

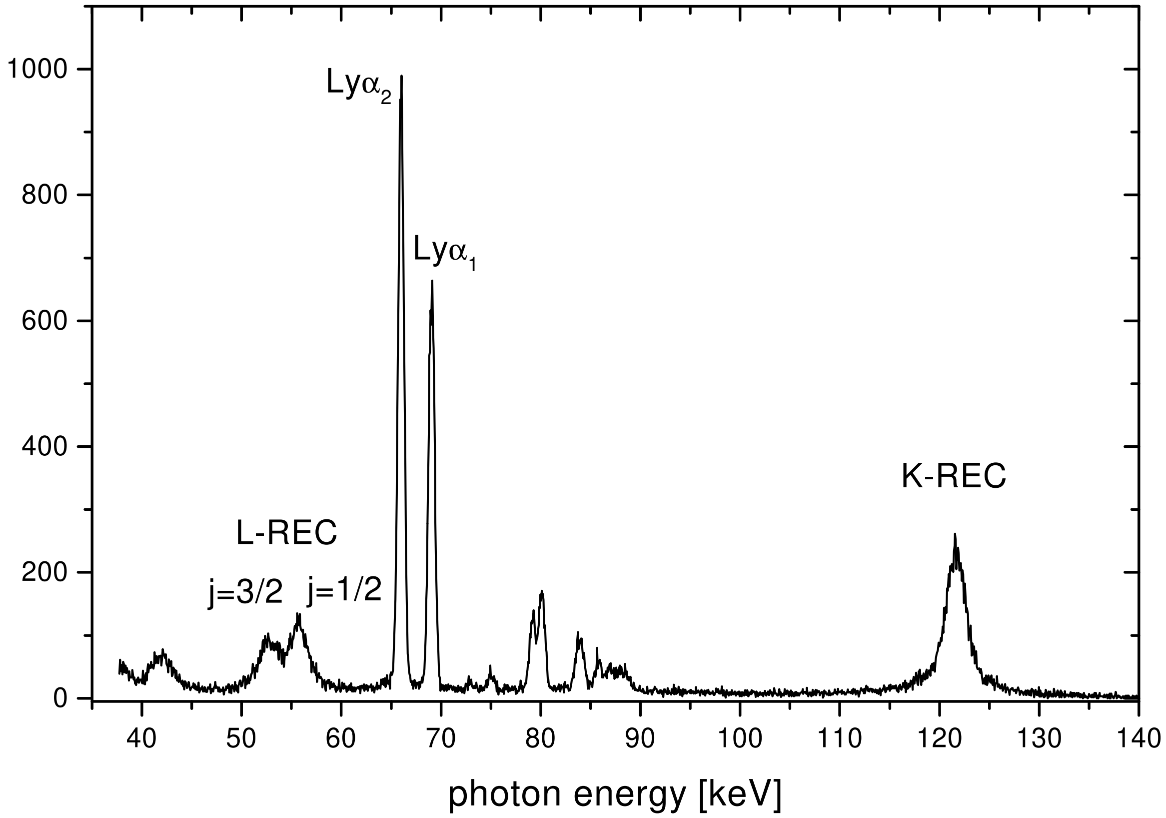

Figure 4.9: Sample x-ray spectrum recorded at 150° for $U^{92+} \rightarrow N_2$ collisions at 88 MeV/u.

tures of the spectrum. In particular, the simultaneous observation of Lyα_2+**M1** radiation allowed, as before, to obtain the electron angular distribution of the REC transitions. In Fig.4.10, the experimental results for K-REC are given as a function of the photon emission-angle in the emitter frame (solid circles).

It can be seen that even in this low-energy case, the distribution is still strongly peaked backwards corresponding to a strong forward peaking of the photoelectron in the time-reversed process. This shows the importance of the full retardation corrections, that have to be taken into account even in this low energy domain. In comparison with the theoretical calculations, [42] (full line in Fig.4.10), the good agreement supports the prediction that the higher multipole contributions persist even close to the threshold of the photoionization, Moreover, both theory and experiment show a non-vanishing cross-section close to 0° which proves that magnetic contributions are still present in the low-energy domain. This proves once more the sensitivity of this method since magnetic transitions contribute with only 3% to the total K-REC cross-section. A comparison with an angular distribution for high-energies was done, displaying in addition the results obtained recently for 310 MeV/u for $U^{92+} \rightarrow N_2$ collisions. This comparison illustrates the increasing impor-

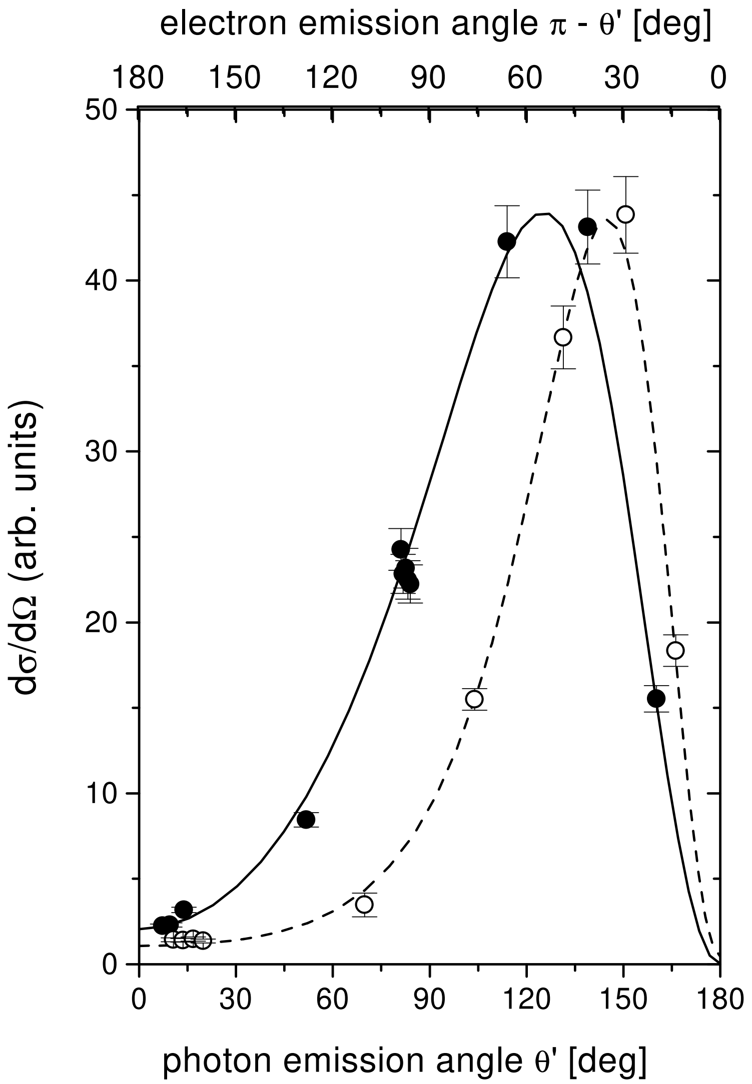

Figure 4.10: K-REC angular distribution (solid circles) as a function of the emission angle θ' (bottom x-axis) in the projectile frame. The x-axis at the top refers to the corresponding electron angular distribution for photoionization of H-like uranium (photon electron energy 48 keV). The full line gives the photoionization distribution as obtained from complete relativistic calculation. In addition, the results of a former experiment conducted at the high-energy of 310 MeV/u (photon energy of 170 keV) are shown for comparison (open circles and dashed line) [81].

tance of higher multipole contributions (retardation) with increasing energy leading to a much stronger backward peaking of the distribution.

A very important aspect of this investigation is that the very good experimental resolution due to the narrow Compton profiles at low beam energies allowed us to derive even j-subshell selective differential cross-sections for photoionization of the first excited states in hydrogenlike uranium. These data are given in Fig.4.11. There, the solid points refer to capture into the two j=1/2 fine structure components of the

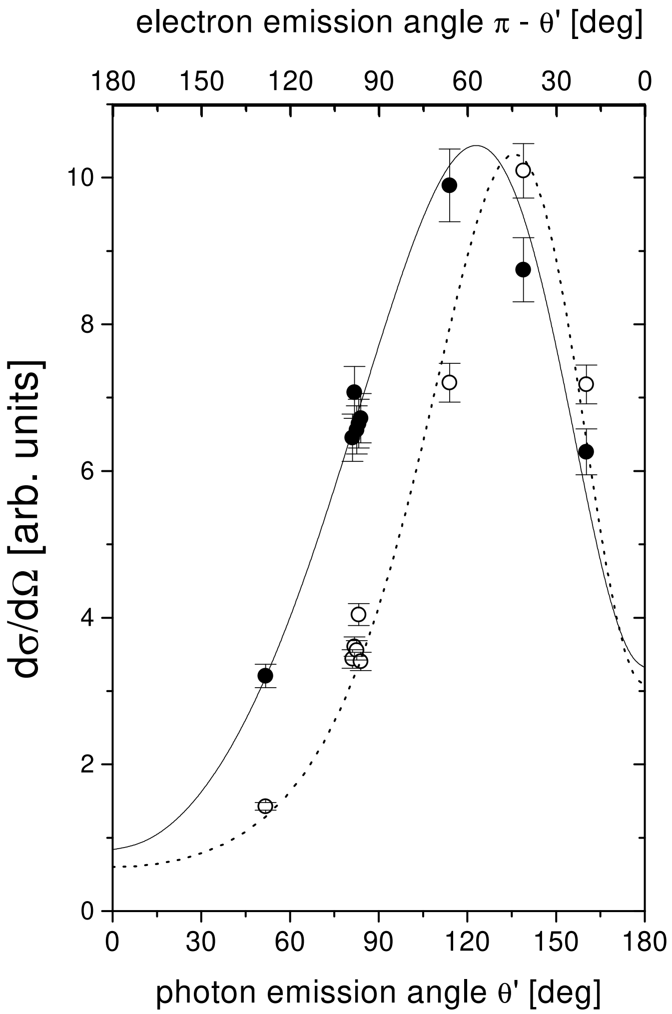

Figure 4.11: Experimental angular distribution for REC into the first excited states of H-like uranium as measured for $U^{92+} \rightarrow N_2$ collisions at 88 MeV/u (solid points: $2s_{1/2}$ and $2p_{1/2}$; open circles: $2p_{3/2}$ state). The data are compared with rigorous relativistic calculations. The lower x-axis refers to the emitter frame, the upper to the electron emission angle for photoionization with a kinetic photoelectron energy of 48 keV.

L-shell ($2s_{1/2}$ and $2p_{1/2}$) and the open circles give the data obtained for the $2p_{3/2}$ state.

The corresponding result of rigorous relativistic calculations are represented in the figure (full line: $2s_{1/2}$ and $2p_{1/2}$; dotted line: $2p_{3/2}$). To facilitate the comparison of the angular distributions for the different j-fine structure components, the $2p_{3/2}$ distribution was multiplied by a factor of 1.6. For the case of the j=1/2 distribution, the $2s_{1/2}$ gives the strongest contribution to the total sum, and the final behaviour is similar to the one observed for the K-shell. The differential cross-section observed for the experimentally isolated $2p_{3/2}$ level is much stronger peaked to backward angles. Its maximum appears for angles quite similar to the ones obtained for the K-REC distribution measured at the much higher energy of 310 MeV/u. This shows that the retardation corrections are much more significant in the case of p states than for s-states.

4.3 Conclusions

In summary, the measured photon angular distribution for radiative electron capture into the K-shell of U^{92+} from N_2 at a collision energy of 309.7 MeV/u corresponds to the time-reversed process of photoionization of hydrogen-like uranium at a photon energy of 301.7 keV. For bare U^{92+} projectiles at 88 MeV/u (photoionization of H-like uranium at a photon energy of 180 keV) in collision with a N_2 target the measurements were done at the same time for REC into the ground state as well as into j-sublevels of the L-shell.

By measuring at observation angles from nearly 0° to 150°, a strong forward peaking of the angular distribution was found due to notable relativistic contributions. The study of REC angular distributions proves thus to be a very sensitive probe for relativistic corrections. The precision of this technique is illustrated by the experimental separation and identification of the spin-flip transitions. In particular, the observation of photon emission close to 0° allowed a precise measurement of spin-flip contributions to the differential K-REC cross sections for the first time. In this way, for a high projectile charge and relativistic projectile motion, the electron spin manifests itself as it was recently predicted by complete relativistic theory. Quantitatively also, a very good agreement can be seen from the comparison with theory. At the same time, the experiment allowed the measurement of angular distribution for photoionization of hydrogen-like uranium U^{91+}, measurements that are not accessible in the direct process. The results demonstrate that the applied method is a powerful tool for these investigations, in particular in the low energy domain.

The structure of the photon spectra allowed the separation of the radiative capture into the ground state from the capture into excited states, moreover, the fine-structure components of the L shell could be resolved. Here, the experimental results underline once more the importance of the angular momentum of the final state. In particular, the data confirm the relativistic prediction that for p-states the retardation effects appear more pronounced than in the case of s-states, where the retardation is completely cancelled by the Lorentz transformation. This measurements allowed for the very first time the study of differential data for photoionization of a high-Z element in the low-energy regime.

Chapter 5

Investigations of highly charged high-Z projectile X-ray production induced by electron capture

5.1 Introduction

The previous chapters have treated the radiative electron capture and the radiative recombination as fundamental processes in ion-atom and ion-electron collisions. In the following, the *non-radiative capture* will be brought in attention as a competing process along with the *radiative capture* in the transfer process of the electron between a target and an excited state of the fast moving projectile. Electron capture is followed by cascade transitions (therefore, emission of radiation) from the initial state in which the electron is captured, to lower lying states of the projectile. In order to analyze these X-ray spectra that are produced, these two relevant capture processes have to be taken into account.

For the radiative electron capture both non-relativistic and exact relativistic existent theories describe extremely well and in detail this process. The calculations of total and differential cross sections show an excellent agreement with the experimental data. However, in spite of the fact that several theories have been proposed in the last years for the description of non-radiative electron capture, this process still lacks a complete relativistic theoretical treatment which could be applied.

In the non-relativistic energy domain, the process of capture is almost entirely governed by the so-called $non-radiative\ electron\ capture$ process NRC (see chapter 1), where the energy and the momentum transfer in the collision are distributed between the projectile, the target and the captured electron.

From the non-relativistic capture theory it is known that for large projectile velocities v the non-radiative charge exchange cross sections decreases asymptotically as v^{-12} or E^{-6} in first order and as v^{-11} or $E^{-11/2}$ in second-order perturbation theory. This dramatic velocity dependence occurs because the overlap in momentum space between initial and final wave functions quickly diminishes as the relative velocity increases. Also, its cross section follows a strong dependence on the projectile and target atomic charge numbers (Z_p and Z_T) :

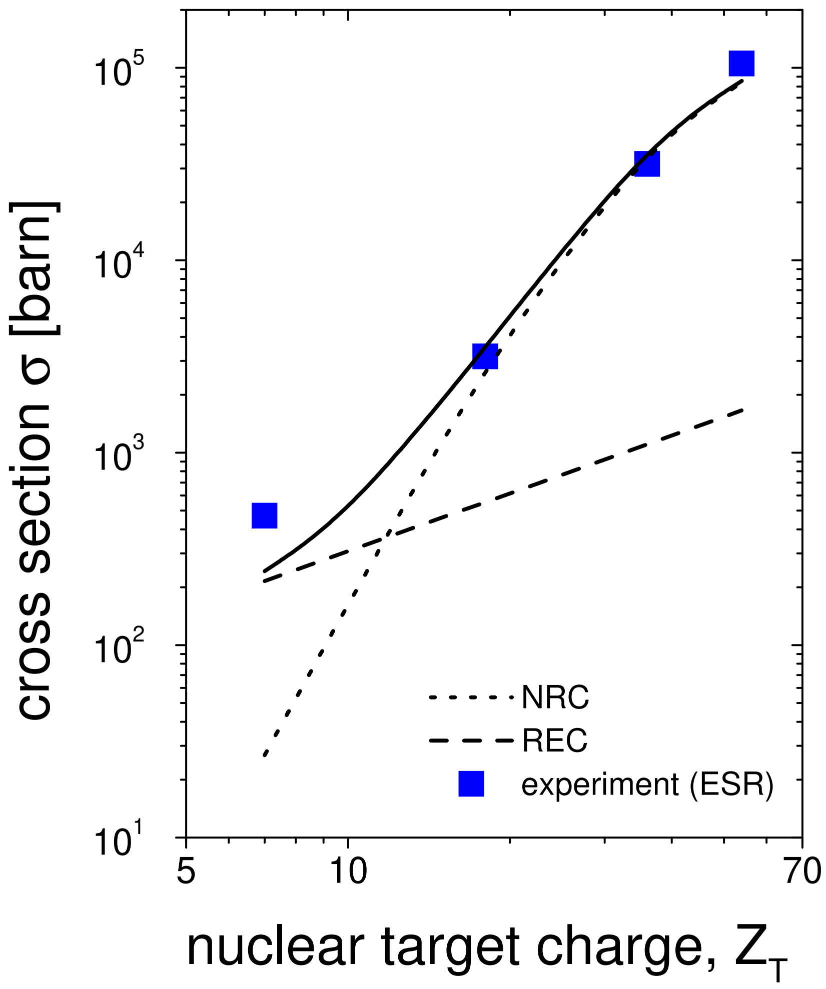

Figure 5.1: Target atomic number (Z_T) dependence of the total electron capture cross sections for 220 MeV U^{92+} interacting with gaseous targets. The dotted line represents the result of the eikonal approach for NRC process. The dashed line gives the prediction obtained within the dipole approximation for REC process. The solid line refers to the sum of both predictions.

$$\sigma_{NRC} \approx \frac{Z_T^5 \times Z_P^5}{v^{12}} \tag{5.1}$$

The question that arises is if at relativistic velocities is there any measurable cross section left. There is a simple qualitative reason why the relativistic cross section decreases less rapidly with the collision energy than the non-relativistic calculation would predict: the Lorentz contraction of the electron space wave function in the beam direction leads to extended momentum wave functions in this direction and thus the overlap in momentum space has a slower decrease. Actual calculations show, almost independently of the type of approximation, that the relativistic capture cross section decreases only with approximately E^{-1} rather that with E^{-6}.

However, in the ultra-relativistic limit the non-radiative capture plays a negligible role. At highly energetic collisions, the electron transfer is entirely determined by *radiative electron capture* (REC) (see chapter 3). The general scaling laws of REC can be derived from the non-relativistic dipole approximation of Stobbe, and can be written as:

$$\sigma_{REC} \approx \frac{Z_T \times Z_P^5}{v^{5/2}} \tag{5.2}$$

Fig. 5.1 shows the dependence of REC and NRC cross sections on the target atomic number Z_T for 220 MeV/u He-like uranium ions. It can be seen from the figure that for target heavier than argon NRC is the most important process, even at this highly energetic collisions.

Up to now, few state selective information about electron capture was available in the domain of intermediate and fast collisions. For high-Z ions, however, the spectroscopic studies of *nlj*-sensitive population cross-sections are accomplished by the large fine-structure splitting present. The latter allowed to obtain population cross section for specific projectile states from the Balmer [1] of bare U ions on N_2 target, produced by electron capture [44], [82]. The reported studies of state selective capture include the characteristic Lyman lines of H-like Bi ions on solid target.

In the following, the population cross sections for specific projectile states from the measured Balmer spectra produced in collisions between He-like uranium ions and different gaseous targets will be presented, in order to obtain precise *nlj*-selective information about electron transfer into high-Z projectiles by comparison with the capture theories available.

This type of theoretical analysis of the x-ray production and decay dynamics of excited states is also useful in the understanding of the feeding and cascade population in the case of U^{91+} in collision with solid and gaseous matter, which will be discussed in the second part of this chapter. Emphasize has been paid particularly to the formation of the $^3P_0$ and $^3P_2$ levels by using electron capture into hydrogen-like U. Both states are of interest for precise measurements on high-Z helium-like ions in future experiments already planned at the GSI accelerator facilities.

5.2 Investigations of electron capture for U^{90+}

5.2.1 Continuum Distorted Wave Approximation

As is already mentioned in the chapter 2 of this thesis, the simplest and earliest approach to relativistic electron capture is the relativistic version of the first-order plane-wave or Oppenheimer-Brinkman-Kramers (OBK) approximation [90, 91]. In this method, the projectile and the target atoms are considered bare and hydrogen-like systems, i.e. the initial and final electron states, assumed to be undistorted atomic eigenstates ψ_i and ψ_f of target and projectile, respectively, are described by

[1] transitions from states with the principal quantum number n $>$ 2 into the L-shell

hydrogenic wave-functions. Strictly speaking, this assumption is not valid since a Coulomb field leads to distortions even at infinite distances. However, similarly as for non-relativistic collisions, the OBK approximation fails to reproduce measured total cross sections. For example, calculated OBK cross sections for 1050 MeV/u Ne on targets with charge numbers between 13 and 92 are almost a factor of 10 too large in relation with the data. The second-order Born approximation has been often regarded as the appropriate method to describe electron transfer in ion-atom collisions at high projectile energies. This should be valid in particular for relativistic collisions. It was found in an exact evaluation of the second-order Born approximation (OBK2) that the calculated cross sections are considerably larger than the first order cross sections, that already overestimate the experimental results [92]. Another relativistic theory is the eikonal approximation, which in comparison with the OBK approximation shows that the eikonal cross section is significantly smaller than the OBK and still much smaller than the second-Born approximation result. In fact, it has been shown, [93] that this reduction brings calculated cross sections in rather good agreement with experimental data for a number of collision systems and energies. In comparison with the continuum-distorted wave (CDW) theory it has been shown by Stöhlker [94], at beam energies of 49 MeV/u and 68 MeV/u that both theories predict very similar final n, l distributions and therefore give almost identical Balmer spectra. However, in the case of the eikonal approximation, only the post-version (see chapter 2) was found to describe correctly the cross section data. Still, for high-Z targets, there are differences from the measured non-radiative capture cross sections, up to a factor of 2 [82]. In contrast with the before mentioned theories, which are symmetric in the entrance and exit channel, (so interchanging the target and the projectile nothing changes in the results), the eikonal theory is an asymmetric theory (see chapter 2). The decision of which version to use in the calculations (prior or post) brings difficulties because it depends on the quantum number n of different levels for the same atom (target or projectile). In this way, artificial jumps in the n, l distribution may appear, and the description becomes inconsistent. In order to overcome this, in the following a continuum-distorted wave theory (CDW) has been chosen to be discussed in comparison with the experimental data, for various targets with increasing atomic number. The CDW theory, as well as the eikonal approximation is a theory for high energy collisions. However, CDW has the big advantage of taking into account the momentum distribution of the electrons in the target, so the wave functions are not any more hydrogenic wave functions.

In the case of two nuclei and a single electron, the classical treatment of the internuclear motion reduces the three-body problem to the motion of the electron in the time dependent fields of the projectile and the target nucleus. The wave function can be obtained from the three body approaches with the nucleus-nucleus interaction considered zero. As the scattering wave function enters into the exact transition amplitude, the methods for evaluating this function can be used to calculate the transition amplitude.

In the semiclassical approximation, the electronic Hamiltonian consists of the kinetic energy T_e plus a time dependent interaction W. It is useful to split H_e into an unperturbed part H_0 which defines the asymptotic states, and a small perturbation

V. For rearrangement collisions, the splitting of H_e is different for the initial channel i and the final channel f, causing the perturbation to be not necessarily small:

$$\begin{aligned} H_e = T_e + W(\mathbf{r}, \mathbf{t}) = & \quad H_{i0} + V_i \\ & = H_{f0} + V_f \end{aligned} \tag{5.3}$$

The initial and final states φ_i and φ_f are eigenstates to H_{i0} and H_{f0}, respectively. The theory is built upon distorted waves χ_i, χ_f which include the perturbation in the entrance and exit channel. A formulation with distorted waves aims at a good approximation of the transition amplitude already with the lowest-order expansion term of the series. The distorted waves are defined by the introduction of an arbitrary splitting of the Hamiltonian in the entrance and the exit channel

$$H_e = H_i + \hat{V}_i = H_f + \hat{V}_f \tag{5.4}$$

.

Correspondingly, distorted waves χ_i and χ_f are defined as eigenstates to H_i and H_f, respectively. In the general case they don't coincide with φ_i and φ_f, but reduce to them asymptotically.

Let us write the potentials $\hat{V}_i$ and $\hat{V}_f$ in the following form:

$$\hat{V}_i = (H_e - i\delta_t)|\chi_i^+ >< \chi_i^+|, \; \hat{V}_f = (H_e - i\delta_t)|\chi_f^+ >< \chi_f^+| \tag{5.5}$$

The CDW theory emerges from the special choice of distorted waves which include both the projectile and the target field to all orders. This choice aims at a fast convergence of the series because the long-range interactions are avoided in $\hat{V}_i$ and $\hat{V}_f$.

The distorted waves are constructed as product of bound-state function to one potential and a continuum function to the other. If a frame is centered at the midpoint between the projectile and target nucleus is taken as the reference frame, a corresponding transformation $\hat{U}$ is necessary. Explicitly, the distorted waves are

$$\begin{aligned} \chi_i^+(\mathbf{r}_P, \mathbf{r}_T) &= e^{-iv^2t/8 - i\mathbf{v}\mathbf{r}'/2 - i\epsilon_i t}\varphi_i(\mathbf{r}_T)\hat{\psi}_{-\mathbf{v}}^{(+)}(Z_P, \mathbf{r}_P) \\ \chi_f^+(\mathbf{r}_P, \mathbf{r}_T) &= e^{-iv^2t/8 - i\mathbf{v}\mathbf{r}'/2 - i\epsilon_f t}\varphi_i(\mathbf{r}_T)\hat{\psi}_{\mathbf{v}}^{(-)}(Z_P, \mathbf{r}_P) \\ \hat{\psi}_{\mathbf{v}}^{(\pm)}(Z, \mathbf{r}) &= e^{\pi Z/2v}\Gamma(1 \mp iZ/v)\,{}_1F_1(\pm iZ/v, 1, \pm ivr - i\mathbf{v}\mathbf{r}), \end{aligned} \tag{5.6}$$

where $\mathbf{r}'$ is the coordinate with respect with the midpoint and ${}_1F_1$ is a confluent hypergeometric function. The functions $\hat{\psi}_{-\mathbf{v}}^{(+)}$ and $\hat{\psi}_{\mathbf{v}}^{(-)}$ are proportional to incoming and outgoing functions, respectively. However, the distorted waves (5.6) are not exact solutions to H_e because of the non-orthogonality of the coordinates $\mathbf{r}_P$ and $\mathbf{r}_T$.

Let us consider now charge exchange of the general type [95]:

$$A^{(p)+} + B^{(q)+} = A^{(p-1)+} + B^{(q+1)+} \tag{5.7}$$

where A and B are multielectron atoms and/or ions. Let Z_σ ($\sigma = A, B$) be the nuclear charge and let i and f be the usual sets of quantum numbers, such as: $i \equiv N_B = n_B, l_B, m_B$ and $f \equiv N_A = n_A, l_A, m_A$. For convenience we choose the "prior" form for the total cross-section for process (1) which, in the CDW approximation, is given by:

$$Q_{if}^{-}(\pi a_0^2) = \frac{1}{\pi}(2\pi v)^{-2} \int d\eta_\perp |T_{if}^{-}(\eta_\perp)|^2, \tag{5.8}$$

where v is the relative velocity, $\eta_\perp$ is the vector of the transverse momentum transfer and T_{if}^{-} is the transition amplitude

$$T_{if}^{-} = -N(\nu_A)N(\nu_B)\mathbf{I}(f) \cdot \mathbf{J}(i). \tag{5.9}$$

Here, we have

$$N(\nu_\sigma) = \Gamma(1 - i\nu_\sigma)exp(\pi\nu_\sigma/2);\ \nu_\sigma = \xi_\sigma/v;\ (\sigma = A, B) \tag{5.10}$$

with Γ - the gamma function and $\xi_{A,B}$ for effective charges [96] :

$$\xi_A = (-2n_f^2\epsilon_f)^{1/2},\ \xi_B = (-2n_i^2\epsilon_i)^{1/2}, \tag{5.11}$$

where ϵ_i and ϵ_f are orbital energies of the initial and final states, respectively.
Integrals $\mathbf{I}$ and $\mathbf{J}$ are defined by

$$\mathbf{I}(f) = \int d\mathbf{s}\ exp(i\rho_A \cdot \mathbf{s})\phi_f^*(\mathbf{s})\nabla_s {}_1F_1(i\nu_A, 1, i\mathbf{v} \cdot \mathbf{s} + ivs), \tag{5.12}$$

$$\mathbf{J}(f) = \int d\mathbf{s}\ exp(i\rho_B \cdot \mathbf{x})\phi_f^*(\mathbf{s}) {}_1F_1(i\nu_A, 1, i\mathbf{v} \cdot \mathbf{x} + ivx)\nabla_x \phi_i^*(\mathbf{x}), \tag{5.13}$$

where ϕ_i and ϕ_f are the initial and final orbitals, and

$$\begin{aligned} \rho_{A,B} = \pm\eta_\perp - \left(\frac{v}{2} \pm \frac{\Delta E}{v}\right)\hat{\mathbf{v}} \equiv \pm\eta_\perp - E^{\pm}\hat{\mathbf{v}}, \\ \delta E = \epsilon_f - \epsilon_i,\ \eta_\perp \cdot \mathbf{v} = 0(\hat{\mathbf{v}} = \mathbf{v}/v). \end{aligned} \tag{5.14}$$

We assume that both ϕ_i and ϕ_f can be expanded as follows

$$\phi_i(\mathbf{x}) \equiv \phi_{NB}(\mathbf{x}) = \sum_\beta B_\beta^B \chi_\beta^B(\mathbf{x}). \tag{5.15}$$

$$\phi_f(\mathbf{s}) \equiv \phi_{NA}(\mathbf{s}) = \sum_\alpha A_\alpha^A \chi_\alpha^A(\mathbf{s}). \tag{5.16}$$

with A_α^A and B_β^B being expansion coefficients and χ's normalized Slater-type orbitals [97]:

$$\chi_\gamma^\sigma(\mathbf{r}) = \left\{ \left[(2n_\gamma^\sigma)!\right]^{-1/2} \left(2\lambda_\gamma^\sigma r\right)^{1/2+n_\gamma^\sigma} exp\left(-\lambda_\gamma^\sigma r\right) Y_{l_\sigma m_\sigma}(\hat{\mathbf{r}}) \right\} \tag{5.17}$$

where n_γ^σ is the orbital number, and $\{\alpha\} = \{n_\alpha^A, l_A, m_A\}$,$\{\beta\} = \{n_\beta^B, l_B, m_B\}$, ($\gamma = \alpha, \beta; \sigma = A, B$).
Inserting eqs. 5.15,5.16 into 5.12,5.13 we have

$$I(f) = \sum_\alpha A_\alpha^A I'(\alpha), \tag{5.18}$$

$$J(i) = \sum_\beta B_\beta^B J'(\beta). \tag{5.19}$$

where

$$\mathbf{I}'(\alpha) = (-)^{m_A} U(\rho_A; \alpha'),\ \mathbf{J}'(\beta) = \mathbf{W}(\rho_B; \beta),\ \alpha' = \{n_\alpha^A, l_A, -m_A\}$$

and

$$\mathbf{U}(i\rho_\sigma; \gamma) = \int d\mathbf{r} exp(i\rho_\sigma \cdot \mathbf{r}) \chi_\gamma^\sigma(\mathbf{r}) \nabla_{r\,1} F_1(i\nu_\sigma, 1, i\mathbf{v}\cdot\mathbf{r} + ivr), \tag{5.20}$$

$$\mathbf{W}(\rho_\sigma; \gamma) = \int d\mathbf{r} exp(i\rho_\sigma \cdot \mathbf{r})_1 F_1(i\nu_\sigma, 1, i\mathbf{v}\cdot\mathbf{r} + ivr) \nabla_r \chi_\gamma^\sigma(\mathbf{r}), \tag{5.21}$$

The two auxiliary vectorial integrals **U** and **W** belong to the class of so-called "Coulomb" integrals containing Slater-type orbitals, which have been studied in detail by Belkic [98]. The calculation of integrals **U** and **W** is performed by means of Bessel integrals, reaching analytical expressions that include Appel hypergeometric function of two variables, which can be expressed as finite series. From here, the scalar product $I \cdot J$ is obtained:

$$\begin{aligned} \mathbf{I}(f) \cdot \mathbf{J}(i) &= (-)^{m_A + m_B} (2\pi)^2 exp\{i(m_B - m_A)\psi_{\eta_\perp}\} \\ & \sum_{\alpha,\beta} \sum_{q_A=0}^{l_A-\mu_A} \sum_{q_B=0}^{l_B-\mu_B} A_\alpha^A B_\beta^B \mathcal{D}_\alpha^{q_A} \mathcal{D}_\beta^{q_B} (a+b+c) \\ &\equiv (-)^{m_A+m_B} exp\{i(m_B - m_A)\psi_{\eta_\perp}\} R_{if}^-(\eta_\perp), \end{aligned} \tag{5.22}$$

in order to express the transition amplitude (5.9). Inserting (5.22) in (5.8) and performing the integral over $\psi_{\eta_\perp}$, the total cross section is:

$$Q_{if}^- = \frac{2}{(2\pi v)^2} \frac{2\pi\nu_A}{1 - e^{-2\pi\nu_A}} \frac{2\pi\nu_B}{1 - e^{-2\pi\nu_B}} \int_0^\infty d\eta_\perp \eta_\perp |R_{if}^-(\eta_\perp)|^2. \tag{5.23}$$

The program developed by Dž. Belkić et al. [98] was used in order to calculate the NRC cross section for electron capture into projectile (n, l) states. Being a non-relativistic calculation, we adopted a collision energy for which the projectile velocity matches the one given by the relativistic expression, i.e. 223 MeV/u for the projectile corresponds to 162 MeV/u non-relativistic collision energy. The input files contain exponents of the basis functions and the coefficients to be used in analytic atomic wave functions expanded in the Roothaan-Hartree-Fock method. The target and projectile wave functions are thus described by linear combinations of Slater type orbitals. Also in the input, the atomic mass, the charge and the energy of the projectile in keV in the laboratory frame are needed. The output files include the cross sections for one electron in the orbital, therefore the cross section is multiplied by the occupation number corresponding to the orbital. For the spectra simulation, the j-selective cross sections are needed, and are obtained from the n, l values using the statistical weights:

$$\sigma_{(nlj)}^{NRC} = \frac{2j+1}{2(2l+1)}\sigma_{nl}^{NRC} \tag{5.24}$$

For the *prompt* capture of electrons inside the target, the same approximations as for bare ions can be applied also for Helium-like ions since an electron capture occurs for high-Z ions predominantly into highly–excited subshells, rather independent of the additional $1s$ electrons. Therefore, for the REC process the cross section for electron capture from different shells of target atoms into specific projectile levels nlj, σ_{nlj}^{REC} are deduced from the exact relativistic nl cross sections for bare uranium calculated by Eichler [80], applying the n^{-3} scaling law. Finally, the total electron capture cross sections were obtained as a sum of REC and NRC cross sections.

$$\sigma_{nlj}^{tot} = \sigma_{nlj}^{NRC} + \sigma_{nlj}^{REC} \cdot N_e \tag{5.25}$$

where N_e is the number of electrons in a target atom.
In the chapter 1 of this work, a brief discussion about transitions, transition energies and transition rates was made. In the following, a short description of the experiment will presented.

5.2.2 Description of the experiment

In this experiment, charge exchange cross sections were studied for He-like uranium ions at the ESR storage ring. The electron pickup cross sections were obtained in collisions of 223 MeV/u U^{90+} with N_2, Ar, Kr and Xe gaseous targets.
The study of electron-capture processes by U^{90+} ions was performed at the heavy-ion synchrotron and storage ring facility SIS and ESR. The experimental arrangement at the ESR gas target was shown in Fig. 2.5. More detailed experimental arrangement at the gas target is shown in Fig. 5.2.
He-like uranium ions, delivered by the SIS with an initial energy of 358 MeV/u, were stacked and accumulated in the ESR storage ring. In the electron-cooler device, the ions were cooled to the final beam energy of 223 MeV/u by an electron beam of 200 mA providing U^{90+} ions with a relative momentum spread of about 5×10^{-5} . Typically, 10^8 uranium ions were stored and cooled, forming a beam with a diameter (full width at half maximum) of 2 mm. After completion of the cooling cycle, the gas-jet device was switched on. N_2, Ar, Kr and Xe gaseous targets with densities between 10^{11} and 10^{12} particles/cm^2 were used. The beam energy loss, caused by the interaction of the ions with the gas target, was compensated by the continuously

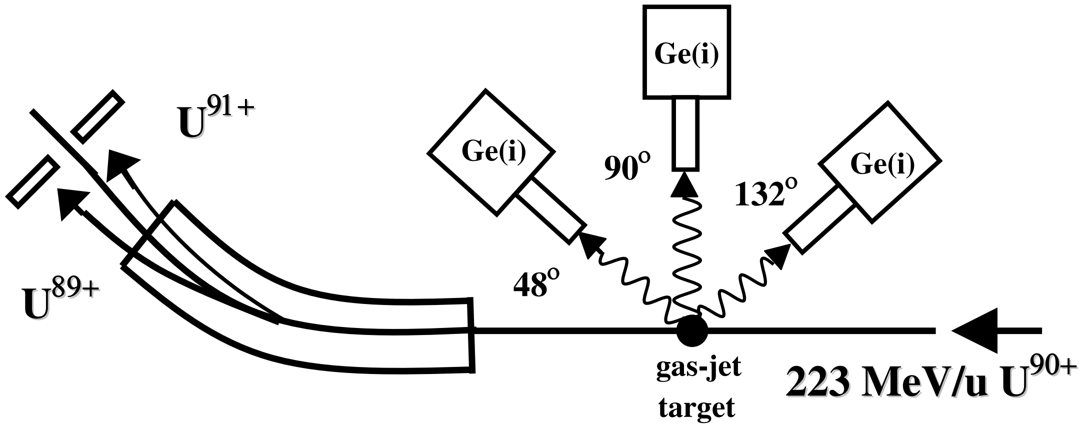

Figure 5.2: Simplified diagram of the experimental setup at the internal gas-jet target of the ESR. The x-rays are detected in coincidence with the down-charged lithium-like U^{89+} ions.

active electron cooler. By applying this procedure, up to 2×10^7 ions could be decelerated with an efficiency close to 80%. The current of the beam was measured by means of a calibrated current transformer, while the revolution frequency and momentum spread of the stored ions were monitored by means of Schottky noise analysis. The x-rays emitted from the reaction volume were registered by three thick planar Ge(i) detectors mounted at observation angles of 48°, 90°, and 132° with respect to the beam axis (see Fig. 2.5). In front of the x-ray Ge(i) detectors placed at 48° and 90° slotted copper and lead assembly with 5 mm opening were mounted to reduce the Doppler broadening. The projectiles which captured one electron from the target atom were registered in a particle detector behind the first bending magnet down-stream from the interaction region. The distances between the x-ray detectors and the gas jet are known to a precision of better than 2 mm, which introduces an uncertainty for the solid angle of the x-ray detector of close to 1%. By using sophisticated, laser-assisted measurements of the x-ray/jet-target geometry, used in spectroscopy experiments, this value can still be improved and an uncertainty below the 1% level is feasible for solid angle determination. The knowledge of the absolute x-ray detection efficiency depends crucially on the x-ray energy regime of relevance. Typically, for our experiments, the x-ray detection efficiencies are measured by using absolutely calibrated, mixed γ sources, containing γ lines from ^{57}Co, ^{60}Co, ^{241}Am, ^{133}Ba, and ^{169}Yb, where the individual line strengths are known within an absolute accuracy of about 5%. Such calibration sources are well suited for the efficiency determination at energies in the range between 80 keV and 1.5 MeV. For the particular case of planar Ge(i) detectors with thickness in the range between 12 and 15 mm and x-ray energies below 200 keV, the detection efficiency is, in general, close to 50%.

The exact value and its related uncertainty depend on the particular x-ray energy and detector used. Finally, for particle detection a systematic error can be introduced by scintillator darkening. It is related to physical damage of the scintillator

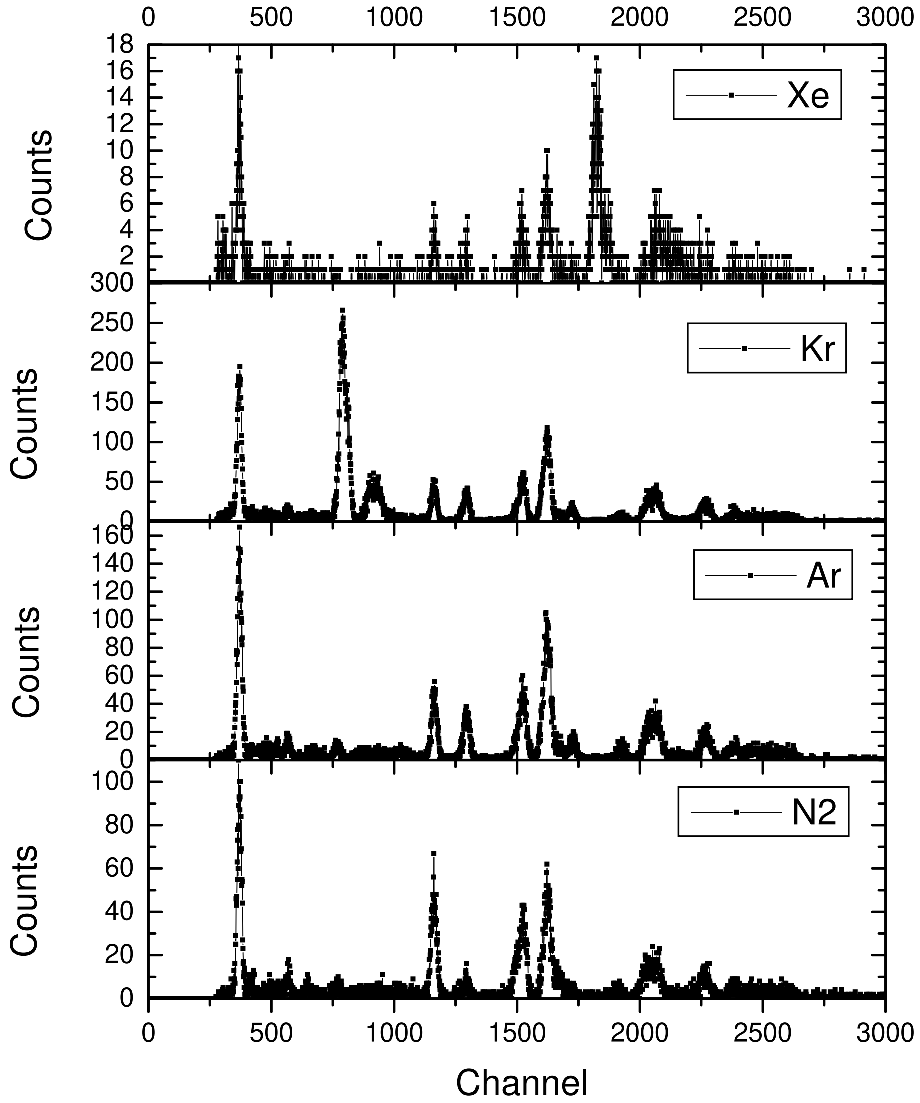

Figure 5.3: X-ray spectra corresponding to characteristic Balmer lines detected at 48° for all targets (see text).

material at the location of the beam spot, which results in a reduction of the signal amplitudes and may therefore lead to efficiency losses. If, however, the total electron-capture rate is normalized to the number of x-ray events associated with electron capture, i.e. measured in coincidence with the particle detector, this uncertainty cancels out.

The emitted X-rays were recorded in coincidence with the down-charged Li-like U^{89+} ions. Figure 5.3 shows examples of x-ray spectra recorded by the detector at 48° in coincidence with down-charged U^{89+} ions for U^{90+} on gaseous targets. The spectra only show x-ray radiation corresponding to the characteristic Balmer lines. The random contributions were subtracted from the true coincident x-ray spectra in all cases. As the target varies from light to heavy atoms, the relative intensities of Balmer lines exhibit a strong change. These features reveal the relative population of different *nlj* sublevels.

5.2.3 Cascade calculations and spectra simulation

In the simulation of the X-ray spectra, all projectile states up to $n = 40$ ($0 \leq l \leq 3$) were taken into account in order to describe the high energy part of the spectra where transitions from Rydberg levels are located. The cascade decay of the excited states were obtained by adopting the transition rates calculated from multi-configuration Dirac-Fock code GRASP, (General-purpose Relativistic Atomic Structure Program), based on the Racah Algebra and finite-difference methods [99]. The program uses a "fully relativistic approach". Multiconfiguration self-consistent-field calculations are based on the Dirac-Coulomb Hamiltonian - at this level the nuclei are considered stationary and may be modeled either as point sources or as spherically-symmetric extended sources; in the latter case the radial variation has the form of the Fermi distribution function. The transition rates are obtained for all n, l, j sublevels considered, to all n', l', j' energetically inferior sublevels. The energy levels of the Li-like ions are calculated for the cascade simulation, from the Dirac equation; to these solutions the screening corrections, due to the 1s shell which is completely filled, and QED corrections were made. To a value calculated by formula (1.37) for a Rydberg state ($9p_{3/2}$), where the Dirac solution is considered to be applicable, the transition energies calculated by Fritzsche, which include the screening corrections, were subtracted in order to obtain the lower energy levels. Moreover, the QED contributions which are calculated for the L-shell, i.e. for $2s_{1/2}$, $2p_{1/2}$, $2p_{3/2}$, were extrapolated, considering the $1/n^3$ scaling law for all s and p states, up to $n = 8$. It should be noted that the inclusion of QED part in energy levels is necessary to reproduce the exact position of the transition lines in comparison with the experimental spectrum.

The importance of including the QED corrections is shown in Fig. 5.4 where the simulation was done for $n = 12$ and without QED corrections, apparently the higher energy part is missing, and the simulated lines do not well coincide with experimental ones. For all the other sublevels, no QED corrections were made. The correction to $8s_{1/2}$, $8p_{1/2}$ and $8p_{3/2}$ are 1.014, 0.14 and 0.125 eV, respectively, and for $3p_{3/2}$, 2.37 eV, which shows that for higher n and/or for higher angular momenta the QED corrections can be safely neglected. Using this calculated values of the binding energies, a program is involved to compute all possible transition energies, which delivers the necessary input for the cascade simulation program.

The theoretical spectrum is obtained from the output of the cascade simulation code, which gives for each channel (i.e. energy) the theoretical number of counts. The total decay rate of a specific sublevel (nlj) can be defined as :

$$R_{nlj} = \sum_{E_{n'l'j'} < E_{nlj}} r_{nlj,n'l'j'} \tag{5.26}$$

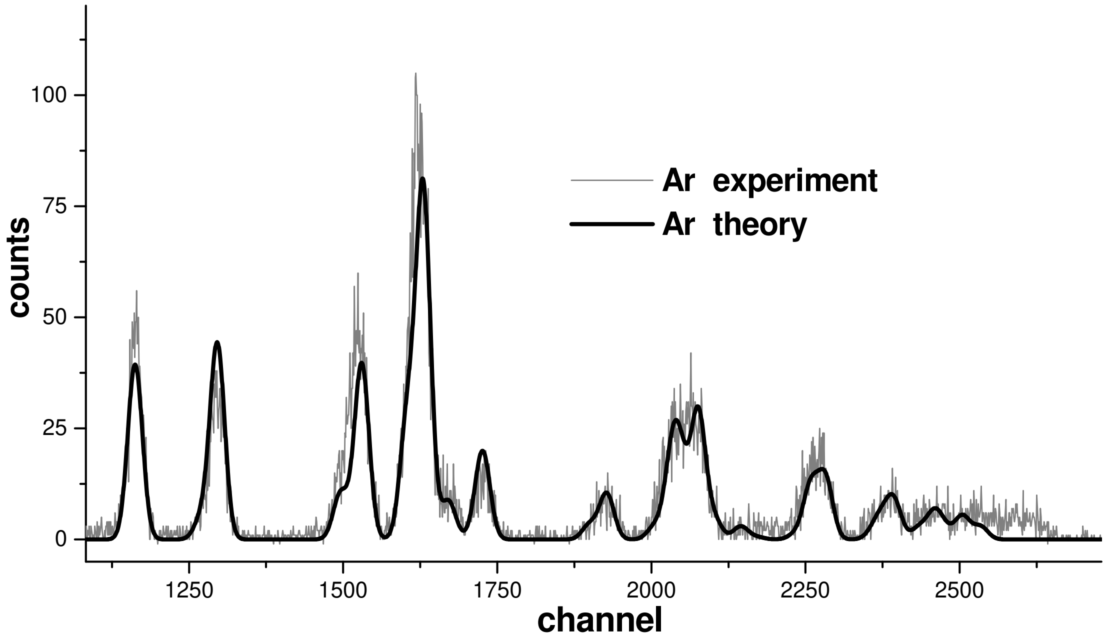

Figure 5.4: Comparison between experimental and theoretical spectra - the QED corrections are not included and the cross sections are calculated up to n=12.

where $r_{nlj,n'l'j'}$ is the decay rate from the level (nlj) to the level $n'l'j'$, the sum being performed over all states $(n'l'j')$, inferior energetically to the (nlj) state.
The branching ratio is then, for a fixed inferior state to which the transition takes place, $(n"l"j")$:

$$BR_{nlj,n"l"j"} = \frac{r_{nlj,n"l"j"}}{R_{nlj}} = I_{NM} \tag{5.27}$$

where I_{NM} are matrix elements defining the relative intensity of the line corresponding to the transition from the state $'N'$, which depicts the state (nlj) to the state $'M'$, which depicts the state $(n"l"j")$.
The total cross section, defined by (5.25), can be written as $\sigma_{nlj}^{tot} = \sigma_{NN}$, obtaining in this way a diagonal matrix, $\tilde{\sigma}$. If we consider all the possible combinations of states between which these transitions can take place, adopting a convenient indexing for the various (nlj) states, we obtain the matrix of all intensities I_{MN}, $\tilde{I}$, where $I_{MN} = 0$, any $M \geq N$, and we can further define the number of counts corresponding to each transition $N \rightarrow M$:

$$\tilde{C} = N_0 \tilde{I} \cdot \tilde{\sigma} \tag{5.28}$$

Equation (5.28) is correct if one considers that the decay of all levels occurs (more or less) instantaneously if compared with the length of the target. The simulation takes into account also the fact that each level, apart from electron capture from the target, is also 'fed' from the higher levels, so the population of the level changes continuously. The factor which multiplies then the branching ratio (or the intensity) in (5.28) is not anymore the total cross section, but the occupation of the level.

Finally, the spectrum is a sum of all contributions to the transition lines, at all transition energies, taking into account the gaussian distribution of the counts in the transition lines:

$$S(\chi) = \sum_n \sum_m C_{nm} \exp\left(-\frac{4\ln^2(\chi - \chi_{mn})^2}{\delta\chi^2}\right) \tag{5.29}$$

where χ represents the channel and $\delta\chi$ is the FWHM (full width at half maximum) of the line.

5.2.4 Results and comparison with experiment

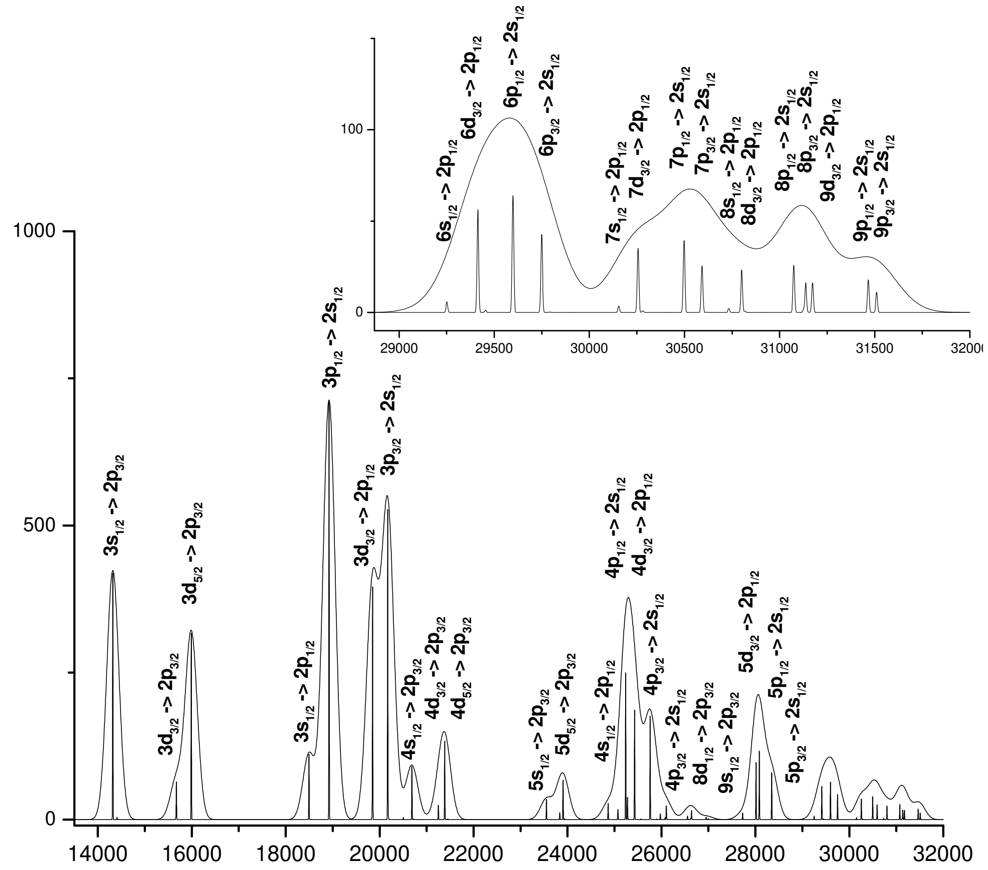

Figure 5.5: Theoretical spectra and identification of the lines. Transitions up to n=9, where n is the principal quantum number are considered and identified using the known values of the allowed transitions. Here it can be seen the contribution of the fine-structure components to different lines .

The theoretical spectrum is shown in figure 5.5. Here the x-position of the line, i.e. the energy, was compared with the known values of the allowed transitions, up to n=9, all the significant lines being identified and reproduced in the spectrum.

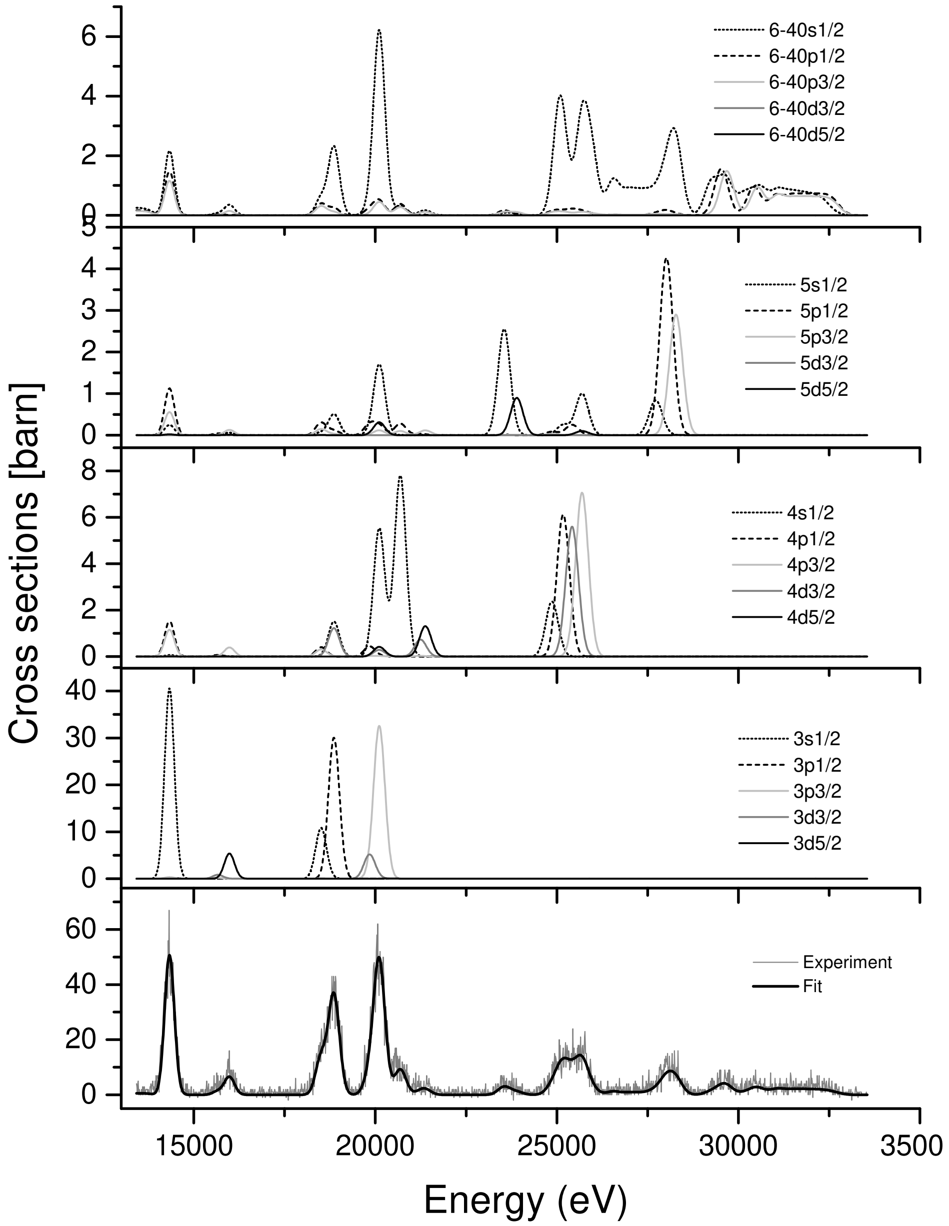

Figure 5.6: Lithium-like uranium x-ray spectrum for collision with N_2 target - experimental data is compared with the theoretical fit - bottom spectrum, and separate contributions from capture into individual subshells calculated with the cascade simulations program are depicted in the top spectra.

This identification gives information about the way in which the decay of the electrons from each excited level contributes to the total x-ray spectra, either directly after capture, to the L-shell, or cascading through other intermediate excited levels. However, the results of the comparison with the experiment were not satisfactory, most probably the theories failed to describe correctly the cross sections of the capture process. In order to overcome this and to evaluate the relative populations of different j-sublevels in the collisions, in the simulation program the cross sections for electron capture (via REC and NRC) were set to 1 for each (n, l, j) subshell up to $n = 5$, $l = 0, 1, 2$ and for all subshells with $6 \leq n \leq 40$ with different l and j's.

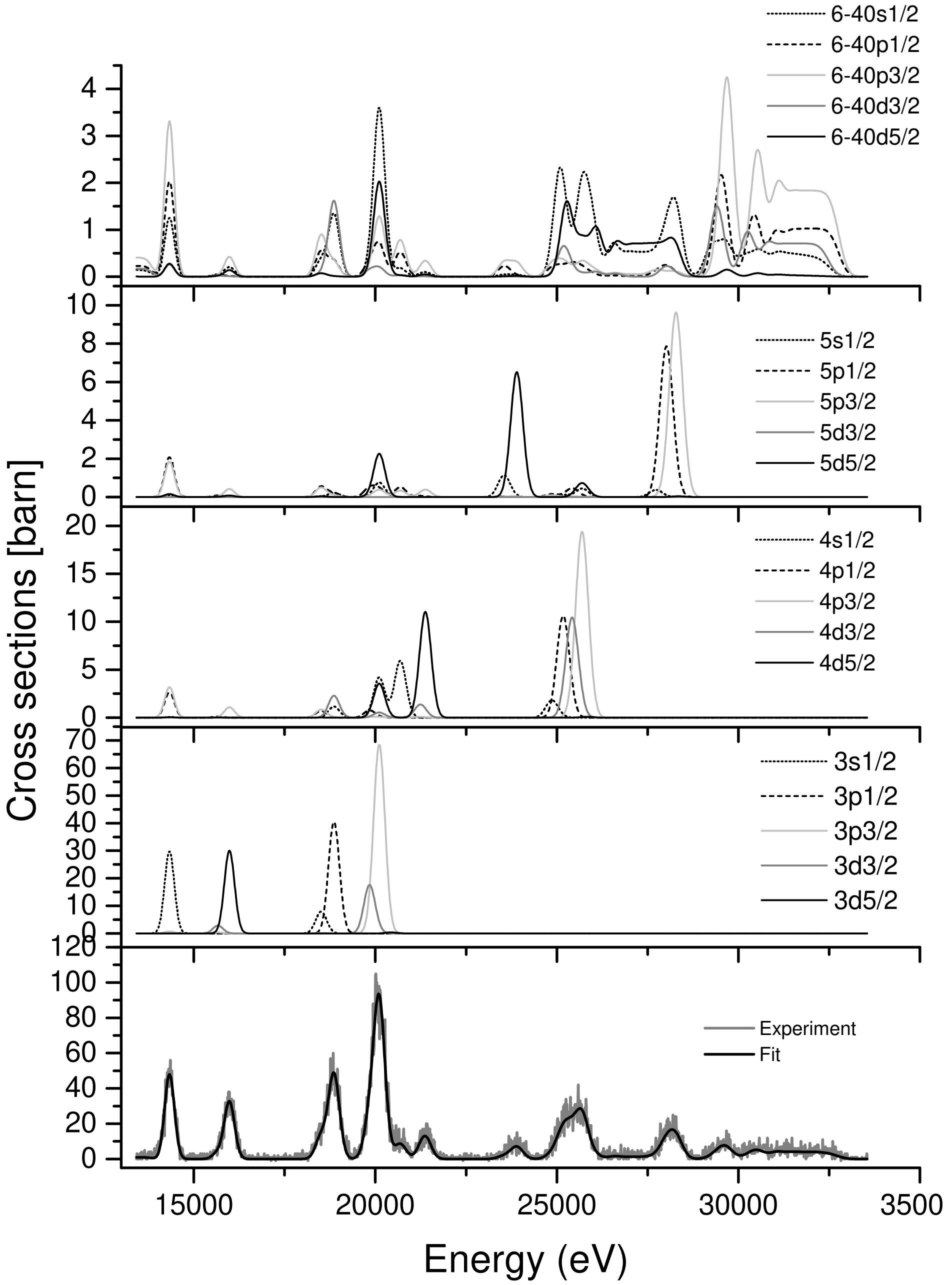

Figure 5.7: The same like Fig. 5.6, but for argon target.

The individual spectra obtained were multiplied by an amplitude that was used as a fit parameter, after these spectra were summed up, in the fitting to the experimental ones. The fitting was based on a Minuit program [100]. Minuit is a software from CERN program library, a tool to find the minimum value of a multiparameter function and analyze the shape of this function around the minimum, taking into account the error functions (χ^2) in order to complete the best fit parameter values and uncertainties.

In Fig. 5.6, the experimental Balmer spectrum of Li-like Uranium recorded for 223 MeV/u U^{90+} ion on N_2 collisions is depicted in comparison with the result of the applied fitting procedure. In addition, the lines from capture into different projectile subshells are represented in the upper spectra to show the relative contributions to the total Balmer spectrum. For this purpose, the spectra of each individual shell is drawn separately. In the bottom spectrum, the contributions from all upper levels are summed.

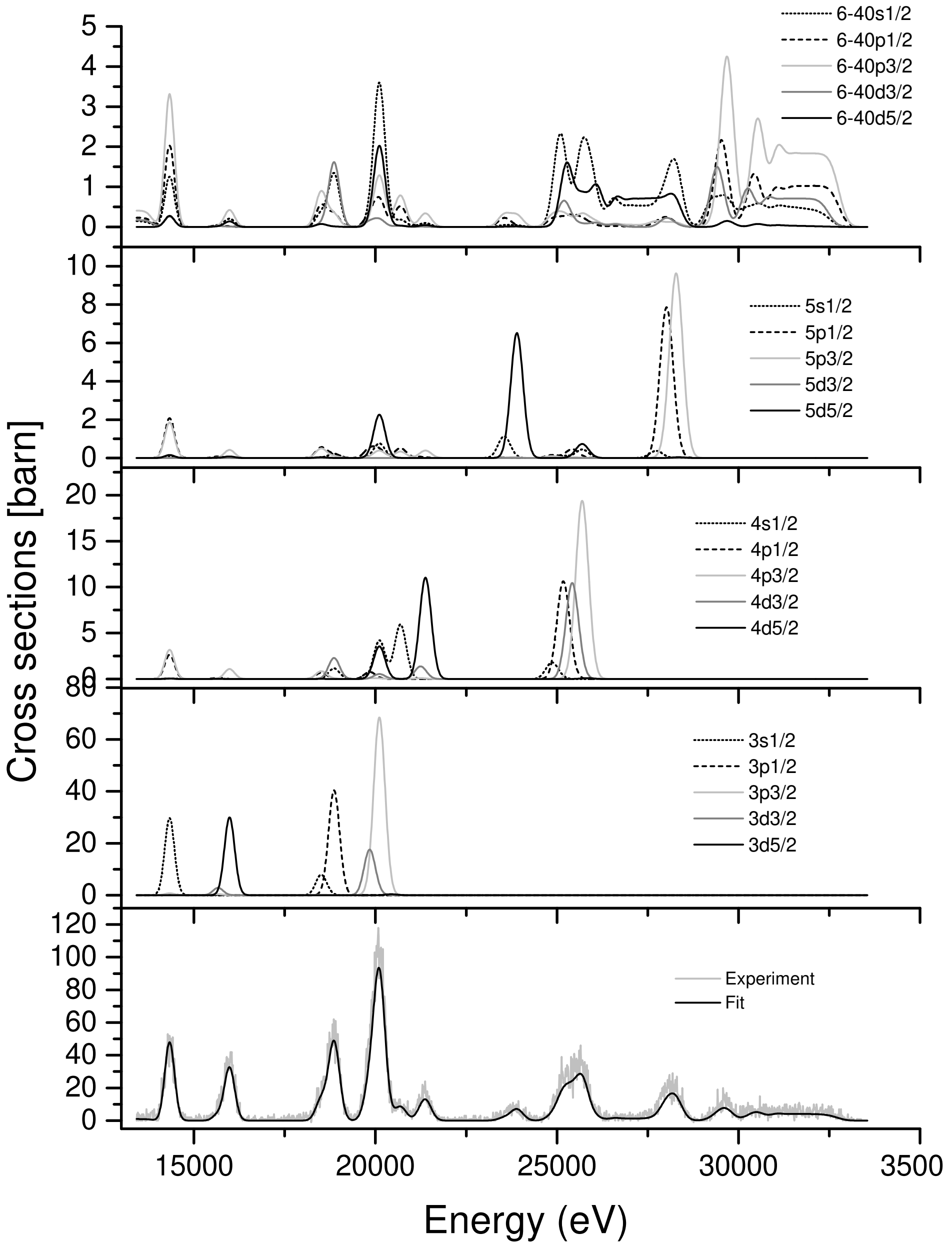

Figure 5.8: The same like Fig. 5.7 for krypton target.

From these spectra, and the ones for Argon and Krypton as well, comparing the contributions from prompt decays from the excited states to the n=2 state (ground state) with the contributions to the same lines via cascade from states above, one can state that the prompt decay dominate the Balmer spectra and that the cascade transitions are much less significant (e.g. see Fig. 5.7, the contribution to the first line ($3s_{1/2}$-$2p_{3/2}$) from direct capture into $3s_{1/2}$ and prompt decay to $2p_{3/2}$ compared with the ones from n=4, 5, 6-40).

From the fitting results, the relative populations of different j-sublevels can be calculated. The fitting parameter i.e. the cross section for capture into individual nlj subshells are compared with the theoretical results for capture, see Fig. 5.9.

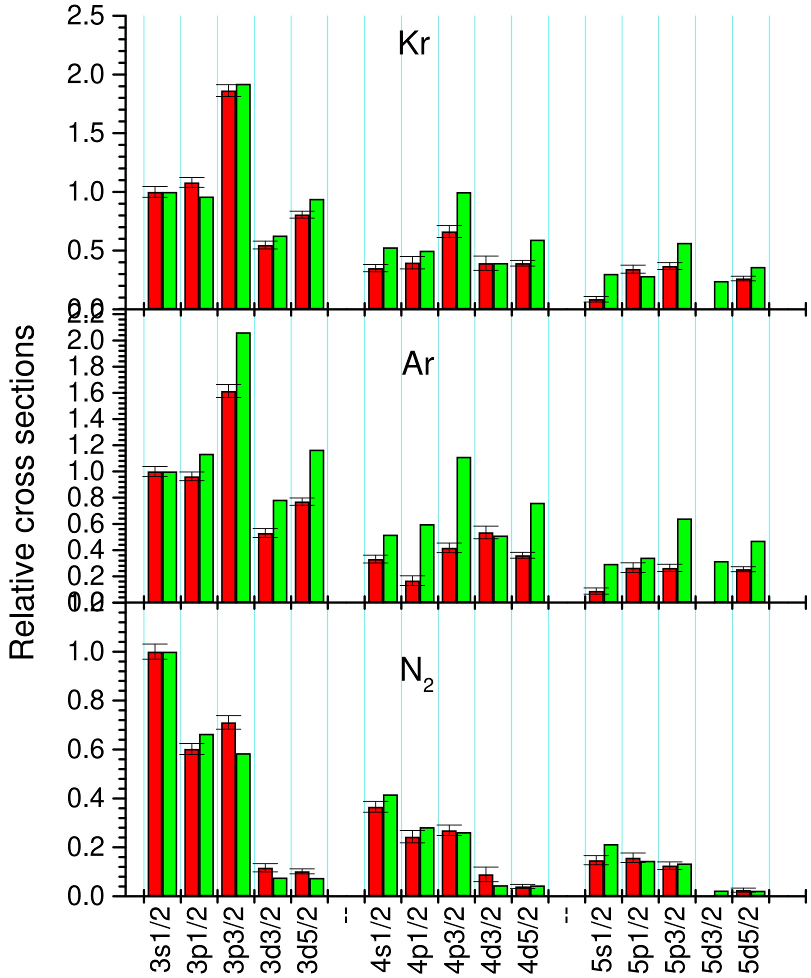

Figure 5.9: Relative populations for nlj subshells, for N_2, Ar and Kr. The cross sections are normalized to the capture into $3s_{1/2}$ cross section for each target.

The relative populations for the nl subshells are depicted in Fig. 5.10, for three targets. For the n-states, the cross sections are shown in Fig. 5.11, and compared with the theoretical cross sections.

For the nitrogen target, an excellent agreement between theory and experiment can be seen. For a light target as N_2, the REC process is predominant. From Fig. 5.1, it can be seen that the REC cross sections are with approximately a factor of 10 bigger than the NRC ones.

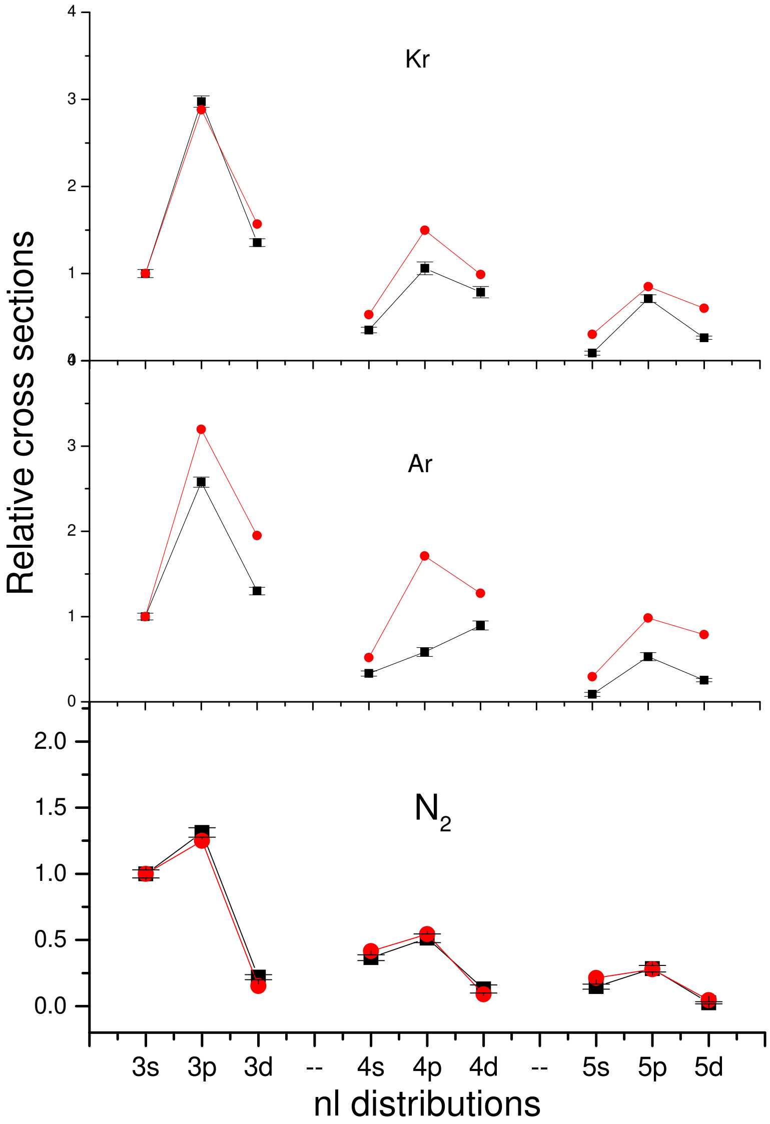

Figure 5.10: Relative populations for the nl subshells for capture into U^{90+} from N_2, Ar and Kr targets, normalized to the cross section for capture into the $3s_{1/2}$ shell for each target, respectively.

The difference between our case and the theoretical line presented in Fig. 5.1 is that there the nonrelativistic dipole approximation and the eikonal theory were used for the calculations of REC and NRC cross sections, respectively. However for REC there is a good agreement, especially for total cross sections, to both experimental data and complete relativistic calculations. Consequently we can regard this difference between the cross sections for both capture processes as being true also in our case, where the exact relativistic calculations were used.

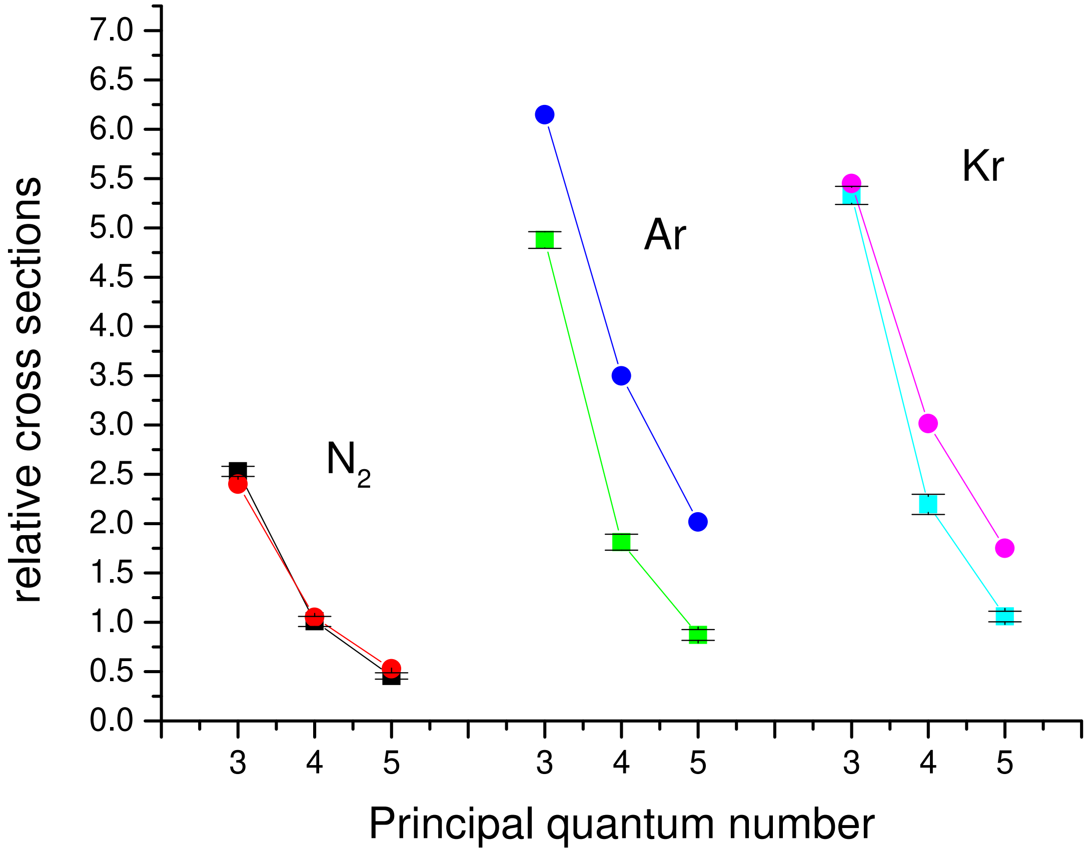

Figure 5.11: Comparison between theory and experimental population cross sections for three targets, normalized to the cross section for capture from N_2 into the n=4 shell of U^{90+}, as function of the principal quantum number n.

Here, even the theoretical line was obtained by using the nonrelativistic dipole approximation, in general there is a good agreement, especially for total cross sections, to both experimental data and complete relativistic calculations, so we can regard this difference between the two capture processes as being true also in our case, where the exact relativistic calculations were used. This proves once more that this latter approach describes extremely well the REC process and predicts with accuracy the j-subshell dependence of the cross section. Here also, the scaling law ($1/n^3$) proves that it can be safely applied. The results show that the capture mainly populates the s and p states, where the $s_{1/2}$ are more favored, as it is already predicted by the REC theory.

For argon the deviations are the largest, even compared with the krypton target. The theoretical state selective cross sections are not only bigger than the experimental ones, but also the statistical weights (formula 5.23 for NRC) within one n,l shell used in the calculations, show a different behaviour from the experimental ones. In the case of argon, at this projectile energy, the roles of the two competing capture processes are inversed compared to the case of N_2. The NRC process is dominant, and the CDW theory may fail to predict correctly the capture process. If the REC and CDW predict correctly the n, l, j distribution of the cross sections, but there are discrepancies in the absolute (total) values in comparison with the experimental values, even if the CDW cross sections are of an order of magnitude smaller than the REC ones, this is still a sufficient reason that in the addition of the two values, as we do in Fig.5.9, the j-sensitive behaviour gets destroyed and this sublevel prediction fails to describe.

For the heavier target, krypton, where the NRC is the main process (see Fig. 5.1, the discrepancies are again large, but smaller than for argon. The relative weights within the n,l subshells are not correct in this case also. However there is a better agreement in the j-sensitive populations - this is in favor of our last consideration, here NRC being from far (several orders of magnitude) dominant, and the CDW results being here the main contribution - the sublevels prediction should get better, which actually happens. Also for this heavy target, the l-distribution within a fixed n-shell (Fig. 5.10) shows an overall better agreement with data. Generally, the l-distribution within the shells for all targets shows the same dependence of the angular momentum quantum number (higher for l=1) and reproduces well the shape given by experimental data, even if the total values are different. For both heavier targets, the n-dependence of the population (Fig. 5.11) shows also the same general behaviour with increasing n as the measured populations. This can be seen also in a comparison between all the three targets.

Here, the comparison is given only for n = 3, 4, 5, however these are the shells that contribute mostly to the spectra. These investigations may be compared with other theoretical approaches used to describe the measured data, in different experiments [82]. In this case, where the dipole approximation was used for REC and the relativistic eikonal approximation for NRC, it can be seen that this last theory is found to give a good description of the experimental data, especially for low energies and low-Z targets.

However, for the heavy targets, this approach proves also to deviate significantly (within a factor of 2) from the experimental result. The CDW theory is a non-relativistic theory - at this energy of 223 MeV/u, one might expect that complete relativistic calculations would be able to describe much better the experimental measurements.

To summarize, the novelty of this calculations originates from the j-sensitivity of this study of the charge exchange process. This kind of calculations were not performed up to now. An overall good agreement is found between the experimental data and the applied theoretical approaches with the exceptions mentioned. Consequently, these results support the reliability of the two theories used for calculating the cross sections for electron capture into high-Z ions as long as the nuclear charge of the target involved in the collisions is not too large. However for higher nuclear charge of the target, the non-relativistic CDW theory shows deviations from the experimental data which indicate the need for a better theoretical treatment. Still this investigations prove to be a powerful tool in the analysis of x-ray spectra produced by highly charged heavy-ions in collisions with matter.

5.3 Application of the cascade simulation program: formation of excited states in high-Z He-like systems

High-Z helium-like ions represent the simplest multi-electron systems for studying the interaction between electron-electron correlations, relativistic and quantum electrodynamical (QED) effects in strong fields. However, in contrast to the lithium-like ions, almost no experimental information is available about the excited states in the high-Z domain of the helium sequence. In the following, a theoretical analysis of the x-ray production and decay dynamics of the excited states in helium-like uranium will be presented.

Until now, few studies were performed concerning the fine structure and the properties of highly charged He-like ions. For the neighboring hydrogen- and lithium-like ions a large number of precise measurements were effectuated ([101, 102]). Still, for the He-like high-Z ions, neither the fine structure, nor the excitation cross sections nor line densities are precisely known. Accurate results have been obtained only up to Z = 36. For higher Z, the individual K_α and K_β transitions have not been resolved in experiments, up to now [103]. So far, just one experiment on the Lamb-shift in helium-like uranium has been carried out by Munger and Gould [104], in which a lifetime measurement of the $^3P_0$ level has been exploited in order to derive the $^3P_0 -^3 S_1$ fine structure splitting. From a lifetime of 54.4 ± 3.4 ps, they obtained a $^3P_0 -^3 S_1$ transition energy of 260.0 eV with a precision of about 8 eV and, thus, could receive a first clue about QED contributions for helium-like uranium. Due to a relative uncertainty of about 7 %, however, all details concerning the fine-structure of these ions still remain uncertain.

For high-Z ions in the helium sequence, the $\Delta n = 0$ transitions in the $L-$shell are of particular interest because they are affected not only by the relativistic interaction among the electrons but also by rather strong QED effects. These transitions, therefore, are an ideal test ground for the understanding of this interplay between electron-electron correlations, relativistic, as well as QED effects in many-particle systems. Fig. 5.12 shows the schematic level structure and decay branches for the $n = 2$ levels in high-Z ions. Interesting for QED studies are the $1s2p\,^3P_0 - 1s2s\,^3S_1$ ($\Delta E \approx 253$ eV in U^{90+}) and the $1s2p\ ^3P_2 - 1s2s\ ^3S_1$ ($\Delta E \approx 4.51$ keV in U^{90+}) transitions for which precise measurements are required in order to determine the level scheme in the high-Z range. The theoretical calculations on these transitions that have been carried out [105, 106, 107] show deviations of a few eV, i.e. rather large if compared with the current precision for the excited states in high-Z hydrogen- and lithium-like ions. These deviations are mainly a result of the different treatment of the electron-electron interaction. However, a direct comparison of the individual theoretical results can not replace accurate measurements of the fine structure and lifetimes for high-Z helium-like ions [108, 109].

Precise energy measurements of the $\Delta n = 0$ transitions in high-Z helium-like ions have not been possible up to now due to the lack of luminosity. However, an alternative access to the fine structure of helium-like ions is provided by the long living, metastable $1s2p\ ^3P_0$ level. For this level, a precise lifetime measurement would enable one not just to collect information about the fine structure splitting of the

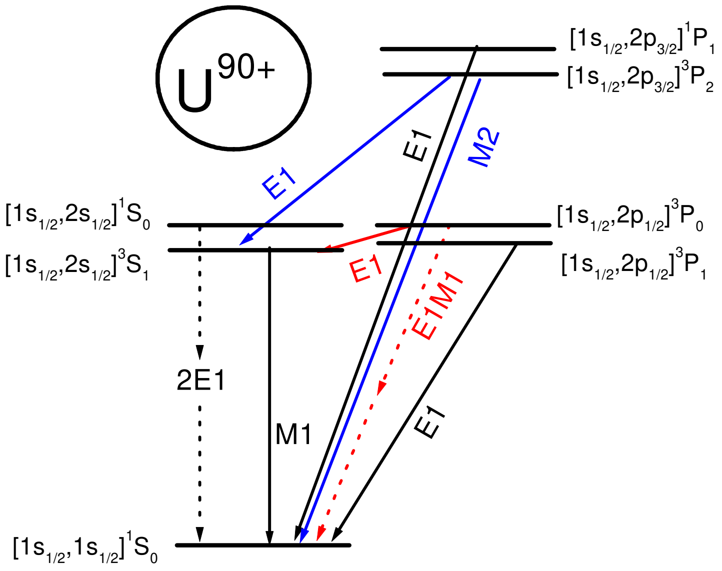

Figure 5.12: Schematic level structure and decay branches for the $n = 2$ levels in high–Z helium-like uranium. The $^3P_0$ states decay either via an 253 eV $E1$ or $E1M1$ transitions with decay rates of $1.2 \cdot 10^{10}$ sec^{-1} and $5.6 \cdot 10^9$ sec^{-1}, respectively. The $^3P_2$ states decay via 4510 eV $E1$ transitions into $^3S_1$ or $M2$ transitions into the ground state with decay rates of $8.6 \cdot 10^{13}$ sec^{-1} respectively $2.1 \cdot 10^{14}$ sec^{-1}.

$1s2s\ ^3S_1$ and $1s2p\ ^3P_0$ levels but would also improve our knowledge of the atomic wave functions, for calculating accurate transition probabilities. As seen from Fig. 5.12 , the $1s2p\ ^3P_0$ level decays either by E1 transitions to $1s2s\ ^3S_1$ or by a two-photon E1M1 emission into the $1s^2\ ^1S_0$ ground state. The rates for both channels are comparable in magnitude. Here, a direct lifetime measurement of the $^3P_0$ level can be done using the $1s2s\ ^3S_1 - 1s^2\ ^1S_0$ M1 transition whose decay rate is more than four orders of magnitude faster than the precursory decay of $1s2p\ ^3P_0$ level.

In the following, the conditions to determine lifetimes for the $1s2p\ ^3P_0$ level are investigated and discussed, as well as a direct energy measurement of the $1s2p\ ^3P_2 \rightarrow 1s2s\ ^1S_1$ transition in high-Z helium-like ions (like U^{90+}) is accomplished by using electron capture into the hydrogen-like ions [111].

5.3.1 Decay dynamics and x-ray production

To simulate the projectile x–ray production which is induced by electron capture, the two relevant capture processes are, as mentioned before, non-radiative and radiative capture. Generally, both capture processes have to be considered in order to obtain the initial population distribution at either a gaseous target or at the foil. While a continuum distorted-wave (CDW) approach has been applied to the non-radiative capture as in the previous chapter, the $(nlj)-$dependent cross sections for a radiative capture were calculated within the dipole-approximation (see chapter 2, and Ref. [94]). For the cases of initially bare and helium-like uranium, these assumptions have recently lead to an excellent agreement between experimental and simulated x-ray spectra for a wide range of energies from 49 MeV/u to 350 MeV/u [94].

For the prompt capture of electrons inside the foil, the same approximations as for bare ions can be applied also for hydrogen-like ions since an electron capture occurs for high-Z ions predominantly into highly-excited subshells, rather independent of the additional $1s$ electron. After the capture, the excited ions stabilize themselves by a cascade of radiative transitions, whose decay dynamic is well described by a system of rate equations

$$\frac{dN_i}{dt} \;=\; - \sum_{j}^{(<)} \lambda_{ij}\, N_i \;+\; \sum_{k}^{(>)} \lambda_{ki}\, N_k \qquad\qquad \forall\, i = 1, \ldots, \Lambda\,. \tag{5.30}$$

In these equations, Λ is the total number of (excited) levels which are considered in the decay cascade; the index j runs over all levels with total energy $E_j < E_i$ and k over all those with $E_k > E_i$. Moreover, apart from its exponential decay into lower-lying levels, each level will also be 'fed' from levels having higher energies.

Most of the excited levels have a rather large number of decay branches and at least one fast E1 branch ($\approx 10^{14}$ sec^{-1}). Only $1s2p\ ^3P_0$ level is metastable $\Gamma \approx 10^{10}$ sec^{-1} for high-Z helium-like ions. For simulating the time evolution of Eq.(5.30) for electron capture in a foil, only the states with total angular momenta $J \leq 3$ and principal quantum numbers $n \leq 9$ were considered. This choice was made considering that due to the big density of particles in the solid, the highly excited states are mainly depopulated. The restriction $J \leq 3$ and $n \leq 9$ leads to a total of 121 excited levels which were taken into account in the time evolution of Eq. (5.30). For the individual decay branches, moreover, all multipole components of the radiation field up to the magnetic-dipole ($M2$) and electric-octupole ($E3$) modes were included. This results in a total of 5149 decay channels which have been considered. All transition energies and decay rates have been generated from (configuration-averaged) wave functions of the GRASP-92 program [112]. For optimizing the wave functions, several groups of levels have been considered together and the main relaxation effects included by applying a newly developed transition probability code [113].

For integrating the rate equations (5.30), time slices of $10^{-17}s$ have been used; they are by a factor of 3 smaller than the fastest decay rate of the $1s2p\ ^1P_1 - 1s^2\ ^1S_0$ transition and will therefore provide a 'smooth' evolution of the level occupation of the high-Z ions. As a result of the simulation, Fig. 5.13 depicts the population probability of the $^3P_0$ level for helium-like uranium as function of time (t) in the emitter frame (upper x-axis). In this figure, a carbon target and a collision energy of 200 MeV/u were assumed [111]. The lower x-axis refers to the distance $d = \gamma \cdot \beta \cdot c \cdot t$ of the ion from the foil. Note, that at $t = 0$ the population of the $^3P_0$ level by direct capture is rather small and amounts to about $\sigma = 200$ barn (not shown in the figure). However, owing to the feeding from higher-lying levels, the population probability increases for this level by more than a factor of five and reaches a saturation after 5×10^{-13}sec. But only after about 5×10^{-10}sec, which corresponds to a distance of about 2 mm from the foil, no additional feeding of the $^3P_0$ level arises and the population of this particular level then approaches an exponential decay behaviour. For an energy of 200 MeV/u, consequently, distances of closer than 2 mm must be avoided in any experiment in order to guarantee a

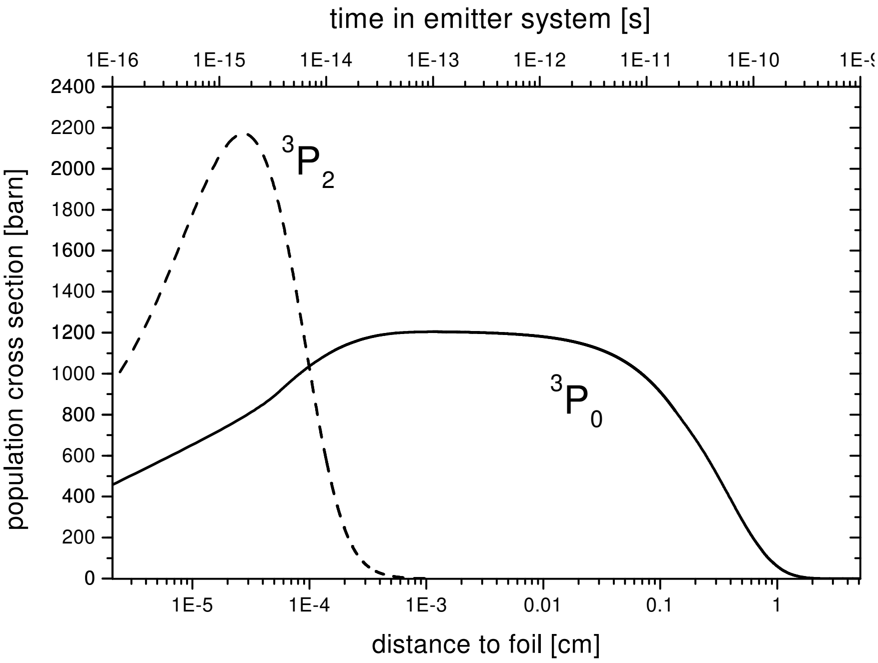

Figure 5.13: Occupation of the $^3P_0$ and the $^3P_2$ levels in helium–like uranium as a function of the time or, equivalently, their distance from the foil (see text). An initial electron capture has been assumed for 200 MeV/u hydrogen-like ions in the foil.

correct lifetime measurement. For comparison, in Fig. 5.13 is presented the time evolution of the $^3P_2$ level ($\Gamma \approx 10^{14}$sec^{-1}) which shows that at such distances all the other L-shell levels are completely depopulated.

Apart from the population of excited states by electron capture inside a foil, the use of a jet-target as the one available at the storage ring ESR is also of interest. Owing to its length of 5 mm, however, this target is not appropriate for a lifetime measurement; still, it may be useful in precise measurements of the $^3P_2 -^3 S_1$ level splitting. Apart from the geometry, the main difference between the jet and a solid target concerns the particle densities. In a solid, the density ρ is typically of the order of 10^{23} p/cm^3 while the jet-target has a density of only about 10^{12} p/cm^3. Thus, no density effects as discussed above for the excitation at a foil need to be taken into account at the jet-target. For a jet-target, in fact, a capture of electrons has been observed even into subshells with $n \approx 20$ at the ESR [94]. In order to estimate the strength of the $^3P_2 -^3 S_1$ x-ray line for U^{90+}, a spectrum simulation is made for the collision system $U^{91+} \rightarrow N_2$ at 100 MeV/u for which all levels up to n=20 have been incorporated in the rate equations (5.30). Such an elaborate computation leads to a total of 435 levels and involves more than 42000 individual transition channels.

We take into account the assumption made before, that using a jet target, the decay of all levels occurs almost instantaneously if compared with the length of the target. Apart from the $^3P_0$ level which has no influence on the time evolution of the upper $^3P_2$ level, this assumption has been well confirmed by the calculations. In Fig. 5.14,

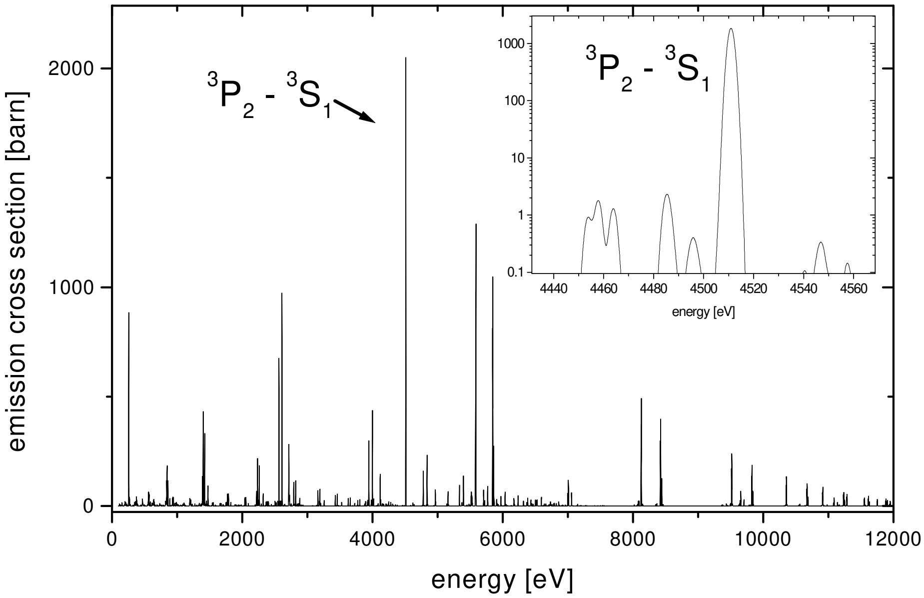

Figure 5.14: Simulated x-ray spectra of U^{90+} ions. Here, the excited states are formed by electron capture from a N_2 jet-target in collision with U^{91+} ions at 100 MeV/u. For the calculation, excited levels up to n =20 have been taken into account.

the result of a simulated x-ray spectrum is depicted by assuming an experimental resolution of 3 eV. The energy range of this theoretical spectrum covers all transitions below 13 keV, i.e. all those transitions involving the M and higher shells as well as the inter L-shell transitions. Most remarkably, the $^3P_2 -^3 S_1$ x-ray line turns out to be the most intensive transition in this energy range. The calculated total production cross-section amounts to about 2 Kbarn. Note, moreover, that no line blends should disturb a precise measurement as could be caused by higher Rydberg transitions (compare inset in Fig. 5.14).

5.3.2 Summary and Conclusions

A theoretical study of the x-ray production and decay dynamics of the excited states in helium-like uranium were discussed for the case of U^{91+} ions in collision with solid and gaseous matter. For the $^3P_0$ level, this theoretical analysis allows the understanding of the feeding and cascade population as function of the distance from the foil. This provides the necessary information for a precise lifetime measurement in future experiments. Concerning the population of the $^3P_2$ level, the analysis predicts that this level can be populated very efficient at the ESR jet target. For this level, no line blends have been found from Rydberg transitions. A precise lifetime experiment as well as energy determination of the $^3P_2 -^3 S_1$ transition will constitute a unique probe of our current understanding of the simplest multi-electron systems in the high-Z domain, a test which has been missing till today.

Conclusions and Outlook

The investigations done within this PhD work cover the x-ray production processes in the collisions of highly-charged heavy ions with matter. These processes are discussed here from the point of view of the two fundamental aspects that have to be taken in consideration in the field of atomic physics with highly charged ions : the collisional and the atomic structure aspects are essentially linked and have to be studied together for a better understanding of fundamental processes like photoionization, electron capture and radiative transitions.

The brilliant beams of highly charged and cooled ions that are available at the ESR storage ring opened an unique insight in fundamental domains of atomic physics that were not accessible up to now. Almost all ion species can be accumulated, stored and electron cooled. This cooling technique guarantees for brilliant high intensity beams, with precisely known energies, charge state, momentum spread and beam diameters close to 1 mm. Along with the internal gas jet available at the ESR, where thin gaseous targets from H_2 up to Xe can be used, the interaction of these beams with matter can be studied under single-collision condition. The experimental conditions are almost free of background noise. The deceleration capability of the storage ring which allows one to investigate the dynamics in ion-atom collisions over a wide range of energies.

Recombination is an important process that can be studied either at the ESR electron cooler, case of free electrons, or in collisions with light targets where the RR can be considered as a good approximation for radiative electron capture (REC). REC allows a direct and unambiguous experimental access to the study of photoionization. A code has been developed providing exact calculations for the radiative recombination cross sections within the nonrelativistic dipole approximation using the Stobbe approach without any other further approximation. These calculations can be performed fast, up to high Rydberg states, for any individual n, l shell. These results are needed in the case of recombination with the cooler electrons, where the capture into high Rydberg states might have a significant contribution to the total cross section due to the small relative velocity between ions and electrons. The capture in these high levels is also important for the study of the x-ray spectra of the radiative electron cascade to the ground state (see §4). Further comparison with other nonrelativistic theoretical approaches shows that they lead to the same results within very close limits.

The dipole approximation proves to be applicable in the low-energy regime even for high nuclear charges as $Z = 92$. However, in such extreme cases some expected differences arise with respect to the full relativistic formulation. In the case of Radiative Recombination rate coefficients, the calculations compared with other theoretical approaches lead to the same result within close limits. This check of validity of the dipole approximation at low energies but high-Z ions was not done up to now. On the other side, recent very precise data are available for both radiative and dielectronic recombination even for the heaviest bare ions [79].

In the case of very high-Z systems an exact theoretical treatment is highly required in order to describe the significant relativistic effects that appear. A sensitive gauge of these effects is the photoionisation angular distribution. The experimental results which are in good agreement with fully relativistic calculations show an unambiguous identification of spin-flip transitions occurring in relativistic ion-atom collisions. This finding emphasizes the importance of the REC process for the study of photoionization in the domain of high-Z few-electron ions. Most remarkably also in the case of decelerated ions both theory and experiment show a non-vanishing cross-section close to 0^o which proves that magnetic contributions are still present in the low-energy domain. These measurements allowed us to obtain for the very first time differential data for photoionization of a high-Z element in the low-energy regime. The results demonstrate that the applied method is a powerful tool for the study of photon matter interaction in regimes not accessible in direct photoionization experiments.

The fine structure and the properties of high-Z ions were investigated in the studies of X-ray spectra. By simulation of projectile X-ray production and comparison with experimental data, important information referring to electron capture into the high-Z projectile could be deduced, and hence could be used to test the related theories. The type of capture (non-radiative NRC and radiative REC) is proved to depend strongly on the target atomic number. Here, the first magnetic-substate dependent study of the x-ray was successfully performed in order to obtain precise nlj-selective information about electron transfer into high-Z projectiles and to reveal the importance of QED corrections for the binding energies and of Coulomb distortion effects by comparison with capture theories available. For light targets, where the REC process is dominant, an excellent agreement with relativistic theory was found. Discrepancies appear for heavier targets, where the NRC is the main capture process, either because the nonrelativistic CDW theory fails to describe the process, either the interplay of the two processes affects the population of the excited states. An overall good agreement is found between the experimental data and the applied theoretical approaches with the exceptions mentioned. Consequently, these results support the reliability of the two theories used for calculating the cross sections for electron capture into high-Z ions as long as the nuclear charge of the target involved in the collisions is not too large.

This type of theoretical analysis of the x-ray production and decay dynamics of excited states is also useful in the understanding of the feeding and cascade population. In summary, a theoretical study of the x-ray production and decay dynamics of the excited states in helium-like uranium is performed for the case of U^{91+} ions in collisions with solid and gaseous matter. It is shown that a precise lifetime experiment as well as an energy determination of the $^3P_2 - ^3S_1$ transition can constitute a unique probe of the current understanding of the simplest multi-electron systems in the high-Z domain, a test which has been missing till today.

Bibliography

[1] M. Stobbe, Ann. Phys. (Leipzig) **7**, 661 (1930).

[2] W. Gordon, Ann.Phys. (Leipzig) **2**, 1031 (1929)

[3] F. Sauter, Ann. Phys. (Leipzig) **11** (1931) 454.

[4] Th. Stöhlker, O. Brinzanescu,A. Krämer, T. Ludziejewski, X. Ma, P. Swiat, A. Warczak, GSI-Preprint-99-43, November 1999, submitted to x-Ray and Inner Shell Processes: 18^{th} International Conference.

[5] H. J. Kluge, Nucl. Inst. Meth. B **98**, 500 (1995).

[6] T. Andersen, L. H. Andersen, P. Balling, H. K. Haugen, P. Hvelpund, W.W. Smith, K. Taulbjerg, Phys. Rev. A, **47**, 890 (1993).

[7] H. Irnich, H. Geissel, F. Nolden, K. Beckert, F. Bosch, H. Eickhoff, B. Franzke, Y. Fujita, M. Hausmann, H. C. Jung, G. Kraus, O. Klepper, C. Kozhuharov, A. Magel, G. Münzenberg, F. Nickel, T. Radon, H. Reich, B. Schlitt, W. Schwab, K. Sümmerer, K. Suzuki, M. Steck, H. Wollnik, Phys. Rev. Lett **B 75**, 4182 (1995).

[8] R. C. Thompson, Meas. Sci. Technol. **1**, 93 (1990).

[9] E. Bodenstedt, *Experimente der Kernphysik und ihre Deutung, B.I.-Wissenschaftsverlag* (1979).

[10] R. H. Pratt, A. Ron, H. K. Tseng, Rev. Mod. Phys. **45** (1973) 273.

[11] H. Bethe and E. Salpeter, in Quantum Mechanics of One- and Two Electron Systems, edited by S. Fluumlgge, Handbuch der Physik Vol. 35 (Springer, Berlin, 1957).

[12] E. Spindler, *Untersuchung des strahlenden Elektroneneinfangs in Ion-Atom Stö βen*, Dissertation LMU München (1979).

[13] P. Zimmerer, N. Grün and W. Scheid, Phys. Lett. A **148**, (1990) 457.

[14] P. Zimmerer, N. Grun, W. Scheid, J. Phys. B: At. Mol. Opt. Phys. **24** (1991) 2633.

[15] T. Stöhlker, *Einfang quasifreier Elektronen in hochgeladene Schwerionen*, PhD Thesis, Universität Giessen, GSI-91-20, June 1991, ISSN 0171-4546.

[16] O. Uwira, A. Müller, J. Linkemann, T. Bartsch, C. Brandau, M. Schmitt, A. Wolf, D. Schwalm, R. Schuh, W. Zong, H. Lebius, W. G. Graham, J. Doefert, D. W. Savin, Hyperfine Interactions bf 108, 149 (1997).

[17] S. Schippers, Phys. Scripta **T80**, 158 (1999).

[18] A. Müller, in: H. F. Beyer, V. P. Shevelko (Eds.) Atomic Physics with Heavy Ions, Springer, Berlin 1999.

[19] A. Lampert, A. Wolf, D. Habs, J. Kenntner, G. Kilgus, D. Schwalm, M. s. Pindzola and N. R. Badnell, Phys. Rev. A **53**, 1413 (1996).

[20] H. Kossmann, N. schmidt and T. Andersen, Phys. Rev. Lett. **28** (1988) 1266.

[21] T. A. Carlson and M. O. Krause, Phys. Rev. A **158** (1967) 18.

[22] A. R. Sohval, J. P. Delvaille, K. Kalata, K. Kirby-Docken, and H. W. Schnopper, J. Phys. B **9** (1976) L25.

[23] H. Tawara, P. Richard, and K. Kawatsura, Phys. Rev. A, **26** (1982) 154.

[24] J. Eichler, Phys. Rev. A **32** (1985) 112.

[25] J. Eichler and H. Narumi, Z. Phys. A **295**, 209 (1980).

[26] L. J. Dubeaa and J. Eichler, J. Phys. B **18**, 2467 (1985).

[27] D. P. Dewangen and J. Eichler, J. Phys. B **18**, L65 (1985).

[28] J. Macek and S. Alston, Phys. Rev. A **26**, 250 (1982).

[29] C. M. Lee, L. Kissel, R. H. Pratt, H. K. Tseng, Phys. Rev. A **13** (1976) 1714

[30] Ćobić and M. V. Kurepa (eds.) *The Physics of Electronic and Atomic Collisions* Institute of Physics, Beograd (1973).

[31] R. Anholt *et al* Phys. Rev. A. **33** (1986) 2270.

[32] F. Folkmann, J. Borggreen and A. Kjeldgaard, Nucl. Instrum. Methods **119** (1974) 117; F. Folkmann, C. Gaarde, T. Huus and K. Kemp, Nucl. Instrum. Methods **116** (1974) 487.

[33] D. H. Jakubassa and M. Kelber, Z. Phys. A **273** (1975) 29.

[34] K. Ishii, K. Maeda, M. Takami,Y. Sasa,M. Uda and S. Morita Nucl. Instrum. Methods Phys. Res. A **75** (1993) 73.

[35] H. Tawara, T. Azuma, T. Ito, K. Komaki, Y. Yamazaki, T. Matsuo, T. Tonuma, K. Shima, A. Kitagawa and E. Takada Phys. Rev. A **55** (1997) 808.

[36] A H. Bethe and W. Heitler, Proc. R. Soc. A **146** (1934) 83.

[37] G. Elwert and E. Haug, Phys. Rev. **183** (1969) 90.

[38] H. K. Tseng and R. H. Pratt, Phys. Rev. A **3** (1971) 100.

[39] H. K. Tseng , R. H. Pratt and C. M. Lee, Phys. Rev. A **19** (1977) 187.

[40] U. Fano, K. W. McVoy, and J. R. Albers, Phys. Rev. **116**, 1147 (1959).

[41] L. R. Andersson and J. Burgdörfer, *The Physics of Electronic and Atomic Collisions* (AIP Conf. Proc. 1993 295) (New York: AIP) p. 595.

[42] A. Ichihara, T. Shirai and J. Eichler, Phys. Rev. A **49**, 1875 (1994).

[43] J. Eichler, A. Ichihara and T. Shirai, Phys. Rev. A **51**, 3027 (1995).

[44] Th. Stöhlker, C. Kozhuharov, P.H. Mokler, A. Warczak, F. Bosch, H. Geissel, R. Moshammer C. Scheidenberger, J. Eichler, A, Ichihara, T. Shirai, Z. Stachura, P. Rymuza, Phys. Rev. A. **51**, 2098 (1995); Th. Stöhlker, C. Kozhuharov, P.H. Mokler, A. Warczak, Comments At. Mol. Phys. **33**, 271 (1997).

[45] T. Ludziejewski, Th. Stöhlker, S. Keller, H. Beyer, F. Bosch, O. Brinzanescu, R. W. Dunford, B. Franzke, C. Kozhuharov, D. Liesen, A. E. Livingston, G. Menzel, J. Meier, P. H. Mokler, H. Reich, P. Rymuza, Z. Stachura, M. Steck , L. Stenner ,P. Swiat and A. Warczak, J. Phys. B: At. Mol. Opt. Phys. **31** (1998) 2601-2609.

[46] V. P. Shevelko, *Atoms and Their Spectroscopic Properties*, Springer Ser. Atom. Plas., Vol. 18 (Springer, Berlin, Heidelberg 1997).

[47] I. I. Sobelman, *Atomic Spectra and Radiative Transitions*, 2nd. edn., Springer Ser. Atom. Plas., Vol. 12 (Springer, Berlin, Heidelberg 1992).

[48] G. Kraft, *First Patient Treatment with Heavy Ions at GSI*, Proc. 6^{th} Europ. Part. Acc. Conf. (EPAC), Stockholm, (1998), p. 212.

[49] H. Geissel *et al.*, Nucl. Instr. Methods Phys. Res. B **70**, 286 (1992).

[50] K. Blasche and B. Franzke, *Status Report on SIS-ESR*, Proc. 6^{th} Europ. Part. Acc. Conference (EPAC), London, (World Scientific, Singapore, 1994), p. 133.

[51] B. Franzke, Nucl. Instr. Methods Phys. Res. B 24/25, 18 (1987).

[52] B. Franzke *et al.*, *Heavy ion beam accumulation, cooling and experiments at the ESR* in Proc. 1993 Part. Acc. Conf. (PAC), Washington D.C., (IEEE, Piscataway, NY, 1993) p. 1465.

[53] B. Schlitt, *Schottky Mass Spectrometry at the Heavy Ion Storage Ring ESR*, Dissertation GSI-97-01, September 1997.

[54] N. Angert *et al.*, *Electron Cooling on the ESR at GSI* in Proc. Europ. Part. Acc. Conf. (EPAC), Rome, ed. S. Tazzari (World Scientific, Singapore, 1988), p. 1436.

[55] F. Nolden, *Zur stochastischen Vorkühlung am ESR*, PhD Thesis, Technische Universität München, 1996.

[56] F. Bosch and B. Schlitt, Phys. Bl. **53**, 27 (1997).

[57] A. Gruber, W. Bourgeois, B. Franzke, A Kritzer and C. Treffert, Nucl. Instr. Methods. Phys. Res. A **282**, 87 (1989).

[58] Uwe Schaaf, *Schottky-Diagnose und BTF-Messungen an gekühlten Strahlen im Schwerionen-Speicherring ESR*, Dissertation Universität Frankfurt, GSI **91–22** (GSI Darmstadt, 1991).

[59] M. Steck, K. Beckert, H. Eickhoff, B. Franzke, F. Nolden, and P. Spädtke, Proceedings of 1993 Particle Accelerator Conference, Washington D.C. (1993) 1738.

[60] M. Steck, K. Beckert, H. Eickhoff, B. Franzke, F. Nolden, H. Reich, B. Schlitt and T. Winkler, Phys. Rev. Lett. **77** (1996) 3803.

[61] H. Reich, W. Bourgeois, B. Franzke, A. Kritzer and V. Varentsov, Nucl. Phys. **A 626** (1997) 417c.

[62] A. Krämer, Th. Stöhlker, A. Kritzer and H.Reich submitted to Elsevier Preprint (2000).

[63] J. Eichler, A. Ichihara, and T. Shirai, Phys. Rev. A **51**, 3027 (1995).

[64] A. Burgess, Mem. Roy. Ast. Soc. **69**, (1964)

[65] L.C.Biedenharn, J.L.McHale and R.M.Thaler, Phys. Rev., **100**, 376, 1955

[66] K. Alder and A. K. Winther, Danske Vidensk. Selsk.mat fys. Medd., **29**, No.18,1955

[67] H. A. Kramers, Philos. Mag. **46**, 836 (1923).

[68] J. R. Oppenheimer, Phys. Rev. **31**, 349 (1928).

[69] W. Wessel, Ann. Phys. (Leipzig) 5, 611 (1930).

[70] E. G. Stueckelberg and P. M. Morse, Phys. Rev. **36**, 16 (1930).

[71] D. Liesen and H. F. Beyer, Gesellschaft für Schwerionenforschung Report (Darmstadt) No. GSI ESR/86 04, 1986 (unpublished).

[72] R. Schuch, A. Baaaraaany, H. Danared, N. Elander, and S. Mannervik, Nucl. Instrum. Methods B **43**, 411 (1989).

[73] Y. Hahn and D. W. Rule, J. Phys. B **10**, 2689 (1977).

[74] Y. S. Kim and R. H. Pratt, Phys. Rev. A **27**, 2913 (1983).

[75] D. J. McLaughlin and Y. Hahn, Phys. Rev. A **43**, 1313 (1991).

[76] M. Pajek and R. Schuch, Phys. Rev. A **45**, 7894 (1992)

[77] M. Bell and J.S. Bell, Part. Accelerators 12, **49** (1982).

[78] A. Wolf, D. Habs, A. Lampert, U. Schramm, T. Schüβler, and D. Schwalm, in *Atomic Physics 13*, edited by H. Walther, T. H. Hänsch, and B. Neitzert, AIP Conf. Proc. No. 274, 228 (American Institute of Physics, New York, 1993). Nucl. Instrum. Meth. Phys. Res. **A 441**, 183, (2000).

[79] A. Wolf, G. Gwinner, J. Linkemann, A. A. Saghiri, M. Schmitt, D. Schwalm, M. Grieser, M. Beutelspacher, T. Bartsch, C. Brandau, A. Hoffknecht, A. Müller, S. Schippers, O. Uwira, D. W. Savin, Nucl. Instrum. Meth. Phys. Res. **A 441**, 183, (2000).

[80] A. Ichihara, and J. Eichler, Atomic Data and Nuclear Data Tables **74**, 1 (2000)

[81] Th. Stöhlker, T. Ludziejewski, F. Bosch, R. W. Dunford, C. Kozhuharov, P.H. Mokler, H. F. Beyer, O. Brinzanescu, B. Franzke, J. Eichler, A. Griegal, S. Hagmann, A. Ichihara, A. Krämer, J. Lekki, D. Liesen, F. Nolden, H. Reich, P. Rymuza, Z. Stachura, M. Steck, P. Swiat, A. Warczak, Phys. Rev. Lett. **82**, 3232 (1999).

[82] Th. Stöhlker, T. Ludziejewski, H. Reich, F. Bosch, R. W. Dunford, J. Eichler, B. Franzke, C. Kozhuharov, G. Menzel, P.H. Mokler, F. Nolden, P. Rymuza, Z. Stachura, M. Steck, P. Swiat, A. Warczak, Phys. Rev. A. **58**, 2043 (1998).

[83] Th. Stöhlker *et al*, Phys. Rev. Lett. **73**, 3520 (1994).

[84] H. K. Tseng, R. H. Pratt, S. Yu, A. Ron, Phys. Rev. A. **17** (1978) 1061.

[85] Schur, U. Fano, K. W. McVoy, and J. R. Albers, Phys. Rev. **116**, 1147 (1959).

[86] J. Eichler, Phys. Rep. **193**, 165 (1990).

[87] J. Eichler and W. Meyerhof, *Relativistic Atomic Collisions* (Academic Press, San Diego, 1995).

[88] A. Ichihara, T. Shirai, and J. Eichler, Phys. Rev. A **54**, 4954 (1996).

[89] R. Anholt *et al* Phys. Rev. Lett. **53** (1984) 234.

[90] J. R. Oppenheimer, Phys. Rev. **31**, 349 (1928).

[91] H. C. Brinkman and H. A. Kramers, Proc. K. Ned. Akad. Wet. **33**, 973 (1930).

[92] F. Decker and J. Eichler, Phys. Rev. A **44**, 377 (1991).

[93] J. Eichler, Phys. Rev. A **32**, 112 (1985).

[94] Th. Stöhlker, Phys. Scr. T 80 (1999) 165.

[95] Dz. Belkic, J. Phys. B 16 (1983) 2773.

[96] Dz. Belkic, R.Gayet and A.Salin, Phys. Rep. **56** (1979) 299

[97] E. Clementi and C.Roetti, At. Data **14** (1974) 177

[98] Dz. Belkic, R.Gayet and A.Salin, Comput. Phys. Commun. **32** (1984) 385.

[99] F.A. Parpia and I.P.Grant, J.Phys IV: Colloque C1, supplémment au J.Phys. II **1** (1991) c1-33.

[100] Minuit, CERN Program Library, entry D506, CERN-Geneva 1994.

[101] H. F. Beyer and Th. Stöhlker, in print (1999).

[102] P. Beiersdorfer, K. Widmann, J. Crespo Lopez-Urrutia, Hyperfine Interactions **114** (1998) 141.

[103] P. H. Mokler, Th. Stöhlker, C. Kozhuharov, R. Moshammer, P. Rymuza, F. Bosch, T. Kandler, Phys. Scr. T **51** (1994) 28.

[104] C. T. Munger and H. Gould, Phys. Rev. Lett. **57** (1986) 2927.

[105] G. W. F. Drake, Can. J. Phys. **66** (1988) 586.

[106] M. H. Chen, K. T. Cheng, and W. R. Johnson, Phys. Rev. A **47** (1993) 3692.

[107] D. R. Plante, W. R. Johnson, and J. Sapirstein, Phys. Rev. A **49** (1994) 3519.

[108] R. E. Marrs, S. R. Elliott, and Th. Stöhlker, Phys. Rev. A **52** (1995) 3577.

[109] Th. Stöhlker and E. A. Livingston, Acta Phys. Pol. **27** (1996) 441.

[110] P. Beiersdorfer, S. R. Elliott, A. Österheld, Th. Stöhlker, J. Autrey, G. Brown, A. J. Smith, and K. Widmann, Phys. Rev. A **53** (1996) 4000.

[111] S. Fritzsche, Th. Stöhlker, O. Brinzanescu, B. Fricke GSI-Preprint-99-45 (1999). Submitted to Hyperfine Interactions.

[112] F. A. Parpia, C. Froese Fischer and I. P. Grant, Comp. Phys. Commun. **94** (1996) 249.

[113] S. Fritzsche, C. Froese Fischer, and C. Z. Dong, Comp. Phys. Commun. in print (1999).

[114] G. W. F. Drake, Phys. Rev. A **34** (1986) 2871.

[115] F. A. Parpia, C. Froese Fischer, I. P. Grant, Comput.Phys. Commun. **94** (1996) 249.

[116] P. H. Mokler and Th. Stöhlker, Adv. in Atomic, Molecular, and Optical Physics, Vol.**37**, 297 (1996).

[117] H. F. Beyer, D. Liesen and O. Guzmann, Particle Accel., Vol. **24** (1989), 163-175.

[118] J. van den Bos and F. J. de Heer, Physica **34** (1967) 333.

[119] J. M. Feagin, J. S. Briggs, and T. M. Reeves, J. Phys. B **17** (1984) 1057.

[120] W. Fritsch and C. D. Lin, Phys. Rev. Lett. **61** (1988) 690.

[121] Th. Stöhlker et al., Phys. Rev. Lett. **84** (2000) 1360.

[122] Th. Stöhlker *et al*, Phys. Rev. Lett. **79**, 3270 (1997).

[123] H. Geissel, P. Ambruster, K.-H. Behr, B. Blank, A. Brünle, H. G. Burkhardt, K. H. Burkhardt, G.-G.Clerc, M. Chen, J. P. Dufour, B. Franczak, Y. Fujita, J. J. Gaimard, E. Hanelt, R. Kirschner, O. Klepper, B. Langenbeck, F. Nickel, K. Poppensieker, M. D. Pravikoff, E. Roeckel, D. Schardt, K.-H. Schmidt, Th. Schwab, H. J. Schött, B. Sherrill, K. Sümmerer, H. Wollnik, G. Münzenberg, Nucl. Instrum. Meth. Phys. Res. **B 70**, 286 (1992).

[124] J. Eichler, Nucl. Phys. A **572**, 147 (1994).

[125] S. J. Blakeway et al., J. Phys. B **16**, 3752 (1983).

[126] J. Eichler, A. Ichihara and T. Shirai, Phys. Rev. A **58**, 2128 (1998).

Acknowledgements

In first place, I would like to thank the person that gave me the unique opportunity to do this PhD work: Prof. Dr. Heinz-Jürgen Kluge, who kindly accepted me in his group and gave me support, encouragement and help every time I needed throughout the years of my PhD work.

For the direct supervising of my work I would like to express my very special thanks to Priv.-Doz. Thomas Stöhlker who has largely contributed to my deeper understanding of physics and has been following closely my work. His help as well as his suggestions were crucial to the development of my whole work.

I would like to thank to Prof. Dr. Jörg Eichler and Dr. habil. Stefan Fritzsche for their support to this work through theoretical calculations.

For the friendly environment and for their help I would like to thank to Priv.-Doz. Dorin Cezar Ionescu, Dr. Andreas Krämer and Dr. Xinwen Ma.

Here I would like to thank also to my diploma supervisor, Prof. Dr. Gheorghe Ciobanu from the University of Bucharest for his availability and friendly encouragement. For guiding my first steps towards the world of physics I would like to thank to Dr. Stefan Frunza from NILPRP, Bucharest.

I would like to express my gratitude to : Deutscher Akademischer Austauschdienst, V. Schad'schen Stiftung, Frankfurt am Main, and specially to Herr Cristoph Freiherr von Gemmingen-Guttenberg, and to Zonta Club, Mannheim who sustained financially my studies in Germany and allowed me to undertake this project.

A very special place in my thanksgiving I want to reserve to Prof. Dr. Violeta Dinescu whose kindness and support were essential.

For the good friendship and for the happy moments we spent together I would like to express my thanks to Faouzi, Magda, Caterina & Karsten, Laura and Giovanni.

The most special thanks I would like to give to my family and especially to my parents. They supported me and my choices financially, psychologically and mathematically and they were always very close, in spite of the physical distances.

To all who helped me to complete this PhD work my sincere thanks.